UC Irvine
UC Irvine Electronic Theses and Dissertations

Title

Characterization of Solid and Liquid Surfaces by X – ray Photoelectron Spectroscopy

Permalink

https://escholarship.org/uc/item/9zz2p787

Author

Bruce, Jared Patterson

Publication Date

2019

Peer reviewed|Thesis/dissertation

UNIVERSITY OF CALIFORNIA,
IRVINE

Characterization of Solid and Liquid Surfaces by X – ray Photoelectron Spectroscopy

DISSERTATION

submitted in partial satisfaction of the requirements
for the degree of

DOCTOR OF PHILOSOPHY

in Chemistry

by

Jared Patterson Bruce

Dissertation Committee:
Professor John Hemminger, Chair
Professor Wilson Ho
Professor Reg Penner

2019

DEDICATION

To

Steven G. Hodgkinson (d. 2018) and Eleanor M. Bruce (d. 2017)

Who both showed me, in their own way, that hard work could open any door

I hope I made you proud

TABLE OF CONTENTS

Page

LIST OF FIGURES

LIST OF TABLES

ACKNOWLEDGMENTS

I would like to thank Professor John Hemminger for his guidance and patience throughout my doctoral studies. John always gave me the freedom to pursue any project, idea or collaboration with full support and really allowed me to continue the exploration of science that I was looking for when I joined his group. Professors Reg Penner and Wilson Ho were on both my doctoral and candidacy committees and I have appreciated their support throughout this process. I would also like to thank Professors Matt Law, Kumar Wickramasinghe and Kieron Burke for their insight and guidance during my candidacy exam.

I have been lucky to work with so many great people during my PhD. When I started in the lab, Dr. Randima Galhenage showed me the ropes and day to day workings of the Hemminger Lab. I will be forever grateful for her help and friendship during my time at UCI. Dr. Djawhar Ferrah was a wonderful colleague and I can't thank her enough for the many conversations about science and life. Drs. Mike Makowski and Paulo Reyes were just completing their dissertations when I joined but our brief time together was a lot of fun. Drs. Anthony Babore and Joel Langford were staples of the lab for most of my time here. I will always appreciate Joel's help during beamline sessions or his input on my projects. I really can't thank Anthony enough for his friendship and sense of humour during my time. He always made coming to lab so much fun and kept it light during tough times. I would also like to thank Amanda Haines for the many conversations throughout my PhD and Jessica Kwo and Mohammed Alam for their hard work. Drs. Ira Waluyo and Adrian Hunt were so helpful at NSLS II when we worked there, and Drs. Hendrik Bluhm and Ethan Crumlin at the Advanced Light Source were great as well.

There are many people I would love to acknowledge here from the Class of 2015 but a few that really stand out to me. Devon Schatz and Dan Huh were the best friends anyone could ask for. We laughed and went on so many adventures together and I will be forever grateful for all your help and support during tough times. Caitlin Hanna, Meghan Newcomb and Krista Fruehauf are all wonderful people and researchers. They helped me see things from different points of view and will all be absolute rock stars wherever they decide to go. Austin Ryan and Chris Woods were also great buddies and I'll forever cherish their friendship. All the people from our softball team "Bad Life Choices" and ball hockey team "Honey Badgers" are the best and helped me get away from the lab.

Finally, I would like to thank my family. My Mom, Dad, Reid and Larah are the best people in the whole world. They support me wherever I am even though they are thousands of miles away. Without their love and support I would never have been able to achieve what I have, and they allow me to have the confidence to continue chasing my dreams. Wherever I go, whatever I do, I know they have my back and I can't thank them enough for that.

CURRICULUM VITAE

Jared Patterson Bruce

2012   B.Sc. (Hons) University of Manitoba, Winnipeg, Manitoba, Canada

2013   Special Student Researcher California Institute of Technology Pasadena, California, USA

2015   M.Sc. University of Manitoba, Winnipeg, Manitoba, Canada

2019   Ph.D. University of California, Irvine, Irvine, California, USA

FIELD OF STUDY

Chemistry; Surface Science

PUBLICATIONS

1. **Bruce, J. P.**, Hemminger, J. C.; Transition Metal Complexes in Aqueous Solutions Characterized by Liquid Jet Ambient Pressure X – ray Photoelectron Spectroscopy. *In Preparation*

2. **Bruce, J. P.**, Huh, D. N., Evans, W., Hemminger J.C., Exploring the Electronic Structure of Molecular Lanthanide Complexes in the +2 Oxidation State Using Photoelectron Spectroscopy. *In Preparation*

3. Ferrah, D., Haines, A.R., Galhenage, R.P., **Bruce, J. P.**, Babore, A.D., Waluyo I., Hunt A., Hemminger J.C.; Wet Chemical Growth and Thermocatalytic Activity of Cu based Nanoparticles Supported on TiO_2 Nanoparticles: In situ Ambient Pressure XPS Study of CO_2 Hydrogenation Reaction. *Submitted*

4. Galhenage, R. P., **Bruce, J. P.**, Bahr, S., Thissen, A., Hemminger, J. C.; A Lab Based Liquid Jet AP-XPS Apparatus to Investigate the Liquid/Solid/Vapor Interfaces. *In Preparation*

5. Galhenage, R.P., **Bruce, J.P.**, Ferrah, D., Waluyo, I., Hunt, A., Hemminger, J.C.; In-operando Study of CO Oxidation on Pt/TiO_2 Nanoparticles to Investigate the Reaction Mechanism: A Step Towards Closing the Pressure and Materials Gap. *In Preparation*

6. **Bruce, J. P.**, Babore, A.D., Galhenage, R. P., Hemminger, J.C.; Photodeposition and Control of Pt Oxidation States on TiO_2 Nanoparticles Supported on HOPG *In Preparation*

7. McEleney, K., **Bruce, J. P.**, Freund, M.S.; Characterization of High – Aspect Ratio Periodic Structures by X – ray Photoelectron Spectroscopy. Surface and Interface Analysis *Surface and Interface Analysis*, **2017**, 49, 503 – 514 DOI: 10.1002/sia.6186

8. Gupta, A., **Bruce, J.P.,** McEleney, K., Freund, M.S., Oliver D.R.; Important Monohydride Predictor for Successful Si(110) Surface Functionalization. *RSC Advances*, **2016**, 6, 88239 DOI: 10.1039/c6ra18009d

9. **Bruce, J. P.***; Giesbrecht P. K.*; Freund M. S.; Electrical Behavior of Thiophene and 3, 4 – Ethylenedioxythiophene Functionalized Planar n – Si/PEDOT:PSS Junctions for Artificial Photosynthetic Applications *ChemSusChem*, **2016**, 9 (1), 109 – 117 DOI: 10.1002/cssc.201501231

10. Kang O. S.; **Bruce J. P.**; Herbert D. E.; Freund M. S.; Covalent Attachment of Ferrocene to Silicon Microwire Arrays: A Model System for Integration and Characterization of Surface Bound Molecular Catalysts in Artificial Photosynthetic Devices *ACS Appl. Mater. and Interfaces*, **2015**, 7 (48), 26959 – 26967 DOI: 10.1021/acsami.5b07814

11. **Bruce, J. P**.; Oliver D. R.; Lewis N. S.; Freund M. S.; Electrical Characterization of the Junction Between PEDOT:PSS and Thiophene – Functionalized Silicon Microwires *ACS Appl. Mater. and Interfaces*, **2015**, 7 (49), 27160 - 27166 DOI: 10.1021/acsami.5b07725

12. McDonald, M.; **Bruce, J. P.**; McEleney, K.; Freund, M. S.; Reduced Graphene Oxide Membranes for Integrated Solar Water Splitting in Optimal OER and HER pH *ChemSusChem*, **2015**, *8* (16), 2645 – 2652; (Back Cover Article) DOI: 10.1002/cssc.201500538

13. McClarty, M. M.; **Bruce, J. P.**; Freund, M. S.; Oliver, D. R.; Piezoresistive Characterization of Bottom-up, n-type Silicon Microwires Undergoing Bend Deformation *Appl. Phys. Lett.* **2015**, *106* (2), 022107

14. **Bruce, J. P.**; Asgari, S., Ardo, S., Lewis N. S., Oliver, D. R., Freund, M. S.; Measurement of the Electrical Resistance of n-type Si Microwire/p-type Conducting Polymer Junctions for Use in Artificial Photosynthesis *J. Phys. Chem. C.* **2014**, *118* (48), 27742-27748; DOI: 10.1021/jp509211k

ABSTRACT OF THE DISSERTATION

Characterization of Solid, Gas and Liquid Interfaces by X – ray Photoelectron Spectroscopy

By

Jared P. Bruce

Doctor of Philosophy in Chemistry

University of California, Irvine, 2019

Professor John C. Hemminger, Chair

X – ray photoelectron spectroscopy (XPS) has traditionally been used to characterize the chemistry at solid surfaces. Recently, work has been done to expand the utility of XPS to other interfaces such as liquids. Work carried out in this thesis focused on a wide range of experimentation using photoelectron spectroscopy. XPS under ultra-high vacuum conditions is used to characterize the photodeposition of Pt nanoparticles on the surface TiO_2 nanoparticles supported on highly oriented pyrolytic graphite (HOPG). Following the Pt 4f peak, photodeposition and photoreduction of the Pt nanoparticles on the surface of TiO_2 can be observed. A shift from a oxidized Pt(IV) state (75.2 eV) to a Pt(II) state (72.5 eV) is observed over longer illumination times. Pt(0) is only observed after heating is applied. Temperature programmed desorption showed a decrease of the desorption temperature of water with Pt in its reduced form on the surface of TiO_2.

Liquid interfaces using a liquid jet were also characterized in later Chapters of this thesis. Fe(II) salts were dissolved in acidic aqueous solution and the interaction between iron and halides were characterized. A small shift in the Cl 2p binding energy (0.4 eV) was observed for Cl^- but not observed for Br^-. The association of Cl^- to Fe(II) also leads to changes in the relative contributions

of Fe and Cl species near the interface. In a subsequent chapter, changes to the intramolecular interactions of acetic acid lead to relative binding energy shifts in the C 1s region of the spectrum. These shifts are related to the hydrogen bonding present in the solvation sphere of the acetic acid in aqueous and methanol solutions. Finally, a mixing jet was generated and characterized using sodium iodide. The signal intensity is related to the relative flow rate input in the microfluidic chips which form the foundation for kinetic reaction experiments of complex solutions using XPS.

Chapter 1: Introduction

Surfaces and Interfaces

Heterogeneous chemistry is driven at the surface of solids and liquids. The surface of a material is the outermost atomic layers (~ 10Å) that differ electronically and structurally from the bulk interior.[1] The interface between different phases of matter is often overlooked and bulk processes are considered to dominate throughout the depth of the material. Experiments that focus purely on interactions with the surface of a material are unique and offer a critical perspective towards understanding the chemistry that occurs there. These techniques often rely on ultra – high vacuum because of the short mean free path of ions and electrons that are used in the analysis.[1] One of the critical techniques in this work and in work focused on surfaces and interfaces has been X – ray photoelectron spectroscopy (XPS).

X – ray Photoelectron Spectroscopy

The photoelectric effect is the fundamental principle to which photoelectron spectroscopy is built upon. The photoelectric effect relationship is shown below:

$$E_k \ = \ h\nu - E_b - \varphi \qquad\qquad (1.1)$$

The kinetic energy of an electron (E_k) increases with increasing photon energy ($h\nu$). The binding energy (E_b) and workfunction (φ) represent the minimum amount of energy required to remove an electron from the medium at a certain orbital energy. When using X – rays, enough energy is applied to remove electrons from core orbitals within a molecule. For example, an atom of carbon has $1s^2 2s^2 2p^2$ orbital configuration and when irradiated by X – rays of enough energy, the carbon will emit electrons from all orbitals. The C 1s core orbital is often used to characterize all forms of carbon within a sample. Ultraviolet radiation has also been used in photoelectron spectroscopy;

however, this wavelength range only allows investigation of orbitals in the valence region or bonding orbitals within the molecules. A depiction of photoelectron spectroscopy is shown in Figure 1.1 below.
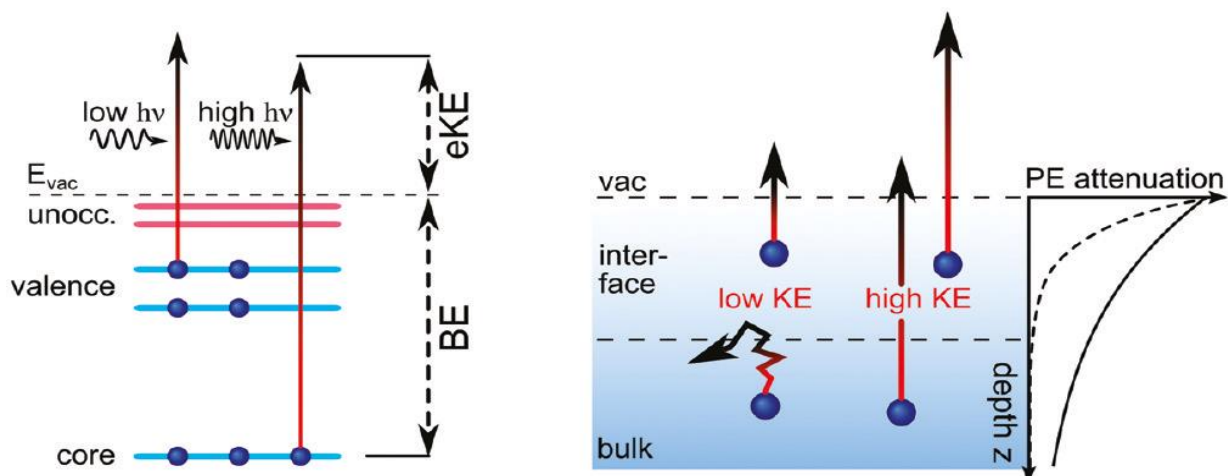
Figure 1.1: *Representation of the photoelectric effect using both high and low energy radiation to illuminate a sample. Reproduced with permission from Reference 2.*

Photoelectron spectroscopy has become a central technique in surface science due to its sensitivity to different chemical states of a molecule within a sample. The limited mean free path of the generated photoelectron within a material generally means photoelectron spectroscopy is a surface sensitive analysis technique. The attenuation of the photoelectron, as depicted to the right in Figure 1, can be modified by using different wavelengths of light thereby creating a depth dependent measurement of the different chemical states within a given probe depth.[2]

Solid materials and solid/gas interactions have traditionally been the main analysis target for XPS experiments; however with the development of electron transfer lenses and differential pumping, XPS can now be carried out in near ambient conditions and has enabled the ability to characterize liquid samples in so called ambient pressure (AP) XPS. Various methods have been used to generate a clean, uniform liquid surface. The method of choice used in our lab is the

generation of a liquid jet.[3–7] The ability to obtain chemical information by characterizing the changes of electronic structure of a molecule within a liquid near the surface opens up many new opportunities to understand liquid surfaces. Furthermore, the addition of gases to the background of the liquid jet chamber will allow for the gas – liquid interface to be investigated for different chemical reactions and transformations at the surface.

Overview of this Thesis

The use of X – ray photoelectron spectroscopy is the focal point of this thesis to show the breadth and impact it can have on the characterization of different surfaces. In Chapter 3, there will be a focus on solid nanoparticle samples and their application as a fundamental model system of a heterogeneous catalyst for different solid/gas reactions. The nanoparticle growth using photodeposition from aqueous solutions were investigated using XPS to determine the different oxidation states present at the interface after the deposition. The surface interaction with water was investigated using temperature programmed desorption and shows that an increase of Pt(0) concentration on the surface causes a decrease in the desorption temperature. In the following chapters, the work focuses on using AP – XPS to characterize liquid surfaces with different solutes contained in an aqueous solution. Chapter 4 investigates the changes in the inner sphere coordination of Fe(II) when chloride and bromide are in the solution. Chapter 5 characterizes the changes in solvation of acetic acid whether it's dissolved in methanol or aqueous solution. In Chapter 6, the framework is developed for characterizing a mixing jet that could be used to investigate nanoparticle formation at the earliest stages. Finally, conclusions drawn from the work throughout this thesis are shown and a pathway to more experiments using XPS are proposed in the last chapter.

References

1   O. K., V. G. Lifshits, A. A. Saranin, A. V. Zotov and M. Katayama, *Surface Science: An Introduction*, 2003.

2   R. Seidel, S. Thürmer and B. Winter, Photoelectron spectroscopy meets aqueous solution: Studies from a vacuum liquid microjet, *J. Phys. Chem. Lett.*, 2011, **2**, 633–641.

3   M. Trebbin, K. Kruger, D. DePonte, S. V Roth, H. N. Chapman and S. Forster, Microfluidic liquid jet system with compatibility for atmospheric and high-vacuum conditions, *Lab Chip*, 2014, **14**, 1733–1745.

4   K. A. Perrine, M. H. C. Van Spyk, A. M. Margarella, B. Winter, M. Faubel, H. Bluhm and J. C. Hemminger, Characterization of the acetonitrile aqueous solution/vapor interface by liquid-jet X-ray photoelectron spectroscopy, *J. Phys. Chem. C*, 2014, **118**, 29378–29388.

5   S. Ghosal, J. C. Hemminger, H. Bluhm, B. S. Mun, E. L. D. Hebenstreit, G. Ketteler, D. F. Ogletree, F. G. Requejo and M. Salmeron, Electron Spectroscopy of Aqueous Solution Interfaces Reveals Surface Enhancement of Halides, *Science*, 2005, **307**, 563–566.

6   J. Knudsen, J. N. Andersen and J. Schnadt, A versatile instrument for ambient pressure x-ray photoelectron spectroscopy: The Lund cell approach, *Surf. Sci.*, 2016, **646**, 160–169.

7   J. A. Faust and G. M. Nathanson, Microjets and coated wheels: versatile tools for exploring collisions and reactions at gas-liquid interfaces, *Chem. Soc. Rev.*, 2016, **45**, 3609–3620.

Chapter 2: Experimental Methods and Techniques

Introduction

Throughout this thesis, the common instrumentation used in X – ray photoelectron spectroscopy (XPS) relies on ultra – high vacuum (UHV) conditions. In this chapter, an overarching theme for the utilization of XPS for both solid and liquid surfaces will be discussed including instrumentation and run parameters for different experiments. Specific experiments will be run under different parameters and these details will be provided at the beginning of each chapter.

Solid State XPS

In the first chapter of this thesis, there will be a focus on solid state experimentation. The solid-state photoelectron spectrometer that was used is an ESCALAB MK II from VG Scientific. Both the Al kα and Mg kα spectral lines were used in the twin anode setup in the XPS. The excitation energy from the Al kα line was 1486.6 eV while the excitation energy for the Mg kα was 1253.6 eV. All spectra were collected at a voltage of 20 kV and an emission current of 10 mA. All survey spectra were collected at 100 eV pass energy while high resolution spectra were collected at 20 eV pass energy. The analysis was carried out at < 1 x 10^{-10} Torr. The analyzer in the ESCALAB is a hemispherical analyzer with channeltrons as the detectors. Channeltrons are electron multipliers that will generate an avalanche cascade when an electron interacts with the walls of the channeltron tube. This allows a single electron to generate as many as 10^8 electrons in the cascade, providing a much higher current for the analysis of the sample. There is a total of three channeltrons on the ESCALAB.

Grounding of the samples is extremely important in XPS. Charge buildup at the surface will shift or broaden the photoelectron peaks. For most samples investigated in this work charging was

not a problem as the samples were grown on graphite surfaces that are easily grounded within the chamber. If there were small shifts in the binding energies, the spectra of the sample would be calibrated to the graphitic carbon at 284.3 eV.

Liquid Jet XPS

Investigation of liquid surfaces with photoelectron spectroscopy has been challenging due to the ultra – high vacuum requirement of these experiments. However, the development of ambient pressure (AP) XPS has enabled us to leverage the surface sensitivity in the characterization of liquids. Liquid XPS has been carried out at different synchrotron and free electron laser facilities throughout the US, however high competition and limited beamline time has limited the number and scope of the experiments. At UCI, we were fortunate to have the first lab – based liquid jet XPS designed and built in our lab. We worked with SPECS Surface Nano Analysis GmbH out of Berlin, Germany. The analyzer is a SPECS Phoibos NAP 150 with a double delay line detector (1D-DLD64_2-150). The x – ray source is monochromatic Al kα radiation using the SPECS μ - FOCUS 350 monochromator. The pre – lens and lens systems are differentially pumped and have several refocusing voltages that can be tuned to optimize the signal going into the analyzer. The entrance cone has a diameter of 300 μm. The x – ray source and analyzer are maintained at 1×10^{-9} Torr when not in use. The instrument is also equipped with a UV source (SPECS UVS 300), but was not utilized in this works. Figure 2.1 below shows a cross sectional schematic of the new ambient pressure liquid jet XPS
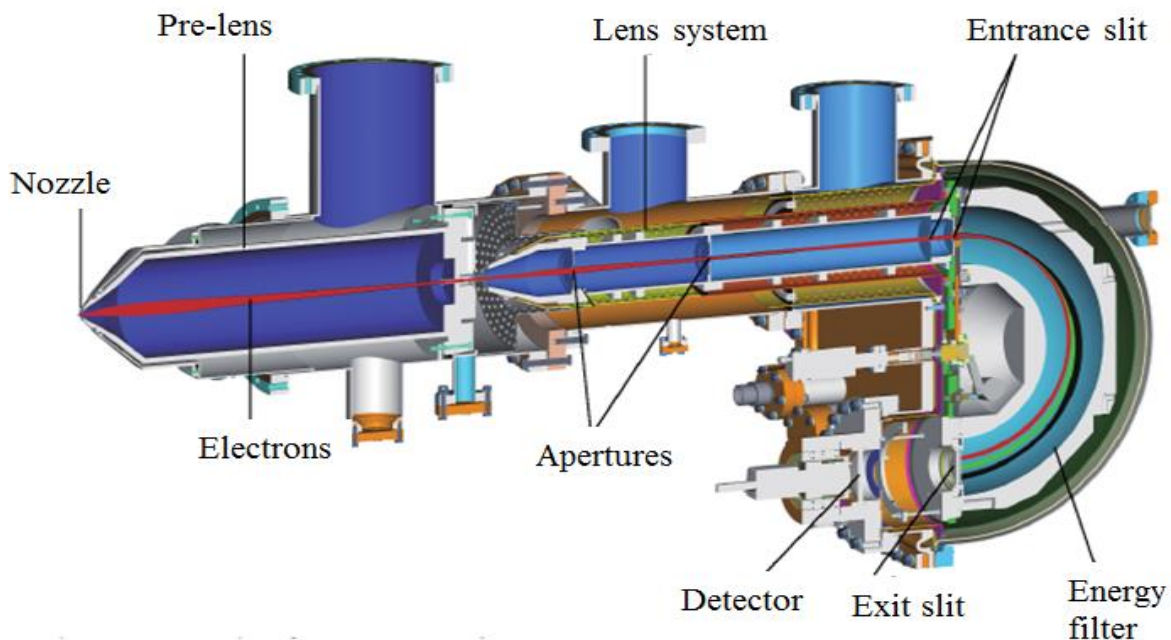
Figure 2.2: *Cross sectional schematic of the pre-lens, lens and analyzer of the lab – based ambient pressure liquid jet XPS at the University of California, Irvine.*

Generation of the liquid jet was achieved by using a HPLC pump tied into a solution loop that could be isolated from the capillary tube responsible for the generation of the jet. Capillary tubes were made of borosilicate glass and had an exit diameter of ~20 µm. The liquid jet setup is shown in Figure 2.2 below.
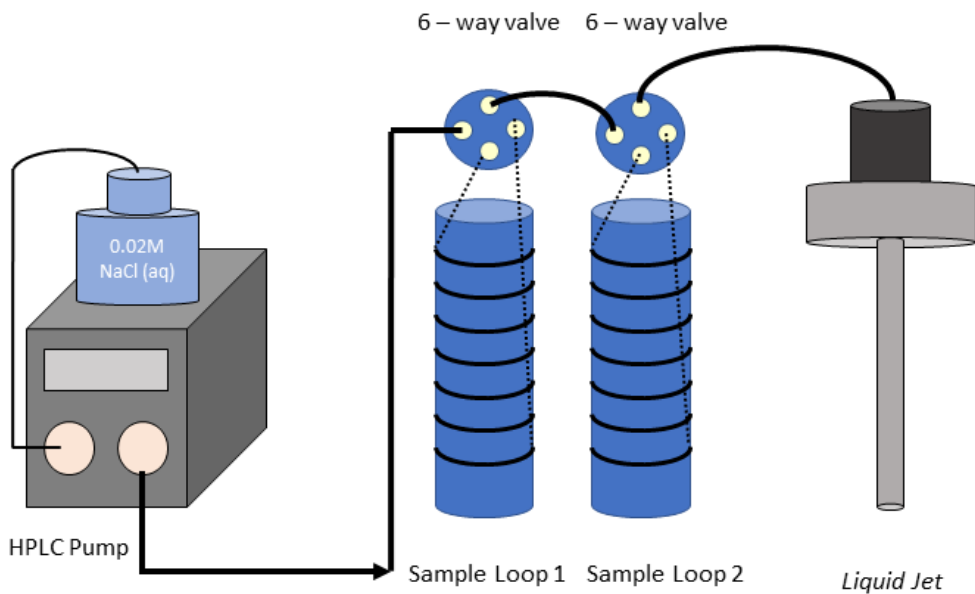
Figure 2.3: *Schematic representation of the liquid jet setup used in the ambient pressure XPS. Two sample loops are used to have continuous sample available for analysis. Once one loop is used, the next will be filled and ready for analysis.*

Any solution of interest is loaded into the sample loops using a syringe and a 25 mm, 0.45 µm syringe filter. The 0.45 µm nylon membrane in the syringe filter removes large, insoluble salt particles that may be in the solution. The solution is also passed through a 2 µm inline filter prior to pumping out to the liquid jet setup from the sample loops. *This filter often clogs with debris or any other insoluble solute and should be replaced regularly.* A dilute salt solution is used to push the sample solution out of the loop after it is injected into the liquid jet instrument. A concentration of 0.02M NaCl is used as it is high enough to dissipate the charge, while low enough to avoid detection during the experiment.

When the liquid jet is installed on the chamber, the waste of the jet is collected by a temperature-controlled basin with saturated NaCl solution at the bottom. Saturated NaCl solutions lower the vapor pressure of the water and allow the chamber pressure to be controlled by the vacuum. The basin is set at a temperature of -5 °C, which has been optimized to ensure the jet does

not freeze from the basin up to the capillary tube. At this temperature, the jet is stable. There is a high signal to noise in the O 1s spectra of the liquid phase water and there is little concern of freezing. The background pressure is also set to 4 mbar on the AP – XPS by the vacuum control. Lower pressures can be achieved, however there is a greater risk of the jet freezing without any significant increase in the signal to noise ratio of the liquid peak.

The instrument is then calibrated using the O 1s water gas phase peak. This peak often occurs at 535.5 eV and is used to charge correct the spectra of the entire experiment. In the literature, the liquid phase peak was used to correct for any charging that may occur and was set to 538 eV.[1–6] This value is based on the valence band spectrum of a water solution and is calibrated to the vacuum level. In the lab – based system, we are still gathering our data with respect to the Fermi level which includes the work function of the instrument. This work function is what makes up the difference between the binding energy observed in our experiment and those reported in the literature. Therefore, all data are reported with respect to the Fermi level rather than an absolute binding energy. The gas phase peak is also a more accurate metric for charge correction, as it is indifferent to minor charge fluctuations that could occur in the liquid. These fluctuations may cause small shifts in the binding energy of the O 1s liquid peak.[7] This is why the O 1s gas phase water peak was used for charge correction.

Once the instrument has been tuned to the gas phase peak, it will then be re-tuned to the liquid phase peak when the liquid jet is brought in front of the cone at the entrance to the energy analyzer. When switching between loops, the jet is moved away from the cone, the loops are switched, and the jet is re – optimized in its position in front of the cone. The background pressure of the chamber should be maintained at 4 mbar. The x – ray source pressure will be around 1×10^{-7} mbar and the analyzer will be at 1×10^{-8} mbar during the collection of the liquid jet photoelectron spectra. All

individual parameters utilized to collect the data will be outlined in the individual chapters. The x – ray parameters used for the experiment are set based on the spot size of the x – ray source. In our case, the x – ray spot was ~40 µm in diameter which is slightly larger than the diameter of the jet (20 µm). UV experiments can also be carried out on the liquid jet instrument; however, the spot size is much larger (>100 µm) and has a very large gas phase component. UV experiments were not a focus of this work.
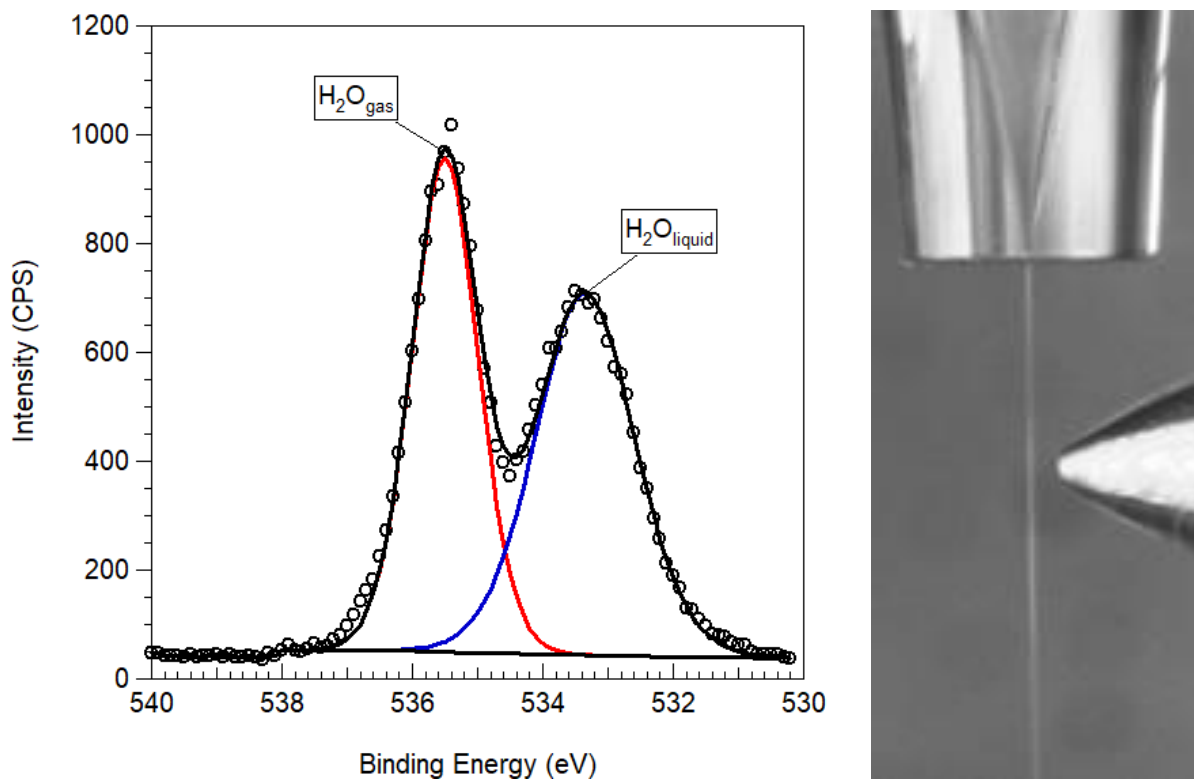
Figure 2.4: O 1s spectrum of the liquid jet with 0.02M NaCl in an aqueous solution. The binding energy of the gas phase peak is 535.5 eV while the liquid phase peak is located at 533.5 eV. A light image of the liquid jet is shown to the right of the O 1s spectra. The cone is 300µm in diameter and the liquid jet is 20 µm in diameter.

In Figure 2.4, a typical O 1s spectrum of the liquid jet when 0.02M NaCl aqueous solution is shown. The two peaks that occur in the spectrum are from the gas phase water peak (535.5 eV) and the liquid phase water (533.5 eV). A light image of the liquid jet during operation is also shown in Figure 2.4. When loops are switched, the liquid jet is moved away from the entrance to

the analyzer cone to prevent any liquid from splashing into the chamber behind it. Tuning of the instrument is done by moving the liquid jet close to the cone while scanning on the liquid phase peak at 533.5 eV. These two peaks play a critical role in the data interpretation of all the liquid jet characterization. The gas phase peak is set to 535.5 eV, as indicated above, to correct for any charge accumulation that may occur on the surface of the jet. All ratios of the data will be based on the liquid phase peak. Equation 2.1 below is the relationship for the photoelectron intensities of different orbitals.[8]

$$I_i = J_0\sigma_i(hv)T \int_{\gamma=0}^{\pi} \int_{\phi=0}^{2\pi} L_i(\gamma) \int_{z=0}^{\infty} n_i(z)\exp(\frac{-z}{\lambda_i cos\theta})dzd\gamma d\phi \qquad (2.1)$$

Where

J_0 = is the intensity of the primary x – ray beam;

γ = is the angle between the incident x – ray beam and the direction of the ejected photoelectron;

$L_i(\gamma)$ = is the angular dependence of photoemission

$\sigma_i(hv)$ = is the photoionization cross – section of the core level K by a photon with energy hv

T = transmission function of the instrument dependent on kinetic energy

$n_i(z)$ = number of species with respect to depth

λ_i = inelastic mean free path of the electron

Rather than trying to evaluate an individual peak intensity to calculate the total number of species with a specific orbital within a specific depth ($n_i(z)$), a ratio between two orbitals can be used. This ratio simplifies the J_0, T and γ dependence on the spectra. The angular dependence of analysis ($cos\theta$) is also considered to be 1 due to the analysis being conducted normal to the liquid jet surface. The inelastic mean free path (IMFP) is related to the kinetic energy of the photoelectron above 100 eV. The photon energy is the maximum depth z, of any photoelectron and integrating the last term

will evaluate the ratio while accounting for the depth dependence. We can then use the ratio and consider the x – ray photoionization cross section and asymmetry parameter of the orbitals to give a much more simplified version of Equation 1 and the IMFP.

$$\lambda_i = KE_i(eV) - KE_i \exp\left[\frac{KE_i(eV)}{h\nu\,(eV)}\right] \tag{2.2}$$

$$\frac{I_a}{I_b} = \frac{n_a(z)\sigma_a(h\nu)L_a(\gamma)\lambda_a}{n_b(z)\sigma_b(h\nu)L_b(\gamma)\lambda_b} \tag{2.3}$$

Though there are many limitations to this simplification, provided the photoelectron has a kinetic energy above 100 eV, a reasonable first approximation of the ratio is obtainable. A sample calculation is shown in Appendix I with the NaBr system of Chapter 4.

Data collected at the Advanced Light Source (ALS) provided intensity ratios that were simpler to elucidate. The depth dependence of the photoelectron is determined by characterizing each individual orbital at the same photoelectron kinetic energy. For example, O 1s is characterized at 835 eV excitation energy and Br 3d is characterized at 368 eV excitation energy to generate a photoelectron kinetic energy of 300 eV for both orbitals.

Peak Fitting

In the final section of this Chapter there will be a discussion of the peak fitting thought process that is used throughout this thesis. Fitting of transition metals, lanthanides and complex surfaces is challenging and must be carried out in a consistent, transparent and chemically relevant way. The interpretation of the sample should always be presented with the chemical information at the forefront of the discussion. Although the physical effects form the foundation of the analysis, it is the chemistry that leads to the greatest change in core orbital structure and interpretation. Over (where more peaks are added) or under (not enough peaks are added) fitting of a specific orbital window can lead to misleading results. Constraint of the peak fit should be avoided except when quantum mechanical effects are considered such as spin – orbit coupling ratios between peaks or

spin – orbit binding energy differences. Additional constraints should only be added if chemically or physically relevant.

In Chapter 3 the focus of the work will be on the identification and characterization of different oxidation states of Pt that are deposited on the surface of TiO_2 nanoparticles from aqueous solution. The Pt 4f spectrum is initially fit with two spin – split peaks (Pt $4f_{7/2}$ and Pt $4f_{5/2}$) that represent a single oxidation state of Pt(IV). As the photoreduction is occurring on the surface of the particles, other oxidation states are observed in the spectrum representing Pt(II) and eventually Pt(0) respectively. These peaks are added with the same spin – split pairs as the Pt(IV) case, but are shifted to lower binding energy as they become more reduced. The important constraints on those peaks are the relative ratio ($4f_{7/2}$:$4f_{5/2}$ is 0.75) and the relative splitting. The peaks are then allowed to find the best fit of the data without any additional constraints of the peaks. These fits allowed us to understand the effect of the photodeposition and photoreduction on the Pt species deposited on surface of the TiO_2.

In Chapter 4, the interpretation of the Cl 2p spectra at different chloride concentrations with and without the Fe(II) in solution was based on a careful peak fit of the data. The advantage of peak fitting liquid XPS data is that a more systematic experimental procedure can be used to monitor small changes in the photoelectron spectra. For example, a pure NaCl solution with increasing concentration was characterized first, with a single set of spin – split peaks. These peaks were then constrained when Fe(II) was present in the solution and the fit did not represent the data. A second set of peaks were added to the spectrum and allowed for proper description of the data. The splitting between the two sets of data is small (~0.4 eV), but is still significant based on the systematic use of the different solutions to deconvolute the peak fit.

Finally, in Chapter 5, peak fitting was used to characterize the solvation of acetic acid and its

derivatives in both aqueous and methanol solutions. This was done in both the gas phase and liquid phase with the relevant species. In most of these fits there was a straightforward approach to adding peaks based on the data. The details are described in the chapter at length. However, in the methanol solution the C 1s spectra became very convoluted and challenging to interpret. Again, liquid phase spectra have the benefit of a more systematic approach for interpreting a sample. In the acetic acid/methanol solutions, the methanol solution can be characterized separately, and any additional peaks can be added to the constrained methanol fit. The acetic acid peaks, both gas and liquid phase, were added to the constrained methanol peak model and allowed to fit the data. The methyl and carbonyl peaks have been shown in previous aqueous solutions to produce a relative area ratio of 1:1, which is consistent, chemically, with the molecule. This was an added constraint to the fit of the methanol/acetic acid solution and allowed a more complete interpretation of the C 1s data.

Careful interpretation of all XPS spectra, whether it is solid, liquid or gas phase, begins with a knowledge of the chemistry of the sample. Additional peaks and deeper interpretation are welcome provided they are consistent with the sample of interest.

References

1   J. W. Smith and R. J. Saykally, Soft X-ray Absorption Spectroscopy of Liquids and

Solutions, *Chem. Rev.*, 2017, **117**, 13909–13934.

2   M. Faubel, K. R. Siefermann, Y. Liu and B. Abel, Ultrafast soft X-ray photoelectron spectroscopy at liquid water microjets, *Acc. Chem. Res.*, 2012, **45**, 120–130.

3   B. Winter, R. Weber, W. Widdra, M. Dittmar, M. Faubel and I. V. Hertel, Full Valence Band Photoemission from Liquid Water Using EUV Synchrotron Radiation, *J. Phys. Chem. A*, 2004, **108**, 2625–2632.

4   R. Seidel, S. Thürmer and B. Winter, Photoelectron spectroscopy meets aqueous solution: Studies from a vacuum liquid microjet, *J. Phys. Chem. Lett.*, 2011, **2**, 633–641.

5   T. Fransson, Y. Harada, N. Kosugi, N. A. Besley, B. Winter, J. J. Rehr, L. G. M. Pettersson and A. Nilsson, X-ray and Electron Spectroscopy of Water, *Chem. Rev.*, 2016, **116**, 7551–7569.

6   B. Winter and M. Faubel, Photoemission from Liquid Aqueous Solutions, *Chem. Rev.*, 2006, **106**, 1176–1211.

7   N. Kurahashi, S. Karashima, Y. Tang, T. Horio, B. Abulimiti, Y. I. Suzuki, Y. Ogi, M. Oura and T. Suzuki, Photoelectron spectroscopy of aqueous solutions: Streaming potentials of NaX (X = Cl, Br, and I) solutions and electron binding energies of liquid water and X-, *J. Chem. Phys.*, 2014, **140**, 17506.

8   O. K., V. G. Lifshits, A. A. Saranin, A. V. Zotov and M. Katayama, *Surface Science: An Introduction*, 2003.

Chapter 3: Photodeposition and Control of Pt Oxidation States on TiO₂ Nanoparticles Supported on HOPG

Introduction

Heterogeneous catalysts are critical to many aspects of environmental, energy and biochemical processes. The understanding of chemical transformations on the surface of these materials has been enabled by rigorous control over the solid interface and the reaction gases under ultra – high vacuum (UHV) conditions. Traditionally, this requires the use of catalysts in their single – crystalline form that are cleaned via a combination of sputtering, heating and/or reactive gases in the vacuum to ensure unobstructed interaction of the adsorbate with the surface.[1–8]

Careful control over the interface of heterogeneous catalysts has deepened our fundamental understanding of reactions at these surfaces; however, there still exists a significant gap between single – crystal studies and industrially relevant systems. Within an industrial scale process, the catalytic material is often supported on colloids or small oxide particles to prevent the metal from sintering together to form larger particles.[9] Sintering reduces the available surface area for the reaction to take place, thereby reducing the catalytic efficiency of the metal.[10] Many studies focus solely on the active catalytic material at the nanoscale but haven't considered a support material at the nanoscale. Nanoparticles of Pt, Pd and Au have been evaporated in a vacuum chamber on a multitude of single – crystal oxide supports.[1,4,11–13] Aluminum oxide (Al_2O_3), titanium dioxide (TiO_2), cerium dioxide (CeO_2) and silicon dioxide (SiO_2) are the most common oxide support for the nanoparticles mentioned previously.[14] These oxides are stable at elevated temperature and provide enough binding energy to prevent the nanoparticles from sintering and maintaining a high surface to volume ratio required for adequate catalytic activity. However, the single – crystal and thin film forms of TiO_2 and CeO_2 have been shown to adversely affect the catalytic efficiency of

16

the nanoparticles by the growth of a thin oxide layer around the particle. This effect is known as strong – metal support interactions (SMSI) and has been frequently observed for most reducible oxide supports where Pt and Pd serve as classic, well studied examples.[2,11,15–17] In addition to sintering, the structure of the exposed surface of colloids is more complex compared to well – defined single crystal surfaces. This represents another gap between industrial catalysts and fundamental studies known as the complexity gap. The interaction of reactants with the surfaces of colloids could be different due to the multitude of crystal facets and edges present. A model system that addresses this complexity has only recently been developed.[18]

To address the gaps between fundamental and industrially relevant catalytic systems, nanoparticles of TiO_2 have been synthesized on highly – oriented pyrolytic graphite (HOPG) using physical vapor deposition through evaporation of titanium.[18] These nanoparticles orient themselves along the step edges of the HOPG. For a higher density of particles, the HOPG can be plasma cleaned to generate defect sites where the TiO_2 nanoparticles will form. Rigorous control of the deposition parameters, such as temperature of substrate and background pressure, will generate crystalline or amorphous TiO_2 and different size distributions of particles on the surface.[18] Additionally, catalytic metals can be deposited on the surface of TiO_2 by illuminating the material with above band gap radiation to generate charge carriers in the semiconductor. These charge carriers can then oxidize or reduce a metal salt in solution and deposit the material on the surface.

Pt is a widely used metal for the catalytic oxidation of carbon monoxide,[19] the water – gas shift reaction,[20] proton reduction and isomerization of hydrocarbons.[21] While it can be deposited as nanoparticles on oxide supports within a vacuum chamber, the most attractive method for deposition on the TiO_2 nanoparticles is photodeposition by irradiation with light above the band

gap.[22] This method has been shown to quickly deposit Pt on nanoparticles dispersed in solution and has been applied herein to the TiO_2 nanoparticles supported on HOPG.[18,23,24]

Deposition through this method generates an inconsistent molecular distribution of oxidation states throughout the literature.[8,17,23–28] Bulk Pt metal is often referenced to 70.8 eV in X – ray photoelectron spectroscopy; however, the size of the nanoparticle plays a significant role in the binding energy of the metallic peak.[30–32] The metallic peak of small nanoparticles can be up to 1 eV greater than that of larger particles (> 5 nm). Additionally, photodeposition generates Pt oxides on the surface of the TiO_2 with PtO_2 manifesting at 75.2 eV and PtO_x at $73 – 75$ eV.[25,33,34] This range in binding energies for reduced Pt oxides observed in the literature creates a significant challenge when identifying the major contributing species to the catalytic cycle on the nanoparticle and its support.

Control of these oxidation states is challenging in a suspension. The nanoparticles supported on HOPG in this study can be treated sequentially with varying experimental conditions after the Pt has been deposited and can provide a more systematic control over the oxidation states. This system is also an ideal candidate for *in situ* work as the nanoparticles are supported on a relatively inert substrate, HOPG. Furthermore, the supported nanoparticles represent an ideal system for investigating the adsorption and desorption of small probe molecules, which is a significant challenge for dispersed nanoparticle solutions. Depositing nanoparticles from solution by drop, spin or other coating method on HOPG may not be well distributed across the surface and is difficult to control for systematic desorption studies. There is also the added challenge of removing the surfactant used in nanoparticle synthesis to create a clean interface between the nanoparticle and the adsorbing molecules, creating a gap in the literature comparing the desorption kinetics between single – crystals and nanoparticles. The complexity and structure of nanoparticle surfaces

may influence the desorption of probe molecules. By utilizing physical vapor deposition, there are no ligands present and the distribution is determined by plasma generated defect sites on the HOPG and the deposition conditions. This allows for small probe molecules, such as water, to be used for investigating the adsorption/desorption kinetics on the nanoparticles. It also provides the unique opportunity to study each component of the experimental procedure prior to the subsequent step. Desorption from the substrate, the TiO_2 and Pt can all be investigated sequentially, allowing for observation of each step on the desorption kinetic profile.

In the work presented herein, we address some of the significant challenges to investigating nanoparticle/nanoparticle systems that have the potential to become models for industrial catalysts. First, we show that photodeposition occurs through deposition of Pt oxide and subsequent reduction by photogenerated carriers. Second, we show the dominant species in the catalytic cycle is the Pt (0) rather than an oxidized form. Finally, we show the change in the water desorption characteristics due to Pt deposition indicating that the Pt resides on bridging oxygen sites rather than open Ti sites on the TiO_2.

Experimental

Formation of TiO₂ Nanoparticles and Deposition of Pt

Highly – oriented pyrolytic graphite (HOPG/ZYB/DS/1, *MikroMasch,* spread $0.8° \pm 0.2°$) is cleaved using the "Scotch tape" method to give an atomically flat surface. HOPG samples are then oxygen plasma cleaned to generate anisotropic nucleation sites for TiO_2 nanoparticle growth.

TiO_2 nanoparticles are synthesized using a physical vapor deposition method developed by NAME.[18] HOPG samples approximately 1 cm^2 are heated to 800°C at an operating pressure of ~ 5 x 10^{-6} Torr in an Edwards E306A evaporator. Titanium shot (6N, Ted Pella) is resistively heated and exposed to the heated sample to deposit TiO_2 nanoparticles across the surface. The

nanoparticles are rutile (110) phase as observed by transmission electron microscopy (TEM) and X-ray absorption (XAS).[18]

Pt nanoparticles are deposited from a 1 µM aqueous solution of K_2PtCl_4 or K_2PtCl_6 (99.99% trace metal basis, Sigma Aldrich) dissolved in HPLC grade water (Sigma Aldrich). TiO_2-HOPG samples were mounted on an in – house constructed sample stage and exposed to UV light for up to 3 hours unless otherwise indicated. Approximately 5 mL of the aqueous Pt solution was bubbled with Ar (Research Grade, Airgas) for at least 30 minutes over the TiO_2-HOPG before irradiation. After deposition, Pt/TiO_2-HOPG samples are rinsed with copious amounts of HPLC grade water before transferring to spectrometer for analysis. The samples were kept under vacuum (< 1 Torr) until further characterization.

X – ray Photoelectron Spectroscopy (XPS)

Photoelectron spectroscopy was performed using an ESCALAB MKII (VG – Scientific) spectrometer. A twin Mg/Al X-ray source is used with an electron emission of 20 mA and accelerating voltage of 10 kV. Survey spectra were acquired using a pass energy of 100 eV, while high resolution scans were acquired using a pass energy of 20 eV. Mg Kα (1253.6 eV) X-rays were used during experiments.

All high-resolution spectra utilized a Shirley algorithm to define the background and mixed Gaussian – Lorentzian peaks to define the different chemical states. Most samples did not require charge neutralization or charge correction due to the sufficient conductivity of the sample, however, when required, the sample was charge corrected to the graphitic C 1s peak at 284.5 eV. The Pt 4f region was fit using two, spin – split Gaussian peaks with a separation of 3.33 eV for each oxidation state. The Ti 2p region was fit using two spin – split Gaussian peaks with the $p_{1/2}$ peak having a larger full – width half max due to a core hole effect.

Temperature Programmed Desorption (TPD)

All TPD experiments were performed in an in-house ultra-high vacuum (UHV) chamber with a base pressure of $< 1 \times 10^{-10}$ torr. Each sample was mounted on a removable sample holder where a chromel-alumel thermocouple wire and tungsten heating wires were sandwiched between the Pt/TiO_2 sample and a freshly cleaved HOPG sample of similar thickness to allow firm contact of the wires with the sample. Custom made tantalum foil clips and backing tantalum plates were used to compress the TiO_2 sample and backing HOPG in place. The Ta clips were fastened to the Ta backing plates with molybdenum screws to avoid seizing to after heating cycles.

Samples were annealed at 700K for 10 min prior to TPD experiments, unless otherwise stated. To obtain TPD spectra, samples were cooled ~110 K and exposed to D_2O (Aldrich, 99.96 atom % D) via a directional doser at a pressure of ~1 torr behind a 1 μm pinhole gasket. D_2O exposure was calculated as a function of time based on the effusion rate of the gas through the pinhole (3×10^{12} molecules/s); assuming a sticking coefficient of unity. Samples were heated to 700 K at 2 K/s and the amount of D_2O desorbing was monitored using a UTI 100C quadrupole mass spectrometer. Thermal desorption profiles were obtained from various exposures of D_2O ranging from 0.036 – 4.3 ($\times 10^{14}$ molecules).

Results

Photodeposition of Pt on TiO_2

Model nanoparticle/nanoparticle catalysts will require that the active metal (Pt) only occurs on the support material. TiO_2 is a classic oxide support and, because of the semiconducting properties of the material, can be illuminated with above – band gap radiation (> 3 eV) to deposit on the surface of the nanoparticles. TiO_2 nanoparticles used herein were supported on HOPG, which is

not photoactive, and therefore does not contribute charge carriers to facilitate deposition of Pt. In Figure 3.1, it is observed that the Pt is deposited only on the TiO_2 and not on the HOPG support. This is also confirmed by other studies in our group.[18]
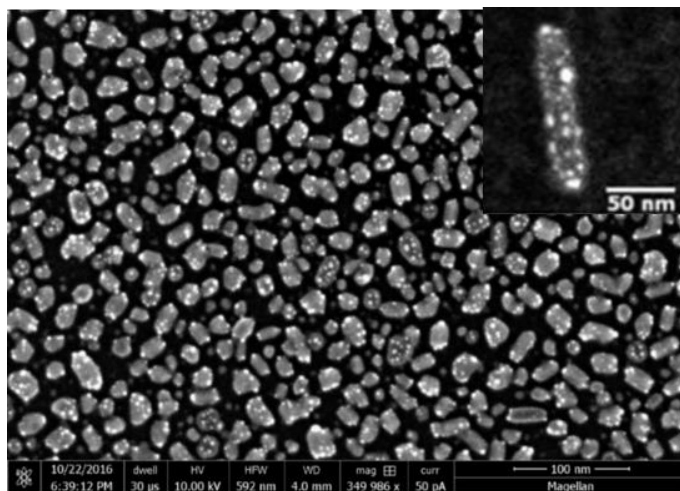
Figure 3.1: *Scanning electron image of Pt deposited on TiO_2. TiO_2 particles are ~ 20 nm in diameter with the Pt appearing as bright protrusions on the nanoparticles. Deposition time was 3 hours under 350 nm illumination*

To characterize the oxidation states of the photodeposited material, X – ray photoelectron spectroscopy (XPS) of the Pt/TiO_2 nanoparticles was carried out. In Figure 3.2a, a high-resolution spectra of the Pt 4f region shows a dominant set of spin - split peaks at 75.2 (Pt $4f_{7/2}$) and 78.5 eV (Pt $4f_{5/2}$), indicating the presence of Pt (IV) species at the surface. There is, potentially, a second contribution to the spectra at 72.9 eV which would indicate a Pt (II) species on the surface. The signal – to – noise ratio of this second state is low in comparison to the dominant, Pt (IV) and would require careful peak fitting to understand its contribution to the total spectra. This will be discussed later in this work. In Figure 3.2b the high – resolution spectra of the Ti 2p region shows a single dominant species at 458.2 (Ti $2p_{3/2}$) and 464.4 (Ti $2p_{1/2}$) eV indicating the presence of a fully oxidized Ti(IV) species. There is no indication of a Ti(III) state which would manifest as a shoulder on the low binding energy side of the Ti $2p_{3/2}$ peak at ~457 eV.
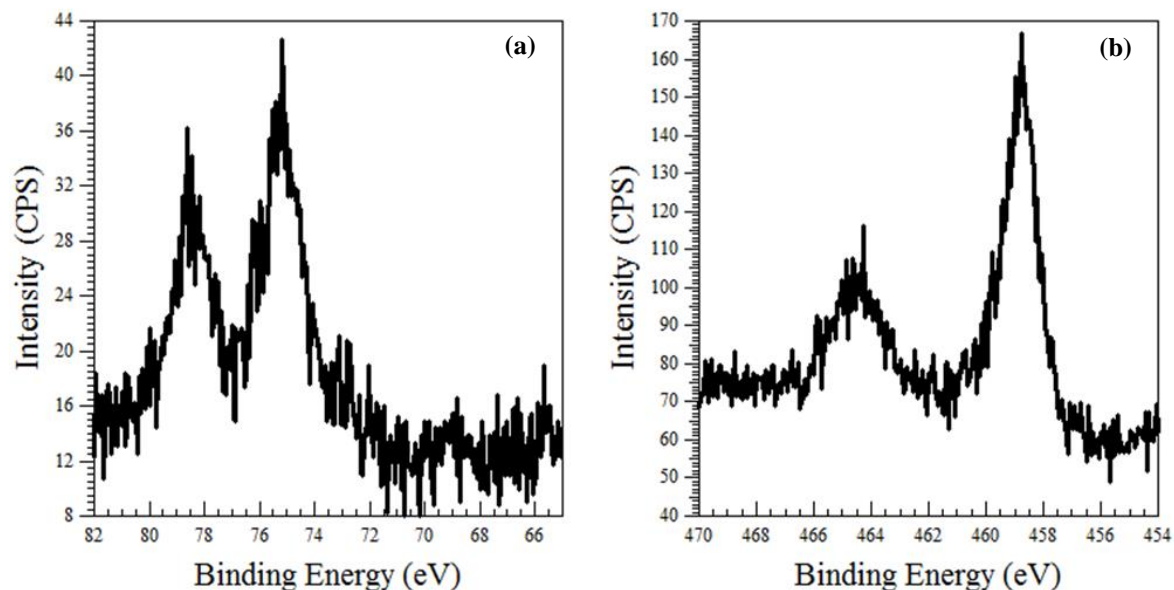
Figure 3.2: X – ray photoelectron spectra of (a) Pt 4f region and (b) Ti 2p region. The Pt peaks occur at 75.2 eV and 79.2 eV as spin – split pairs indicating the presence of Pt (IV). Ti 2p occurs at 458.2 eV and 464.4 eV indicating a fully oxidized Ti (IV) species as expected for these nanoparticles

Photodeposition of Pt generates multiple oxidation states depending on the pH of the solution. At low pH, it has been reported that there is a larger contribution from the lower oxidation states of Pt (II) and Pt (0) compared to the fully oxidized species. In Figure 3.3, the ratio of Pt oxidation states is shown as a function of the pH in the deposition solution.
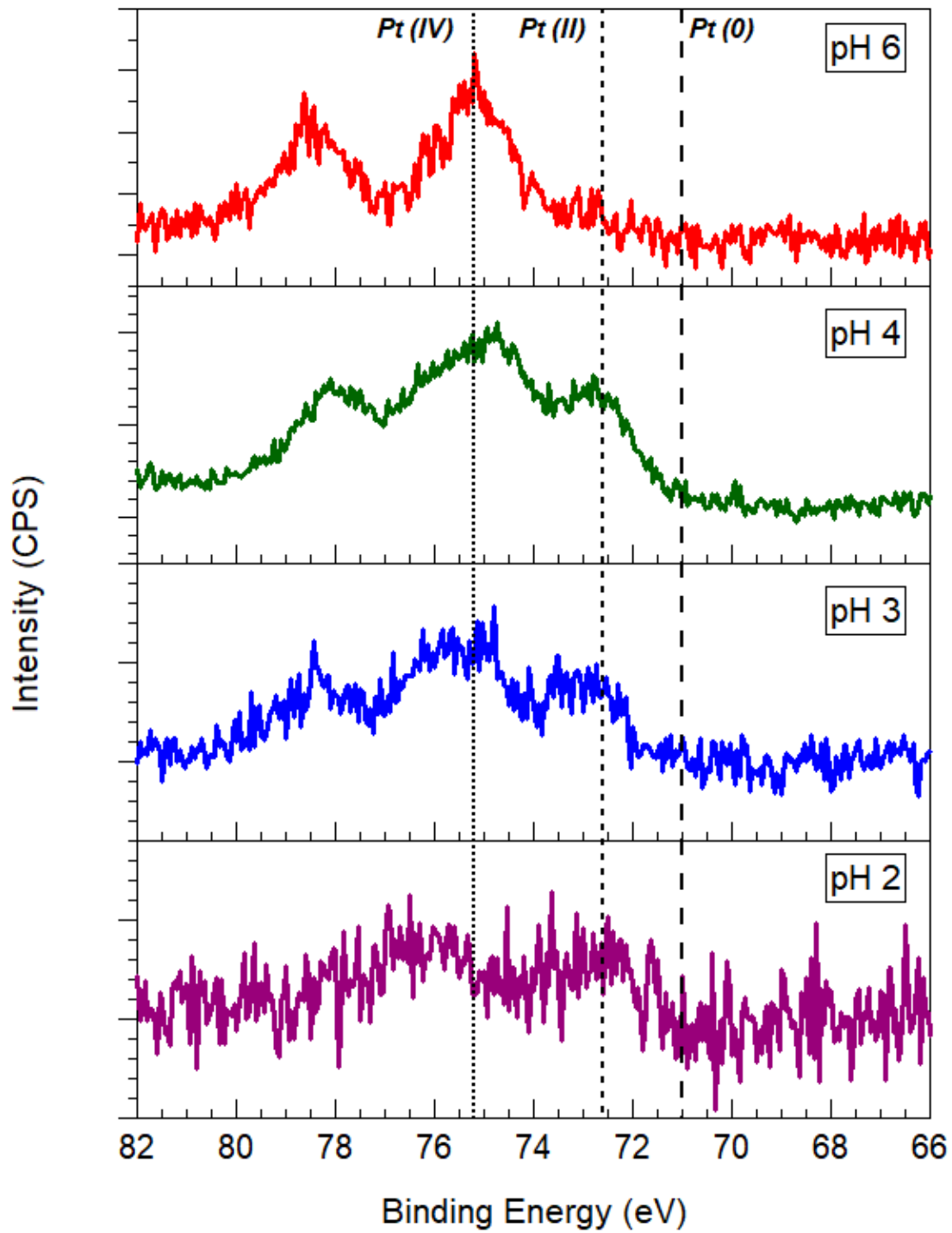
Figure 3.3: *Evolution of the Pt 4f region with respect to the pH of the deposition solutions. At low pH, there is significantly less Pt deposited on the surface of the TiO₂ however there is a greater number of lower oxidation states. At high pH, there is significantly more Pt deposited but with a greater amount of higher oxidation states. The amount of Ti from the Ti 2p region was constant within error for all spectra above.*

At pH 6, Pt (IV) is the only observable oxidation state in the spectra. As the pH of the deposition solution is lowered, higher contributions of Pt (II) are observed at the expense of Pt (IV), while Pt (0) remains below the background signal. The total Pt signal decreases as a function of pH, while the illumination time (3hrs) and Ti 2p signal remained constant. Decreased Pt signal at lower pH could be due to competing reactions at the interface, such as proton reduction, or an inhibition of the photodeposition mechanism. More detailed studies on the reaction mechanism could reveal the exact source of decreased signal intensity; however, it is beyond the scope of this work.

The deposition precursor used in this study utilizes Pt(II) chloride. In the literature, Pt(IV) chloride is often used to generate Pt nanoparticles on the surface of semiconductors.[24,25,34,35] In Figure 3.4, both Pt chloride species were used as the precursor under the same illumination, concentration and pH in solution.
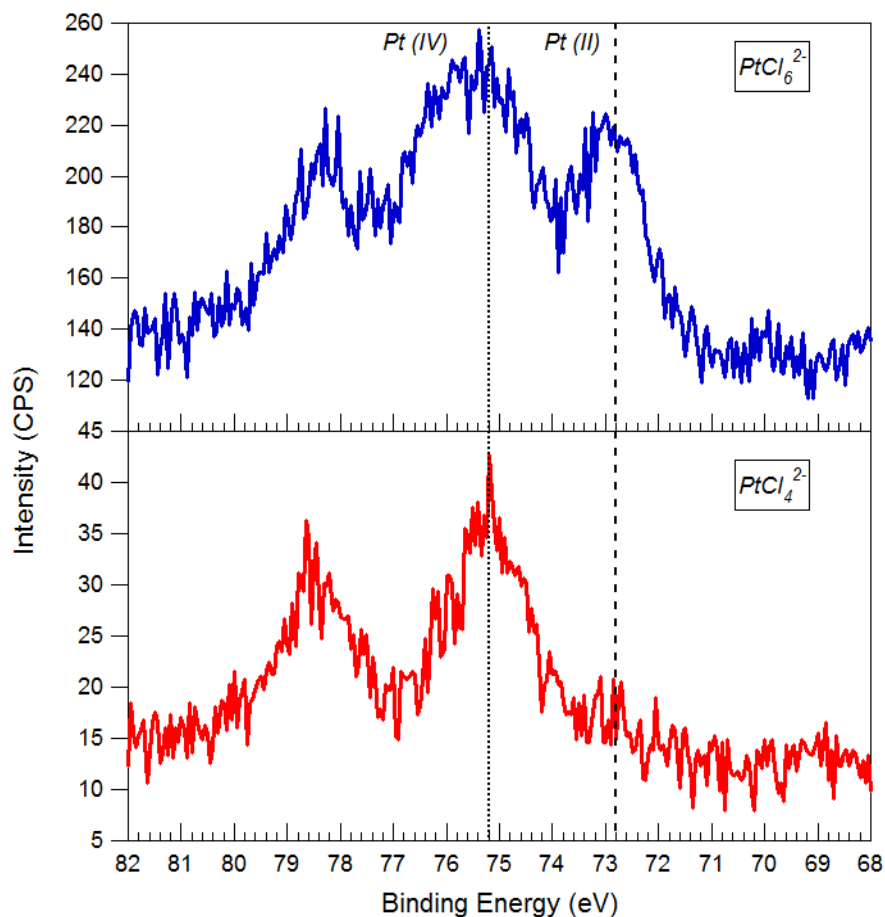
Figure 3.4: *Resulting Pt 4f spectra using different Pt chloride salts as the precursor for photodeposition. If Pt (IV) is the precursor there is a higher amount of Pt (II) present on the TiO₂ surface whereas when Pt (II) is used there is only Pt (IV) above the limit of detection. The illumination times were held constant at 3 hours and the pH of the solution was 6.*

When Pt(II) chloride is used, there is a single, dominant oxidation state observed in the high – resolution Pt 4f spectrum at 75.2 eV without any additional oxidation state observed above the background. However, when Pt (IV) chloride is used, there are multiple oxidation states contributing to the spectrum at 72.8 and 75.2 eV. The cause of the change in oxidation state distribution over the Pt spectra using different precursors could be rooted in the deposition mechanism. Competing deposition/reduction pathways on the surface of the TiO₂ determine the distribution of oxidation states present. Control over these pathways would allow for different

26

ratios of oxidation states to be present for different applications. It should be noted that there are no Pt(0) species observed when Pt(IV) or Pt(II) are used as a deposition precursor. A Pt (0) species has been observed at 71.2 eV from subsequent heating experiments (Figure 3.5), however no such contribution has been observed when only light is used to deposit the Pt on the surface.

Photoreduction of Pt Oxides on TiO$_2$

Initial photodeposition of Pt on the surface of TiO$_2$ nanoparticles shows that Pt(IV) and Pt(II) are the dominant contributors to the overall spectrum. The relative amounts of each species and further reduction to Pt(0) is controlled by the illumination of the samples. Removal of the precursor halts deposition and emphasizes the reduction pathway on the surface of TiO$_2$. In Figure 3.5, the photodeposition and subsequent photoreduction of a single sample over multiple irradiation times is shown.
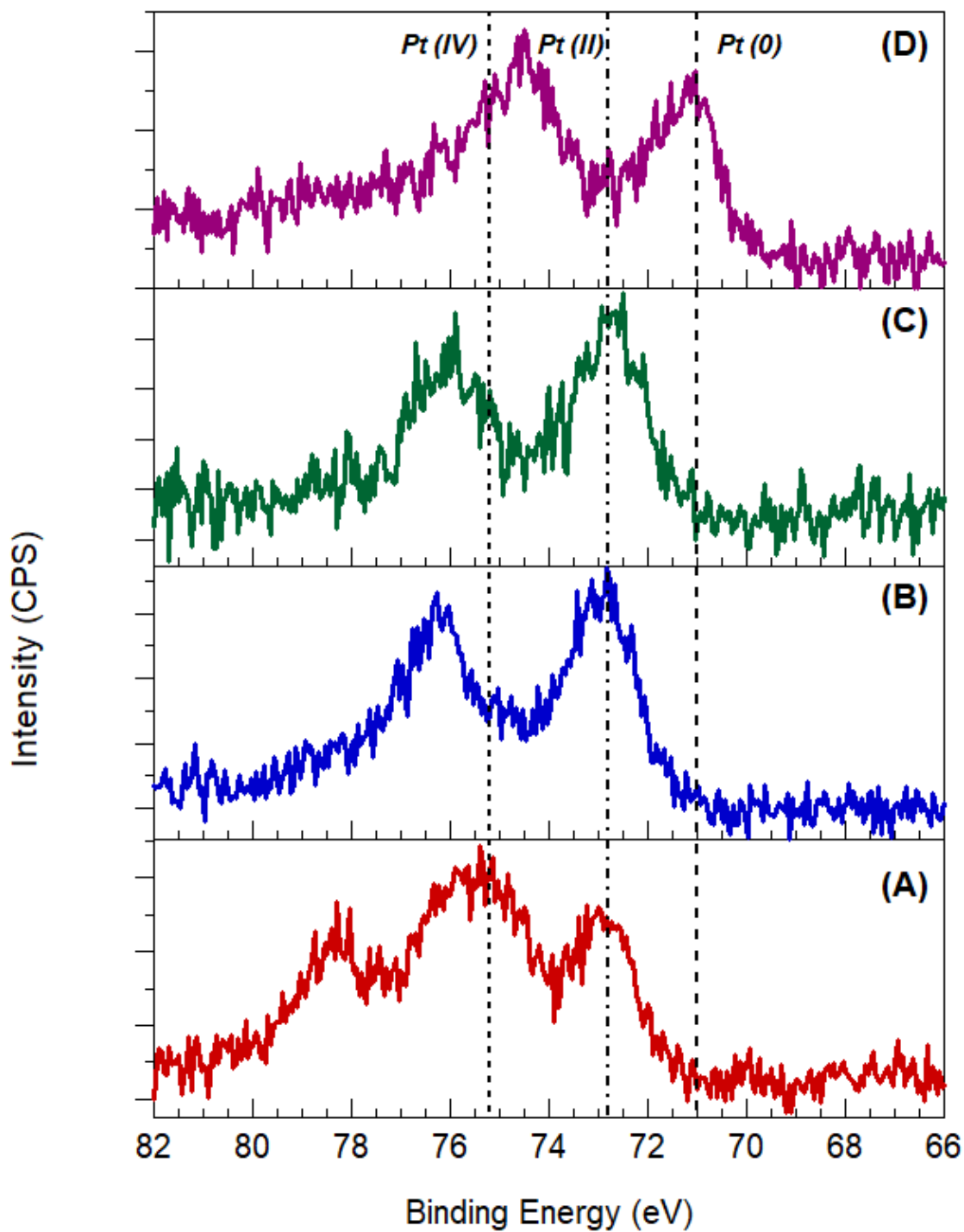
Figure 3.5: *Photoreduction of Pt on the surface of TiO₂. (a) Initial deposition of Pt (IV) for 3 hours followed by 3 hours of photoreduction without any precursor in the solution. (b) 3 hours of subsequent illumination for photoreduction. (c) 3 hours subsequent photoreduction (d) Pt/TiO₂ was annealed at 500K for 10 minutes to generate Pt (0) on the surface*

Removal of the precursor followed by irradiation of UV light shows that the distribution of oxidation states can be controlled by irradiation time. A small amount of methanol was added to the solution to scavenge any photogenerated holes that may be near the Pt and prevent re-oxidation or recombination with electrons. After the first 3-hour irradiation session, shown in Figure 3.5b, the major species present is the Pt(II) at 72.8 eV. The Pt(IV) has little contribution to the spectrum and there is no indication of a Pt(0) at lower binding energy. After a second irradiation of 3 hours, little changed with no indication of Pt(0) present on the surface. The Pt signal does not decrease significantly over the irradiation times indicating that it is stable on the surface and any Pt(IV) species are converted into Pt(II) without being dissolved into solution. The sample was transferred to a separate vacuum chamber where temperature programmed desorption (TPD) experiments were performed and the sample was heated to 500K for 10 minutes. Figure 3.5d shows the first indication of Pt(0) after the sample has been heated in the vacuum. The dominant species in the spectrum is the Pt(0) without any indication of other oxidized species at 72.8 or 75.2 eV.

Due to the transfer between vacuum chambers there was a concern that the Pt re-oxidized during its time in the ambient atmosphere. A Pt sample that was heated in the vacuum was left in ambient conditions to investigate the stability of the Pt particles. Figure 3.6 shows that when the sample was removed and left in ambient conditions for a week there was an increase in FWHM of the peak which may indicate an oxidation state change, however most the signal remains unchanged. After a second week in ambient conditions the major species is still Pt(0) and there appears to be a change in the symmetry of the peak. There is no indication of a full oxidation state change to Pt(II) species and the FWHM of the peak is within error of the first spectrum. Based on this data, there is little concern that the sample oxidized when it was transferred between chambers for different characterization.
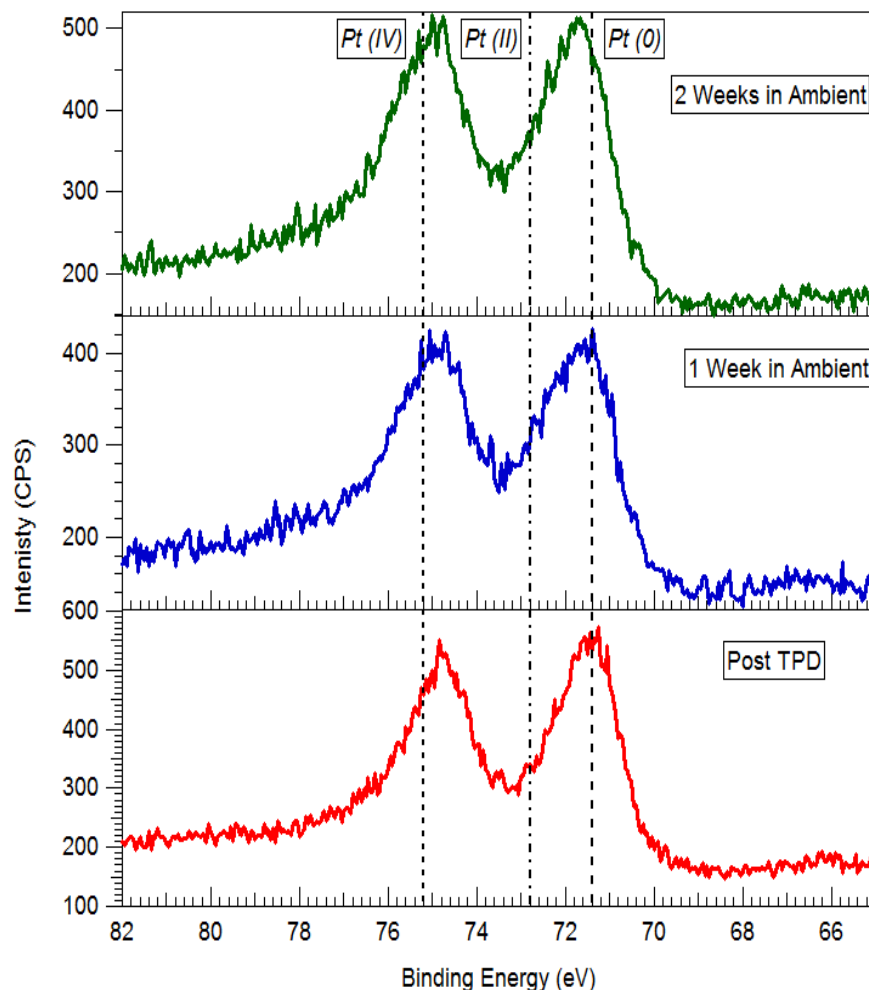
Figure 3.6: *Resulting Pt 4f spectra after Pt/TiO₂ was left in ambient conditions. After 1 week there is an increase in full width at half max which could indicate surface oxidation. After 2 weeks there is an asymmetry apparent in the spectrum which could indicate more oxidation of the surface. There is no clear indication of Pt (II) present on the surface*

Desorption of D_2O from Pt/TiO₂ Nanoparticles

Water is a standard, small probe molecule used to investigate the adsorption/desorption kinetics on the surface of a material. TPD of nanomaterials is an adolescent field due to the complexity of the surface and the difficulty in isolating the nanoparticles on an inert substrate. TiO₂ supported on HOPG is an ideal system for investigation of the desorption characteristics

because the particles are well dispersed and adhere to the support. In this work D_2O is used as a surrogate for H_2O to account for water present in the chamber background that would otherwise contribute to the overall desorption signal. For simplicity, D_2O will be referred to as water henceforth. In Figure 3.7, the water desorption spectrum of a single sample of TiO_2/HOPG and Pt/TiO_2/HOPG is shown.
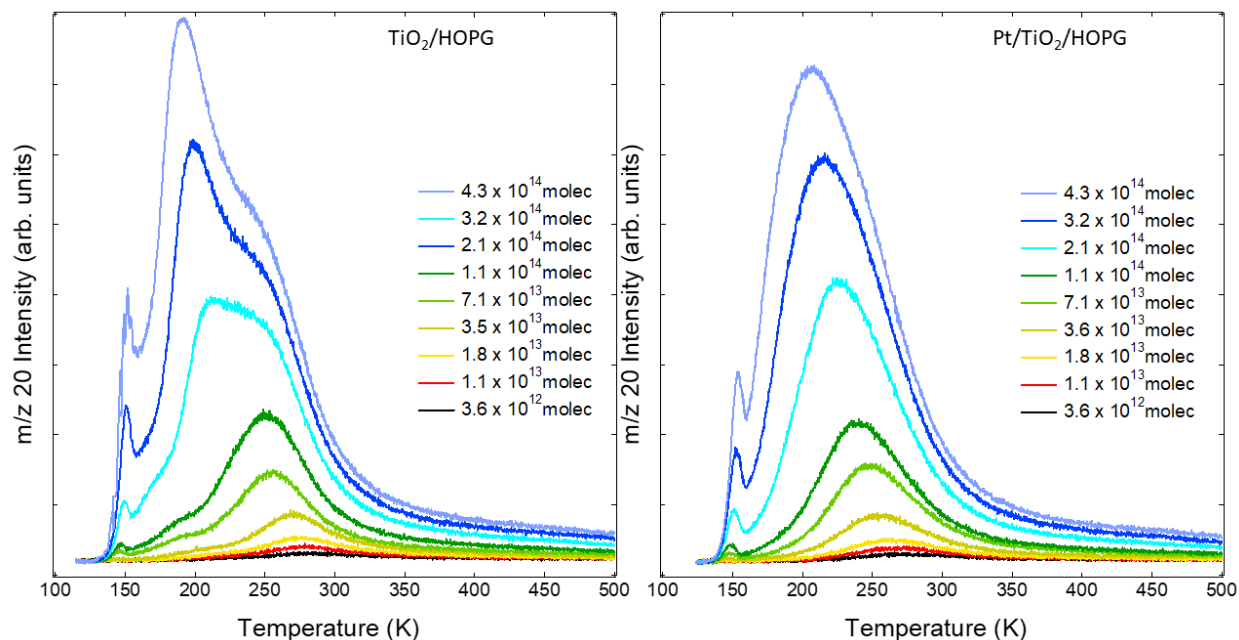
Figure 3.7: *Temperature desorption spectra of TiO₂/HOPG and Pt/TiO₂/HOPG. Desorption is given in number of molecules rather than monolayers due to the uncertainty in definition of a monolayer on these surfaces. Samples were annealed to 700 K prior to desorption studies*

The water desorption spectrum of TiO_2 nanoparticles shows four distinct areas of interest. The first is the lowest temperature peak corresponding to multilayer desorption of bulk water from the total surface.[36–39] The second peak starts at 200K and decreases in temperature to ~170 K at an exposure of 2.1 x 10^{14} molecules. This peak is attributed to defect sites caused by the oxygen plasma cleaning prior to imaging. The third peak starts at 275 K and saturates at ~250 K. This peak is attributed to Ti cation sites on the surface of TiO_2.[36–39] The final peak occurs later in the spectrum,

not appearing until 2.1 x 10^{14} molecules of water are exposed to the surface, at ~ 200 K. This peak is attributed to oxygen anion sites present on a rutile TiO_2 surface.[36–39] There is little contribution from the underlying HOPG in the spectra shown in Figure 7. This is because during particle deposition, defect sites promote formation and growth of TiO_2 on the HOPG and are thus blocked by TiO_2 nanoparticles. When Pt is deposited on the surface and the sample is returned to the TPD chamber, there are two key features observed in Figure 3.7. The first is the low temperature multilayer peak and the second is the broad feature beginning at ~275 K, ending at ~225 K attributed to Ti cation sites present on the TiO_2.

Discussion

Pt Oxidation State Upon Deposition

Many studies in the literature use colloid solutions to investigate the effect of photodepositing Pt on the surface of TiO_2 nanoparticles. Long deposition times are routinely used to place a significant amount of the active material on the nanoparticles. Physical vapor deposition of TiO_2 nanoparticles on the surface of an inert material generates a more reliable and reproducible method to investigate the effects of catalyst/substrate interactions at the nanoscale. It also allows for more flexibility to systematically investigate the nanoparticles after any chemical or heat treatment that may be used to change the interface.

The initial oxidation state of Pt upon deposition is a Pt(IV) species as observed in Figures 3.2 and 3.3. Given that the Pt source for these experiments was Pt(II) chloride, the deposition of only Pt (IV) is somewhat unexpected if electrons are what is driving the photodeposition on the surface. Oxidation of the Pt is likely to occur either at the interface of TiO_2 or within the solution prior to deposition. Photogenerated holes in the TiO_2 are known to create hydroxyl radicals that readily

oxidize the Pt in solution if they desorb prior to interaction.[22,40-49] However, because the Pt only appears on the surface of the TiO_2, it is more likely that the oxidation happens at the interface of TiO_2 rather than in solution. Additionally, the solutions are always prepared fresh before deposition to prevent any oxidation of the precursor prior to illumination.

As was observed in Figure 3.3, lowering the pH of the solution creates more reduced species on the surface of TiO_2 under the same illumination time. However, there is significantly less Pt deposited over this time compared to higher pH solutions. This could indicate that the deposition pathway is hindered or that the mechanism for deposition has been modified to include a slower reaction step. The premise that hydroxyl radicals are responsible for the deposition, as stated above, would hold true when the pH is decreased. Protons in solution would quench the radicals, forming water, rather than allowing the radicals to oxidize Pt depositing it on the surface. The small amount of Pt that does get deposited would be reduced by photogenerated electrons leading to a lower concentration of Pt(II) present on the surface, which is clearly observed in Figure 3.3. A direct reduction pathway of the Pt(II) in solution would generate Pt(0) on the TiO_2 however this is not observed in this study.

The precursor species was expected to have a direct effect on the deposition of Pt on the surface of TiO_2 nanoparticles. In Figure 3.4, the deposition precursor is changed from a Pt(II) chloride to a Pt(IV) chloride to investigate this effect. The mixture in the oxidation states observed when similar concentrations and time of deposition are used indicate that the Pt is deposited as a Pt(IV) and is subsequently reduced on the surface of TiO_2. This indicates that the Pt(II) species is oxidized to Pt(IV) upon deposition to the nanoparticles.

Photoreduction of Pt Oxides

Illumination of the TiO_2 produces both electrons and holes capable of driving chemical reactions on the surface of the nanoparticles. There is significant precedent showing photogenerated holes drive oxidation reactions near the interface of TiO_2, however the photogenerated electrons also have the capability to drive a reduction reaction given an appropriate amount of time before recombination ends that pathway. In the previous section, the photogenerated holes drive the photodeposition mechanism on the surface of TiO_2, and due to the shift to lower binding energy in the Pt 4f regions, there is a reduction mechanism observed as well. Figure 3.5 demonstrates how the photogenerated electrons can also be utilized to drive a reduction reaction on the interface. In Figure 3.5a, the photodeposition of Pt on the nanoparticles is shown to generate a mixture of Pt (IV)/(II) after photoreduction in 1mM aqueous solution of methanol. Methanol was added to scavenge holes at the interface and lead to a higher probability of reduction by the electrons rather than recombination.[50] Two additional irradiation times (3hrs) are shown in Figure 3.5b and c. The relative mixture of Pt(IV)/(II) shifts significantly to show almost exclusively Pt(II), but interestingly, there is no presence of Pt (0) at the longer irradiation times. The lack of Pt (0) could be due to increased recombination of the carriers rather than reduction to Pt (0). The reduction potential of Pt(II)/(0) is 1.2V (vs. NHE), which should allow the reduction of the Pt with ease, however there has also been work in the literature that shows a large surface dipole (~1.3 D) is generated by the $Pt(II) - O_x$ bond.[50,51] This dipole would hinder charge transfer across the interface and increase recombination of charge carriers rather than reduce to Pt(0). Pt(0) is still attainable by heating within the vacuum of the TPD chamber. The sample is only heated to 500 K to promote reduction, and based on Figure 3.5d, there is complete conversion to Pt (0) with no other oxidation states present at the interface. A low temperature is desired for the reduction as

TiO$_2$ is capable of strong – metal support interactions (SMSI) with Pt and could form an oxide shell around the nanoparticles reducing, or eliminating, their ability to catalyze heterogenous oxidation reactions such as the oxidation of CO to CO$_2$. Typically, the SMSI effects begin to appear closer to 800 K on single crystal studies and there should be little concern when using temperatures near 500 K. The Ti 2p spectra of all studies show no contribution of a Ti(III) in the TiO$_2$ which would appear as a shoulder on the low binding energy side of the Ti 2p$_{3/2}$ peak to indicate a SMSI effect.

Desorption of Water from TiO$_2$ and Pt/TiO$_2$

Utilization of water as a small probe molecule to understand the desorption kinetics from the nanoparticles is unique to this system because each surface can be investigated systematically once a new material is added. Despite the non – ideal, *ex situ* deposition procedures, the TPD spectra provides unique insight into the effect of the presence of Pt nanoparticles on the TiO$_2$. In Figure 3.7, there is clear suppression of the oxygen anion peak, which occurs with higher water doses at ~200K when Pt is present on the surface of TiO$_2$. The defect site peak, which occurs at low doses beginning at 200K, is completely removed when Pt is present on the surface. A closer look at the change in the desorption spectra is shown below in Figure 3.8.
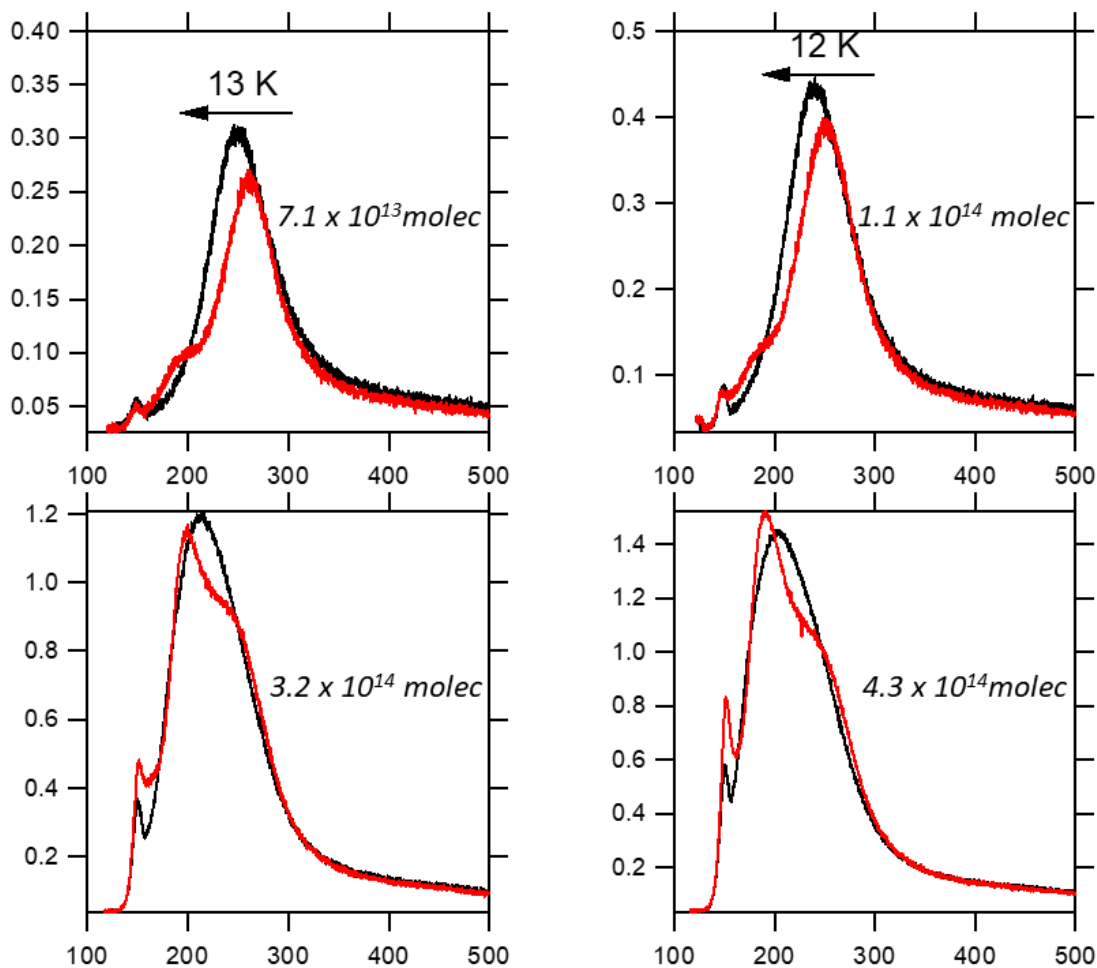
Figure 3.8: *Selected exposures to D_2O that show the shift in the peak at 250K to lower temperatures by 13K. The main multilayer peak shows up at ~150K which is temperature independent.*

At the low doses, there is a well – resolved peak at ~200 K on the TiO_2 nanoparticles but is absent when Pt is added. The Pt nanoparticles could be depositing on these defect sites and would therefore remove that peak from the spectrum. At higher doses, a new peak appears that is also removed from the spectrum when Pt is present. These are oxygen anion sites and could be where the Pt resides on the surface of the TiO_2 nanoparticle. If photogenerated holes are the main driver of Pt deposition, then it is likely that defects and oxygen anion sites would be the primary site of charge transfer. Defect sites are known to trap photogenerated carriers and could easily be a source

of hydroxyl formation. Additionally, an anion site would be a more likely place to have holes transfer rather than a cation site, such as those observed in the large peak at 250K.

The cation desorption peak at 250K also shifts ~13K lower in temperature with Pt on the surface relative to without. This could be due to the proximity of the Pt to the cation sites. If Pt is close to these sites, it may hydrogen bond with water that is adsorbed and weaken the interaction with the TiO_2. It may also be the case that there is a second contribution within that spectral width that originates from the adsorption of water with Pt. This may be the cause of the peak broadening. Comparison with single crystal Pt desorption would provide greater insight into the cause of the shift of this peak.

Conclusion

TiO_2 nanoparticles and their interactions with Pt are often studied on colloidal solutions that are difficult to modify after the Pt is photodeposited on the surface. In this work, we used a physical vapor deposition method to deposit TiO_2 nanoparticles on HOPG, which was followed by photodeposition of Pt on the surface of TiO_2. The Pt is deposited as Pt(IV) by utilizing the electrochemical energy of the photogenerated holes to create hydroxyl radicals on the TiO_2. Photoreduction of Pt(IV) to (II) can be easily achieved, while Pt(0) was not observed under these conditions. A low temperature anneal (500K) in the vacuum generates the Pt(0) species, which would be free of any oxide shell due to strong – metal support interactions. Desorption experiments of the TiO_2 and Pt/TiO_2 show significant changes in the water desorption kinetics with and without the presence of Pt on the surface. Elimination of defect and oxygen anion peaks from the spectrum indicate Pt is deposited at these sites preferentially compared to Ti cation sites on the nanoparticles.

Additionally, a 13K shift to lower temperatures indicates the weakening of the interaction at the

Ti cation sites due to the Pt.

References

1   B. C. Gates, Supported Metal Clusters: Synthesis, Structure, and Catalysis, *Chem. Rev.*,
     1995, **95**, 511–522.

2   G. A. Somorjai, The surface science of heterogeneous catalysis, *Surf. Sci.*, 1994, **299**–**300**,
     849–866.

3   S. Royer and D. Duprez, Catalytic Oxidation of Carbon Monoxide over Transition Metal
     Oxides, *ChemCatChem*, 2011, **3**, 24–65.

4   E. Lundgren, C. Zhang, L. R. Merte, M. Shipilin, S. Blomberg, U. Hejral, J. Zhou, J.
     Zetterberg and J. Gustafson, Novel in Situ Techniques for Studies of Model Catalysts,
     Acc. Chem. Res., 2017, acs.accounts.7b00281.

5   M. A. van Spronsen, J. W. M. Frenken and I. M. N. Groot, Surface science under reaction
     conditions: CO oxidation on Pt and Pd model catalysts, *Chem. Soc. Rev.*, ,
     DOI:10.1039/C7CS00045F.

6   W. Weiss and W. Ranke, Surface chemistry and catalysis on well-defined epitaxial iron-
     oxide layers, *Prog. Surf. Sci.*, 2002, **70**, 1–151.

7   Q. Fu and T. Wagner, Interaction of nanostructured metal overlayers with oxide surfaces,
     Surf. Sci. Rep., 2007, **62**, 431–498.

8   S. Porsgaard, L. K. Ono, H. Zeuthen, J. Knudsen, J. Schnadt, L. R. Merte, J. Chevallier, S.
     Helveg, M. Salmeron, S. Wendt and F. Besenbacher, In Situ Study of CO Oxidation on
     HOPG-Supported Pt Nanoparticles, *ChemPhysChem*, 2013, **14**, 1553–1557.

9   A. S. M. Nur, E. Funada, S. Kiritoshi, A. Matsumoto, R. Kakei, S. Hinokuma, H. Yoshida
     and M. Machida, Phase-Dependent Formation of Coherent Interface Structure between
     PtO2 and TiO2 and Its Impact on Thermal Decomposition Behavior, *J. Phys. Chem. C*,

2017, acs.jpcc.7b10858.

10 B. G. C. Bond, Supported Metal Catalysts : Some Unsolved Problems.

11 S. J. Tauster, S. C. Fung, R. T. Baker and J. A. Horsley, Strong interactions in supported-metal catalysts, *Science (80-.).*, 1981, **211**, 1121–1125.

12 G. N. Vayssilov, Y. Lykhach, A. Migani, T. Staudt, G. P. Petrova, N. Tsud, T. Skála, A. Bruix, F. Illas, K. C. Prince, V. Matolı´n, K. M. Neyman and J. Libuda, Support nanostructure boosts oxygen transfer to catalytically active platinum nanoparticles, *Nat Mater*, 2011, **10**, 310–315.

13 S. Porsgaard, L. R. Merte, L. K. Ono, F. Behafarid, J. Matos, S. Helveg, M. Salmeron, B. Roldan Cuenya and F. Besenbacher, Stability of Platinum Nanoparticles Supported on SiO2/Si(111): A High-Pressure X-ray Photoelectron Spectroscopy Study, *ACS Nano*, 2012, **6**, 10743–10749.

14 H.-J. Freund, The Surface Science of Catalysis and More, Using Ultrathin Oxide Films as Templates: A Perspective, *J. Am. Chem. Soc.*, , DOI:10.1021/jacs.6b05565.

15 S. J. Tauster and S. C. Fung, Strong Metal-Support Interactions - Occurrence among Binary Oxides of Groups Iia-Vb, *J. Catal.*, 1978, **55**, 29–35.

16 S. J. Tauster, S. C. Fung and R. L. Garten, Strong Metal-Support Interactions - Group-8 Noble-Metals Supported on Tio2, *J. Am. Chem. Soc.*, 1978, **100**, 170–175.

17 S. J. Tauster, STRONG METAL-SUPPORT INTERACTIONS, *Acc. Chem. Res.*, 1987, **20**, 389–394.

18 J. Taing, M. H. Cheng and J. C. Hemminger, Photodeposition of Ag or Pt onto TiO2 Nanoparticles Decorated on Step Edges of HOPG, *ACS Nano*, 2011, **5**, 6325–6333.

19 S. Miyashita, M. Wakisaka, A. Iiyama and H. Uchida, Analysis of the Surface Oxidation

Process on Pt Nanoparticles on a Glassy Carbon Electrode by Angle-Resolved, Grazing-Incidence X-ray Photoelectron Spectroscopy, *Langmuir*, 2017, acs.langmuir.7b01446.

20   T. Rajesh, A. K. Rajarajan, C. S. Gopinath and R. N. Devi, Evidence of Cationic Pt Active for Water–Gas Shift Reaction: Pt-Doped BaCeO3 Perovskite, *J. Phys. Chem. C*, 2012, **116**, 9526–9532.

21   E. Kemppainen, J. Halme and P. D. Lund, An analytical model of hydrogen evolution and oxidation reactions on electrodes partially covered with a catalyst, *Phys. Chem. Chem. Phys.*, 2016, **18**, 13616–13628.

22   K. Wenderich and G. Mul, Methods, Mechanism, and Applications of Photodeposition in Photocatalysis: A Review, *Chem. Rev.*, 2016, **116**, 14587–14619.

23   A. Henglein and M. Giersig, Reduction of Pt(II) by H2: Effects of Citrate and NaOH and Reaction Mechanism, *J. Phys. Chem. B*, 2000, **104**, 6767–6772.

24   C. Sungbom, M. Kawai and K. Tanaka, XPS Studies of the Platinum Species Photodeposited on Titania from Aqueous Chloroplatinic Acid, *Bull. Chem. Soc. Jpn.*, 1984, **57**, 871–872.

25   T. Yoshida, Y. Minoura, Y. Nakano, M. Yamamoto, S. Yagi and H. Yoshida, XAFS study on a photodeposition process of Pt nanoparticles on TiO $_2$ photocatalyst, *J. Phys. Conf. Ser.*, 2016, **712**, 12076.

26   F. Pesty, H.-P. Steinrück and T. E. Madey, Thermal stability of Pt films on TiO2(110): evidence for encapsulation, *Surf. Sci.*, 1995, **339**, 83–95.

27   J. Lee and W. Choi, Photocatalytic Reactivity of Surface Platinized TiO2: Substrate Specificity and the Effect of Pt Oxidation State, *J. Phys. Chem. B*, 2005, **109**, 7399–7406.

28   K. Angermund, M. Bühl, U. Endruschat, F. T. Mauschick, R. Mörtel, R. Mynott, B.

Tesche, N. Waldöfner, H. Bönnemann, G. Köhl, H. Modrow, J. Hormes, E. Dinjus, F. Gassner, H.-G. Haubold, T. Vad and M. Kaupp, In Situ Study on the Wet Chemical Synthesis of Nanoscopic Pt Colloids by 'Reductive Stabilization', *J. Phys. Chem. B*, 2003, **107**, 7507–7515.

29   M. QAMAR and A. K. GANGULI, Self-assembling behaviour of Pt nanoparticles onto surface of TiO2 and their resulting photocatalytic activity, *Bull. Mater. Sci.*, 2013, **36**, 945–951.

30   Z. Li, K. Yang, G. Liu, G. Deng, J. Li, G. Li, R. Yue, J. Yang and Y. Chen, Effect of reduction treatment on structural properties of TiO2 supported Pt nanoparticles and their catalytic activity for benzene oxidation, *Catal. Letters*, 2014, **144**, 1080–1087.

31   A. Mondal and N. R. Jana, Effect of size and oxidation state of platinum nanoparticles on the electrocatalytic performance of graphene-nanoparticle composites, *RSC Adv.*, 2015, **5**, 85196–85201.

32   F. Şen and G. Gökağaç, Different Sized Platinum Nanoparticles Supported on Carbon: An XPS Study on These Methanol Oxidation Catalysts, *J. Phys. Chem. C*, 2007, **111**, 5715–5720.

33   F. Zhang, J. Chen, X. Zhang, W. Gao, R. Jin, N. Guan and Y. Li, Synthesis of Titania-Supported Platinum Catalyst: The Effect of pH on Morphology Control and Valence State during Photodeposition, *Langmuir*, 2004, **20**, 9329–9334.

34   F. Mahlamvana and R. J. Kriek, Photocatalytic reduction of platinum(II and IV) from their chloro complexes in a titanium dioxide suspension in the absence of an organic sacrificial reducing agent, *Appl. Catal. B Environ.*, 2014, **148**–**149**, 387–393.

35   X. Chanjuan, C. Zhengshi, L. Qinglin and J. Zhensheng, Effects of H+, Cl− and

CH3COOH on the photocatalytic conversion of PtCl62− in aqueous TiO2 dispersion, *J. Photochem. Photobiol. A Chem.*, 1995, **87**, 249–255.

36   M. B. Hugenschmidt, L. Gamble and C. T. Campbell, The interaction of H2O with a TiO2(110) surface, *Surf. Sci.*, 1994, **302**, 329–340.

37   M. A. Henderson, An HREELS and TPD study of water on TiO2(110): the extent of molecular versus dissociative adsorption, *Surf. Sci.*, 1996, **355**, 151–166.

38   L.-M. Liu, C. Zhang, G. Thornton and A. Michaelides, Structure and dynamics of liquid water on rutile $TiO_2(110)$, *Phys. Rev. B*, 2010, **82**, 161415.

39   Y. Suda and T. Morimoto, Molecularly adsorbed water on the bare surface of titania (rutile), *Langmuir*, 1987, **3**, 786–788.

40   K. Shirai, G. Fazio, T. Sugimoto, D. Selli, L. Ferraro, K. Watanabe, M. Haruta, B. Ohtani, H. Kurata, C. Di Valentin and Y. Matsumoto, Water-Assisted Hole Trapping at the Highly Curved Surface of Nano-TiO $_2$ Photocatalyst, *J. Am. Chem. Soc.*, 2018, jacs.7b11061.

41   O. I. Micic, Y. Zhang, K. R. Cromack, A. D. Trifunac and M. C. Thurnauer, Trapped holes on titania colloids studied by electron paramagnetic resonance, *J. Phys. Chem.*, 1993, **97**, 7277–7283.

42   Y. Nosaka, S. Komori, K. Yawata, T. Hirakawa and A. Y. Nosaka, Photocatalytic ˙OH radical formation in TiO $_2$ aqueous suspension studied by several detection methods, *Phys. Chem. Chem. Phys.*, 2003, **5**, 4731–4735.

43   Á. Valdés, Z.-W. Qu, G.-J. Kroes, J. Rossmeisl and J. K. Nørskov, Oxidation and Photo-Oxidation of Water on TiO 2 Surface, *J. Phys. Chem. C*, 2008, **112**, 9872–9879.

44   R. S. Smith, Z. Li, L. Chen, Z. Dohnálek and B. D. Kay, Adsorption, Desorption, and Displacement Kinetics of H_2O and CO_2 on TiO_2 (110), *J. Phys. Chem. B*, 2014, **118**, 8054–8061.

45   S. Tan, H. Feng, Y. Ji, Y. Wang, J. Zhao, A. Zhao, B. Wang, Y. Luo, J. Yang and J. G. Hou, Observation of photocatalytic dissociation of water on terminal Ti sites of TiO_2(110)-1 × 1 surface, *J. Am. Chem. Soc.*, 2012, **134**, 9978–9985.

46   P. Salvador, On the nature of photogenerated radical species active in the oxidative degradation of dissolved pollutants with TiO_2 aqueous suspensions: A revision in the light of the electronic structure of adsorbed water, *J. Phys. Chem. C*, 2007, **111**, 17038–17043.

47   F. Liu, N. Feng, Q. Wang, J. Xu, G. Qi, C. Wang and F. Deng, Transfer Channel of Photoinduced Holes on a TiO_2 Surface As Revealed by Solid-State Nuclear Magnetic Resonance and Electron Spin Resonance Spectroscopy, *J. Am. Chem. Soc.*, 2017, **139**, 10020–10028.

48   C. D. Jaeger and A. J. Bard, Spin trapping and electron spin resonance detection of radical intermediates in the photodecomposition of water at titanium dioxide particulate systems, *J. Phys. Chem.*, 1979, **83**, 3146–3152.

49   a Imanishi, K. T. Okamura, N. Ohashi, R. Nakamura and Y. Nakato, Mechasnim of water photooxidation reaction at atomically flat TiO(utaile(110) and (100) surfaces:dependence on solution pH, *J.Amer. Chem.Soc.*, 2007, **129**, 11569.

50   M. Alsabet, M. Grden and G. Jerkiewicz, Comprehensive study of the growth of thin oxide layers on Pt electrodes under well-defined temperature, potential, and time conditions, *J. Electroanal. Chem.*, 2006, **589**, 120–127.

51   B. Kraeutler and A. J. Bard, Heterogeneous photocatalytic preparation of supported

       catalysts. Photodeposition of platinum on titanium dioxide powder and other substrates, *J.*

       Am. Chem. Soc., 1978, **100**, 4317–4318.

Chapter 4: Characterization of Fe^{2+} Solutions with Liquid Jet X – ray Photoelectron to Understand Fenton Chemistry at Air – Liquid Interfaces and the Effects of Halide Ions

Introduction

Transition metal complexes in aqueous solution are central to many different scientific processes, ranging from corrosion science to biochemistry to atmospheric reactions. Iron is one of the most ubiquitous transition metals and has been the focus of intense theoretical and experimental work. Its two most stable oxidation states in aqueous solution (Fe(II)/(III)) are very sensitive to the local chemical environment surrounding it. Several different chemical species are known for Fe(III) complexes that depend on the pH, ions in solution and the coordination environment of the Fe center in the solution.[1–4] Fe^{2+} ions have garnered less attention due to its fast oxidation to Fe (III), but still have several complex equilibria related to pH and ions present in solution. These equilibria have a profound effect on chemistry around the Fe containing species in solution. One such reaction is the Fenton reaction that utilizes and Fe(II) complex in aqueous solution as shown in Reaction 1.1:

Fenton Reaction: $Fe(II)_{(aq)} + H_2O_{2(aq)} \rightarrow Fe(III)_{(aq)} + \cdot OH_{(aq)} + OH^-_{(aq)}$ (1.1)
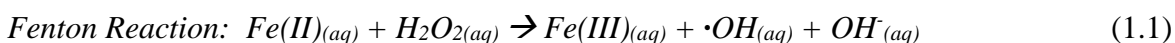
Fenton and photo – Fenton reactions that are catalyzed by iron – containing species have recently gathered significant attention in the literature, especially in atmospheric chemistry. These species are important for generating highly reactive oxidizing species that later go on to form secondary organic aerosols (SOA) from either small, organic materials in solution, or from carboxylic ligands attached to the metal center.[5] The mechanism in the formation of these species is reliant on many of the same parameters that modify the chemical environment of the iron center in solution. Additionally, the rate of the reaction can be dependent on many of the dissolved solutes

that are commonly found in atmospheric systems. Dissolved anions such as chloride and bromide ions can serve as both coordination ligands to the metal center and participants in the mechanism for the reactions.[4] For instance, chloride ions have been shown to hinder hydroxyl radical formation in the Fenton process whereas bromine shows little effect on the rate.[4] Investigation into the dependence of the reaction mechanism on the chemical environment of the first solvation sphere is a crucial first step to understanding the oxidative processes that are reliant on these Fe - species.

Fundamental work focused on characterization and understanding of the first solvation sphere of $Fe^{3+/2+}$ complexes has relied on the interpretation of the electronic structure through ultraviolet/visible, electron paramagnetic resonance (EPR) and Mössbauer spectroscopies or by using x – ray absorption spectroscopy to evaluate the extended structure of the ligand environment and the outer solvation spheres.[6–9] The accepted primary coordination sphere of Fe(II/III) coordination complexes in acidic aqueous solution are an octahedral arrangement of aqua ligands around a central Fe center.[10–14] These aqua ligands are, inherently, sensitive to the pH of the solution. As the pH increases, the aqua ligands to the Fe^{2+} center will deprotonate to form coordinated hydroxido ligands, before eventually collapsing to insoluble Fe^{2+}- hydroxido nanoparticles.[3,15,16] Fe^{3+} complexes have more complicated aqueous solution chemistry as Fe^{3+}-hydroxyl complexes are stable as monomers in solution, but can also form dimers, trimers and polymers.[2] The presence of small inorganic ions in solution, especially Cl^- ions, has been shown to generate large networks of polymeric species in solution by the use of resonant X – ray absorption spectroscopy on a liquid jet solution.[17] Small, inorganic ions are also known to have an affinity for the air – water interface and significantly affect the chemistry near the surface. [18–23]

Chemistry at the air – water interface is paramount in atmospheric chemistry; however, few studies have been able to investigate the solvation sphere of Fe(II) species and translate observational knowledge to reactions that occur at the interface. Much of the work has focused on the bulk species in solution and very few have investigated the active species at this interface. More recent work utilizing mass spectrometry of $FeCl_2$ solutions has inferred surface reactivity from low gas dosing concentrations. Notably, this technique is not inherently surface sensitive in comparison to XPS and cannot probe the solvation sphere of molecular species in solution.[23] Additionally, the ability of the halide ions to coordinate to Fe(II) centers could have significant effects on both the Fenton reaction and any chemistry that involves the halide ion at the interface. In the work described here, we utilize a lab – based liquid jet ambient pressure X – ray photoelectron spectrometer (LJ – APXPS), to investigate the solvation sphere of Fe(II) species at the solution/vapor interface. Modification of the solution interface composition and chemistry with the addition of Cl^- and Br^- ions to the aqueous solution is shown to influence the Fe(II) inner solvation sphere and the concentration of the halide species at the interface. This finding will have significant effects on the understanding of Fenton and air – water interface chemistry of oxidative atmospheric reactions. Additional work has been carried out at the Advanced Light Source (ALS) to investigate the distribution of Cl and Fe species as a function of depth with respect to the liquid – vacuum interface by varying the probe depth of the XPS experiment.[21,24–26] These experiments illustrate the first molecular picture of small, coordinating ions on the solvation sphere of Fe^{2+} ions and the consequences with respect to the air – water interface.

Experimental

The instrumental details of the first lab – based liquid jet XPS are documented in Chapter 2. Photoelectron spectra of the inner shell orbitals of iron (2p), oxygen (1s), chlorine (2p) and

bromine (3d) in aqueous solution were performed using a 20 μm diameter liquid jet with Al kα X -rays (1486 eV) at a pass energy of 50 eV. The background pressure of the ambient pressure liquid – jet chamber was held constant at 4 mbar. The x – ray spot size was 40 μm in diameter and all spectra were collected after optimization of the O 1s liquid water peak at 533.5 eV. No additional charge correction was applied, and all binding energies are reported with respect to the O1s gas phase water peak at 535.5 eV.

Details of the liquid jet setup are described in Appendix I. Briefly, the liquid microjet is cooled to 6°C and run at a constant flow rate of 0.4 mL/min. The jet position is oriented normal to the detection axis of the hemispherical electron analyzer. The electron analyzer entrance aperture was 300 μm in diameter and the differentially pumped chambers were operated a pressure $< 5 \times 10^{-4}$ mbar during the experiment. The analyzer pressure and x – ray source was operated $< 5 \times 10^{-8}$ mbar and $< 5 \times 10^{-7}$ mbar, respectively during the experiment.

All spectra were fit using CasaXPS software and a Shirley function was used to define the background. Fe 2p had spin – orbit pairs corresponding to the Fe $2p_{3/2}$ and Fe $2p_{1/2}$. O 1s had two peaks associated with the gas phase water (535.5 eV) and liquid phase water (533.5 eV). The splitting due to the phase is in accordance with literature. Cl 2p had spin – orbit pairs corresponding to Cl $2p_{3/2}$ and $2p_{1/2}$. Br 3d also had spin orbit pairs corresponding to Br $3d_{5/2}$ and $3d_{3/2}$ peaks. All ratios to the O $1s_{liq}$ peak were normalized based on the photoionization cross section, asymmetry parameter and inelastic mean free path (IMFP) of the electron associated with the Fe 2p, Cl 2p and Br 3d orbital. A sample calculation is shown in Appendix I.

All solutions were prepared using aqueous 0.1M H_2SO_4 (Sigma Aldrich, HPLC Grade Water) to generate a solution pH less than the hydrolysis pH of the Fe^{2+} complex ($pH_{hydrolysis} = 3.5$). $FeSO_4 \cdot 7H_2O$ (Sigma Aldrich, ACS Reagent >99.0%) was used to create 0.9M $FeSO_4$ solutions.

0.9M was near the upper solubility limit of the $FeSO_4$ and generated sufficient signal to noise for the Fe 2p peak. NaCl and NaBr (Sigma Aldrich, ACS Reagent) were added to the acidic 0.9M $FeSO_4$ solutions after the solids had fully dissolved. Generating the Fe^{2+} in acidic solution was done to ensure a hexaaquo complex in aqueous solution without any hydrolyzed ligands.

Results

In order to understand the first solvation sphere of Fe^{2+} ions in aqueous solution and prevent any hydrolysis of the aqua ligands that reside in the first solvation sphere, $FeSO_4$ was dissolved in 0.1M H_2SO_4 (aq). The resulting Fe 2p spectrum is shown in Figure 4.1 below.
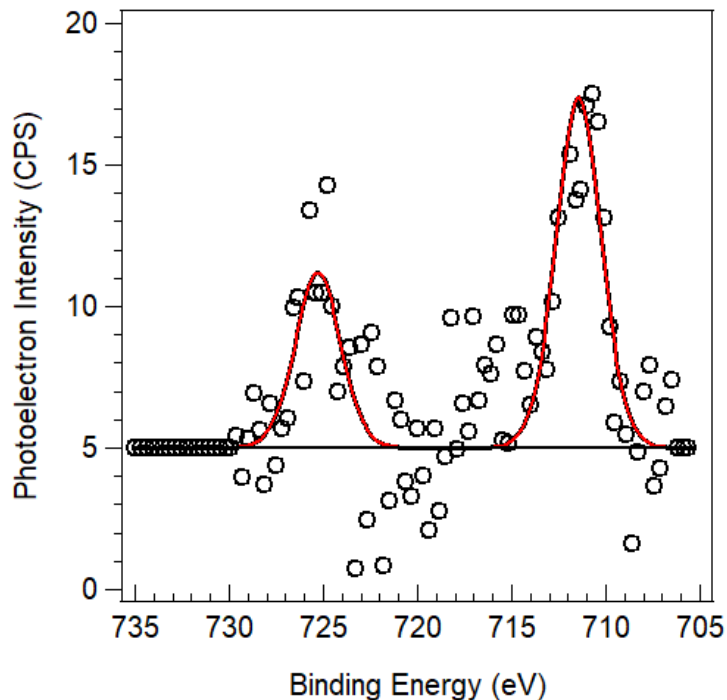
Figure 4.1: Fe 2p of 0.9M FeSO₄ in 0.1M H₂SO₄ aqueous solution. A Shirley background has been subtracted from the raw data for peak clarity.

A single Fe species is shown in the Fe 2p spectral window indicative of a $[Fe(H_2O)_6]^{2+}$ complex. Unfortunately, the species cannot be resolved in the O 1s spectral window due to the large FWHM of the liquid water O 1s. The spin – orbit coupled splitting is 13.8 eV which is similar to those

reported for solid state Fe(II) species.[27] When the Fe 2p area is compared to the O $1s_{liq}$ peak, the ratio for that species is 0.02 and is maintained across all subsequent experiments involving Fe.

To investigate the effect of the halide ions on the Fe complex, NaX salts (X = Cl⁻ and Br⁻) were dissolved in water at increasing concentrations to create a calibration curve. In Figure 4.2, a representative XPS spectrum of O 1s, Cl 2p and Br 3d are shown for 2M solutions.
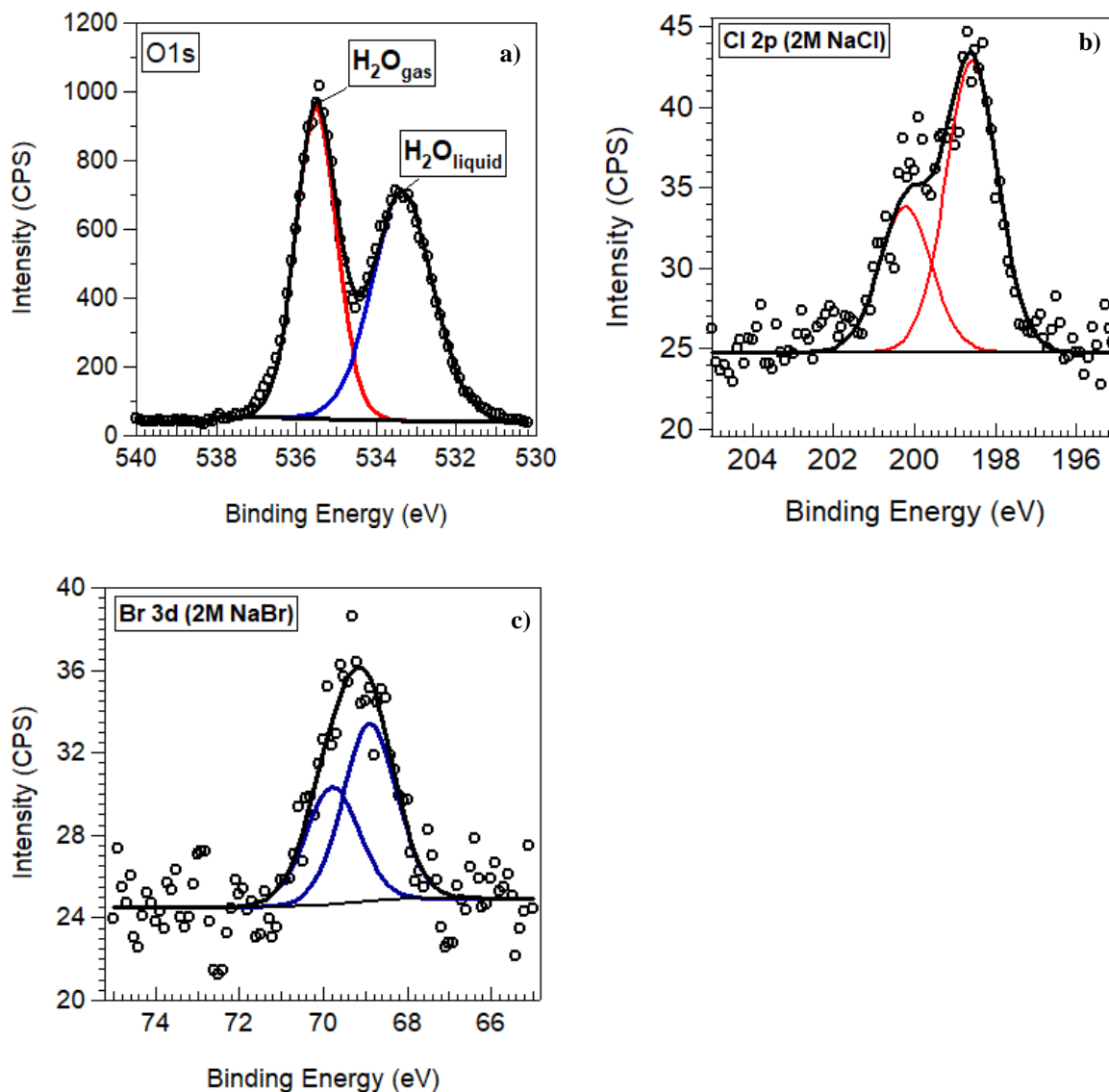
Figure 4.2: *Photoelectron spectra of liquid jet with 2M aqueous solutions of NaCl and NaBr salts. (a) representative O 1s spectrum (b) Cl 2p spectrum of 2M NaCl aqueous solution. (c) Br 3d spectrum from 2M NaBr aqueous solution.*

The splitting of the O1s is similar to what has been reported previously, while the binding energy of the gas and liquid phase are consistent when reported with respect to the Fermi level of the instrument.[28–30] In the Cl 2p spectrum, the binding energy of the $2p_{3/2}$ is 198.7 eV, has a spitting of 1.6 eV and a FWHM of 1.4 eV for the core orbitals. In the Br 3d spectrum, the binding energy is 68.8 eV, has a spitting of 1.0 eV and a FWHM of 1.4 eV. Increasing the concentration of the NaX salts was carried out to indicate whether there are shifts to the binding energy of these peaks as a function of concentration. These peaks were also used to generate a calibration curve as shown in Figure 4.3.
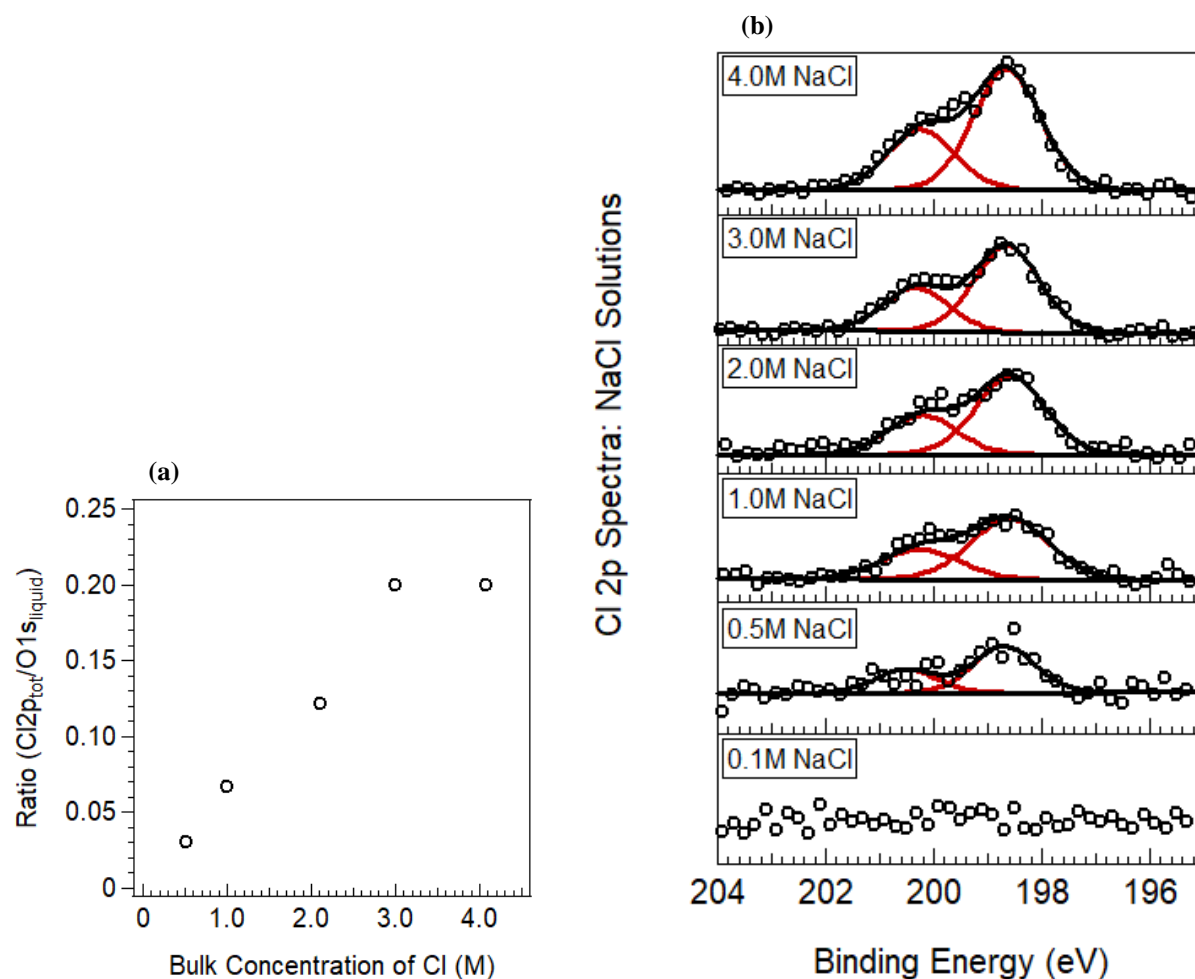
Figure 4.3: Calibration curve using the Cl 2p peaks in increasing concentrations of NaCl aqueous solutions. (a) Cl 2p peaks increasing signal to noise as the concentration is increased. (b) Calibration curve of the ratio of Cl 2p area/O1s$_{liq}$ area as a function of the concentration.

A linear behavior is observed up to a concentration of 3M in Figure 4.3b. After which, the ratio is flattened at 0.20. This effect is likely due to saturation of the interface with Cl^- ions. The binding energy, splitting and FWHM are all found to be consistent with the values reported previously for the 2M concentration and do not deviate outside of the error of the measurement (0.1 eV) as the concentration is increased. A similar curve is generated for NaBr and shows that the values are also consistent with the 2M solution as the concentration is increased. The free Cl^- and Br^- were then used to compare with any changes observed in the solution due to the presence of Fe^{2+}.

Acidic $FeSO_4$ solutions are shown to contain a single Fe species in the Fe 2p region (Figure 4.1). Small shifts were expected when a complexing ion is added to the solution. In Figure 4.4, the Fe 2p of the Fe^{2+} complex and Cl 2p associated with the Cl^- ions in solution is shown as the concentration of NaCl is increased in the solution.
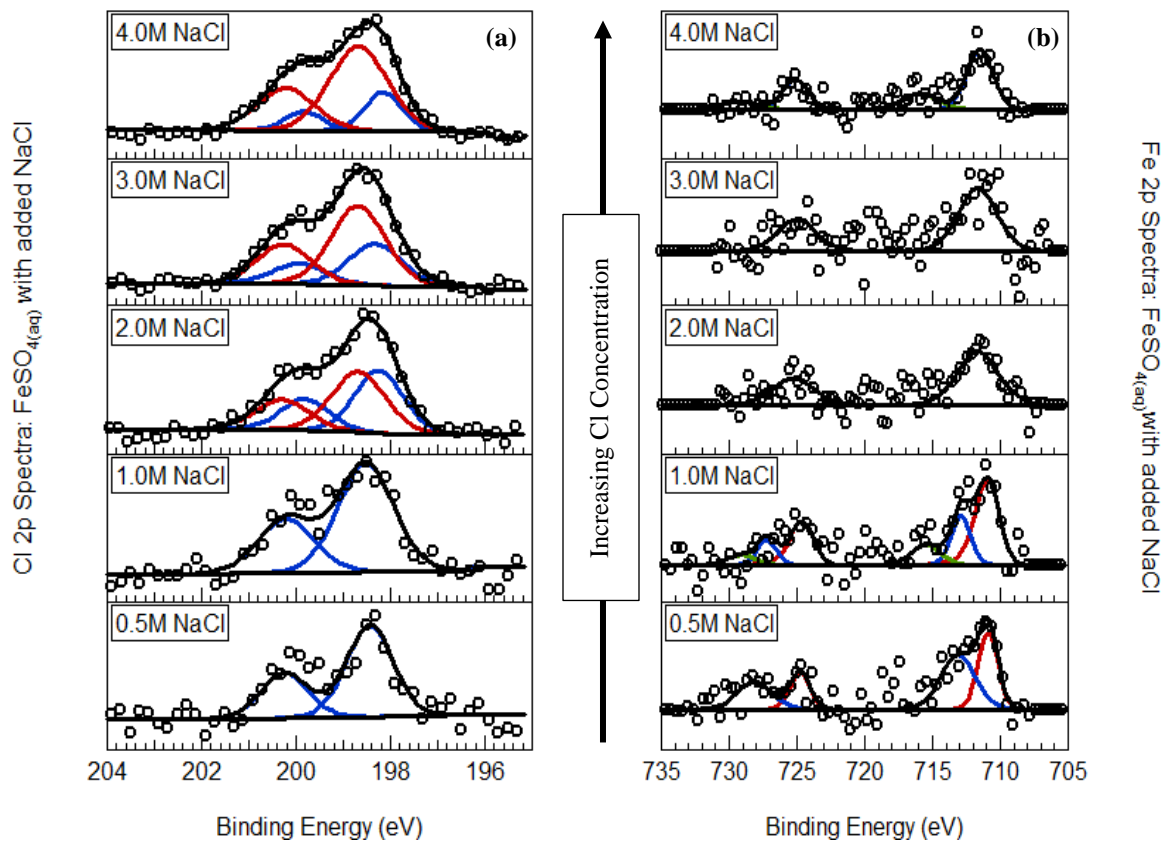
Figure 4.4: *Increasing concentrations of NaCl in 0.9M FeSO₄/0.1M H₂SO₄ solutions. (a) Cl 2p (b) Fe 2p were collected using the same parameters as Figure 1 for Fe 2p and Figure 3 for Cl 2p.*

In the Fe 2p region at low concentrations, a second Fe species is observed at ~713 eV in addition to the 711 eV corresponding to $[Fe(H_2O)_6]^{2+}$. This second contribution is attributed to a free Cl^- ions entering the first solvation sphere of the complex and binding to the Fe^{2+} center to form $[FeCl(H_2O)_5]^+$ near the interface of the solution. The relative ratio of $FeCl^+$ and Fe^{2+} in solution increases until only one species can again be resolved at 713 eV when the ratio of Fe to Cl in solution exceeds 1:1. At higher ratios, if a second Cl^- ion would be added to the inner solvation sphere, a subsequent binding energy shift would be expected, but was not observed. In Figure 4.4a, the related Cl 2p spectra is shown that corresponds to the identity of the Cl^- ion within the solution. A small binding energy shift from 198.7 eV to 198.3 eV is observed. This indicates the

complexation leads to an overall increase of electron density on the Cl ion within the first solvation sphere associated with the shift to lower binding energy. As the concentration is increased beyond a 1:1 ratio of Fe to Cl, a second contribution associated with the free Cl^- ion is observed. The free Cl^- begins to dominate the spectral window as the concentration continues to increase. Similar experiments were performed with Br^- ions; however, no changes were observed in the Fe 2p or Br 3d spectral window.

The calibration curve of the free Cl^- ions can then be overlaid with the calibration curve when there is Fe^{2+} ions present in the solution. The results of which are shown in Figure 4.5.
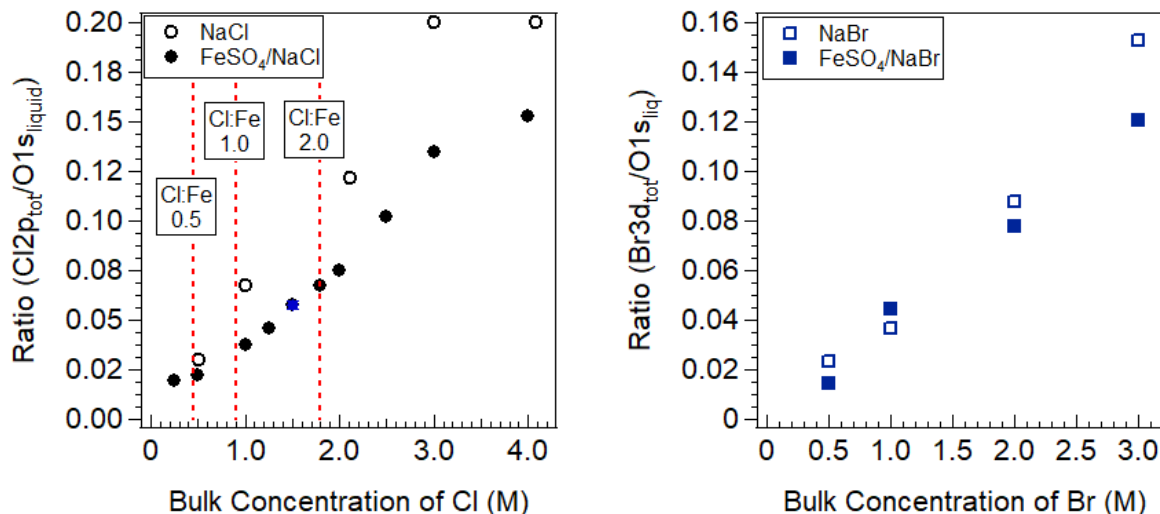
Figure 4.5: Overlay of calibration curve with and without Fe^{2+} present at 0.9M concentration in the solution. (a) Cl 2p have the open points as the solution without Fe^{2+} and the solid points from solution with Fe^{2+} (b) Br 3d have the open points as the solution without Fe^{2+} and the solid points from solution with Fe^{2+}.

In Figure 4.5a, the total concentration of the solution containing Fe(II) ions has a lower Cl 2p: $O1s_{liq}$ ratio compared to the free Cl^- ions in solution. This deviation is small at low concentrations but increases with higher NaCl concentration. At high concentrations, near the saturation turnover for the free Cl^- ions, the ratio does not have the same stark turnover of the ratio and appears to continue increasing. The difference between the two appears to have a constant value in the linear

portion of the curve and does not deviate when higher ratios of Fe:Cl are reached. This is likely due to coordination of the Cl^- ion to the Fe complex in solution. In Figure 4.5b, the same overlaid calibration curves are shown with Br^- ions. The two curves do not show the same deviation until very high concentrations of are reached. This indicates the binding of Br^- ion to Fe complex is weak and does not occur until sufficiently high concentrations force to equilibrium into the complex form.

Based on the data shown in Figure 4.5a, the Fe – Cl complex in solution represents a change in the molecular speciation at the interface of the liquid. In order to investigate this change, experiments were undertaken at the Advanced Light Source (ALS) at the University of California, Berkeley. An Fe^{2+} aqueous solution was created and characterized with respect to depth. A single concentration (0.9M NaCl) representing a 1:1 ratio Fe/Cl was also investigated. The results of the single Fe^{2+} aqueous solution is shown below in Figure 4.6.
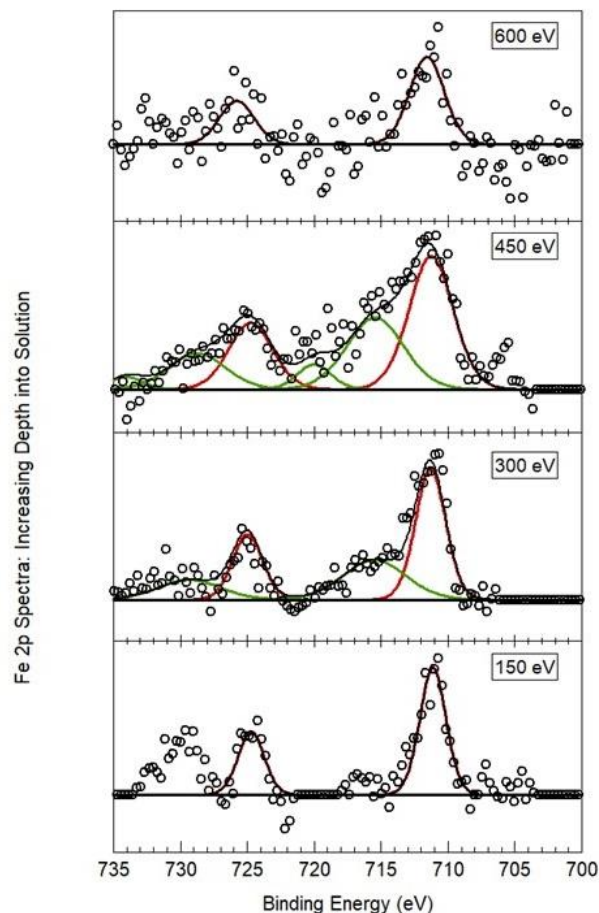
Figure 4.6: Probe depth characterization of 0.9M FeSO₄ aqueous solution. The pH of this solution was 2 and was collected with similar parameters as the lab-based characterization. The energy in each of the panels is the kinetic energy of the photoelectron.

There are two contributions observed as a function of probe depth in the Fe 2p spectra of the Fe^{2+} solution. One occurs at the 711 eV and is indicative of the $[Fe(H_2O)_6]^{2+}$ while the other contribution occurs at a binding energy of 716 eV and is attributed to an Fe^{3+}, $[Fe(H_2O)_6]^+$ complex. The Fe^{3+} species does not occur near the interface of the solution based on its observation only at higher photoelectron kinetic energies.

The addition of an equimolar amount of Cl to the Fe^{2+} solution above generated Figure 4.7 below.

57
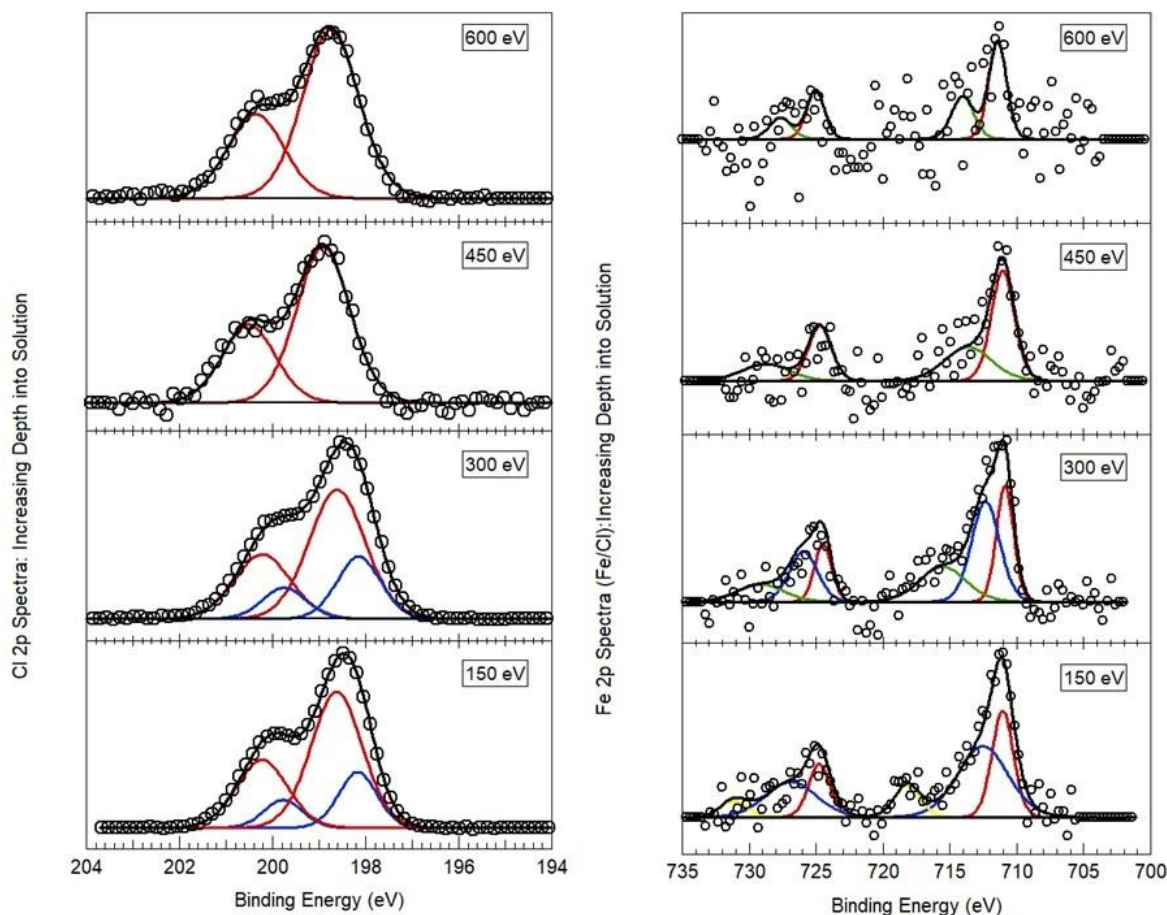
Figure 4.7: *Cl 2p (left) and Fe 2p (right) of 0.9M FeSO$_4$ acidic aqueous solution. The pH of this solution is 2 as in previous experiments. The photoelectron kinetic energies are shown in the inset boxes in each frame.*

The addition of Cl to the Fe^{2+} aqueous solution generates a very different spectral signal compared with the Cl free Fe^{2+} solution. A second contribution to the Fe 2p spectra appears at 712 eV binding energy at low probe depth and indicates the coordination of the Cl to the Fe^{2+} inner solvation sphere. This signal does not occur at higher probe depths, indicating this species occurs near the interface of the solution. The Cl 2p also shows two contributions in the spectral window. One that occurs at the 198.3 eV and another at the 198.7 eV, which has been assigned to a coordinated Cl and a free Cl$^-$ respectively. The coordinated species at 198.3 eV only exists at the low probe depths in the Cl 2p spectra and is not resolved above the background above 450 eV photoelectron kinetic

energy. This further supports the notion that the coordinated $[FeCl(H_2O)_5]^+$ occurs near the interface rather than in the bulk of the solution.

Discussion

Speciation of Fe^{2+} at the Air – Liquid Interface

In $FeSO_4$ aqueous solutions, we have shown that only one complex is present at the interface indicated by the binding energy of 711 eV in the Fe 2p spectrum in Figure 4.1. We have assigned this to a $[Fe(H_2O)_6]^{2+}$ complex as the acidic solution would prevent the hydrolysis of the aqua ligands attached to the Fe^{2+} in aqueous solution. This complex can only be resolved at concentrations approaching the solubility limit of $FeSO_4$ in aqueous solutions and indicates that the complex does not have a propensity for the interface like other species. This is not unprecedented, as large highly charged polyatomic ions such as sulfate have been shown to prefer bulk solvation rather than a surface solvation.[31,32] In addition, we have shown that the overall speciation of Fe^{2+} changes at deeper probe depths in Figure 4.6. It should be noted that the pH of the depth profile work is set at pH 2 (0.01M H_2SO_4), which allows for a higher concentration of Fe^{2+} complexes with hydrolyzed ligands and oxidation of the Fe^{2+} to Fe^{3+}. The major species at the interface is the $[Fe(H_2O)_6]^{2+}$ complex by the single contribution to the Fe 2p species at 150 eV excitation energy with a binding energy at 711 eV. A second species is observed at 300 and 450 eV, a much higher binding energy that we are attributing to an Fe^{3+} complex. The binding energy of this species is ∼ 5 eV higher in binding energy and is attributed to an oxidation state change rather than a change to the first solvation shell of the Fe^{2+} center. Smaller binding energy shifts are more likely to be a first solvation shell effect rather than a large shift such as this. Control of the pH was also crucial in these experiments as the Fe^{2+} spectra in the 0.1M H_2SO_4 solution of Figure

4.1 show no contribution above the background at the higher binding energy and therefore no oxidation of the Fe^{2+} in solution.

Addition of Halide Anions to Fe^{2+} Aqueous Solutions

Given that $[Fe(H_2O)_6]^{2+}$ comprises the majority of the Fe species at the interface, the addition of small anions could affect the first solvation sphere, altering the distribution of the Fe speciation away from the air – water interface. The addition of Cl^- and Br^- ions to the solution illustrates the difference between two ions that are instrumental in many atmospheric reactions. In Figure 4.4, there is a new contribution to the Fe 2p spectra that is higher in binding energy compared to the contribution from $[Fe(H_2O)_6]^{2+}$ by 2 eV. This new peak has been assigned to a single Cl^- ion that has coordinated to the Fe^{2+} in the first solvation shell. This contribution increases as the amount of Cl increases until a single contribution is observed at the new binding energy of 712 eV. The signal at 712 eV could indicate dimerization of the Fe complexes near the interface at higher concentrations, however more work is required to determine the exact identity of the species shown in the Fe 2p region at high Cl concentrations. The distribution of the species at 1M NaCl, or a 1:1 ratio of Cl to Fe, is shown in Figure 4.7. Again, the contribution of 713 and 711 eV are both present at the interface (150 eV excitation energy). As the probe depth is increased, there is a change in the distribution of species deeper into the solution. The $[FeCl(H_2O)_5]^+$ is not observed beyond 300 eV excitation energy and the iron – aquo contribution is present at all excitation energies. This indicates that the Fe – Cl species resides near the air – water interface rather than in bulk solvation like the Fe aquo species.

The Cl 2p region also offers a glimpse into the changes observed with the Cl^- ion in the solution. In Figure 4.4, the Cl is dominated by the contribution at 198.3 eV at low NaCl concentrations, indicating that the Cl^- ion is coordinated to the Fe center. As the concentration is

increased, there is discernable asymmetry in the peaks and the contribution from 198.7 eV begins to increase after a 1:1 ratio of Cl to Fe. The free Cl^- ion contribution begins to dominate the spectra after 2M NaCl is added to the Fe solution. In Figure 4.7, the Cl 2p region as a function of probe depth is shown and corroborates what is observed in the Fe 2p spectra. The 198.3 eV Fe – Cl contribution occurs near the interface, whereas the bulk solution contains the free Cl^- ion and no complexation appears at a ratio of 1:1 Fe to Cl. The difference between the lab – based Cl spectra and the synchrotron spectra could be due to the pH of the solution or to the brilliance of the synchrotron radiation that allows for more of the free Cl^- to be observed in the Cl 2p region.

The different species have been defined based on the data presented. It is clear that the complexed $[FeCl(H_2O)_5]^+$ resides near the air – water interface and the $[Fe(H_2O)_6]^{2+}$ prefers bulk solvation rather than the interface. Figure 4.5 shows how the complexation can change the standard curve and provides some insight into the fate of the small anion once it is coordinated to the Fe species. Depletion of Cl^- ions near the interface by complexation to the Fe complex gives rise to a decrease in the Cl 2p: $O1s_{liq}$ ratio as a function of concentration. This is in comparison to the Br^- ions, which do not bind as readily to the Fe^{2+} complex, which show no change in the ratio of Br 3d:O $1s_{liq}$ whether there is Fe complexes in the solution or not. It should be noted that Br does coordinate the Fe^{2+}, but with a coordination constant that is significantly lower than for Cl. All solutions in this work were prepared fresh and characterized immediately, mitigating slow coordination events on the time scale of the analysis.

Consequences to Fenton Chemistry at Air – Water Interface

Fenton chemistry in the atmosphere has been proposed to occur at the air – water interface. Based on the results from this study, it is unlikely that the chemistry will happen directly at the interface and is more likely to occur near the bulk of the solution. Fenton chemistry is driven by the outer

sphere electron transfer of Fe^{2+} center to peroxide to form a hydroxyl radical and hydroxide, making the solution more basic. Regeneration of the Fe^{2+} species must also occur for the catalysis to continue. In bulk studies, there has been suppression of the Fenton chemistry when Cl^- ions are present, but not when Br^- ions are present in the solution. Given the species shown in Figure 4.4 and Figure 4.7, Cl^- ions bind to the Fe center presumably making it more difficult for the Fe to transfer an electron via an inner sphere mechanism to a peroxide in the solution. Furthermore, the complexed Fe – Cl species also resides at the interface alongside the Fe – aqua and would therefore slow the Fenton reaction there. With Br^- ions present, there is no apparent coordination and the electron transfer would occur unimpeded as it would without the Br^- ions present in the solution. Concentrations of $FeSO_4$ approaching the solubility limit were required to generate a suitable signal to noise to investigate these solutions with liquid jet XPS. This supports the hypothesis that the Fe^{2+} prefers bulk solvation as if it were to prefer interfacial solvation, a much lower concentration could be used to characterize the solutions.

Figure 4.5 sheds light on an unintended consequence of the complexation events with Fe species or any other transition metal complex that has that bind additional ligands. In addition to the Cl^- ion coordinating to the Fe complex in solution, there is also a depletion of the Cl^- ions away from the air – water interface. In normal aqueous solutions, Cl^- ions have a propensity for the interface and has been linked to many fundamental reactions that occur there.[33–36] These reactions would be modified or depleted entirely if the Cl^- ions are no longer at the interface. They would also be subject to the concentration of the Fe^{2+} species in the solution and should be taken into consideration as a possible cause of abnormalities in the reaction rates.

Conclusions

The work described here shows the speciation of different Fe^{2+} complexes away from the air – water interface and the effect of small anions that are present in the solution. $[Fe(H_2O)_6]^{2+}$ at 711 eV was found to prefer bulk solvation by synchrotron characterization and by the high concentrations of $FeSO_4$ required to carry out the experiment. Free Cl^- ions were found at 198.7 eV in aqueous solutions. When Cl^- ions are added to the solution, complexation occurs and generates a new peak in both the Fe 2p (713 eV) and Cl 2p (198.3 eV) that is dependent on the concentration of the Cl in solution. This is in stark contrast to Br^- ions which show no complexation and no change in either the Br or Fe spectra. The complexation event also depletes the interface of Cl ions that would normally be used for interfacial oxidation reactions. From this work, it is unlikely that Fenton chemistry occurs at the interface, but is a bulk reaction and interfacial oxidation reactions depending on Cl^- ions would also be affected by the presence of Fe complexes in the solution.

References

1   H. A. Al-Abadleh, Review of the bulk and surface chemistry of iron in atmospherically relevant systems containing humic-like substances, *RSC Adv.*, 2015, **5**, 45785–45811.

2   H. Schugar, C. Walling, R. B. Jones and H. B. Gray, The Structure of Iron (III) in Aqueous Solution, *J. Am. Chem. Soc.*, 1967, **89**, 3712–3720.

3   J. Burgess and M. V Twigg, in *Encyclopedia of Inorganic and Bioinorganic Chemistry*, 2011.

4   A. Fischbacher, C. von Sonntag and T. C. Schmidt, Hydroxyl radical yields in the Fenton process under various pH, ligand concentrations and hydrogen peroxide/Fe(II) ratios, *Chemosphere*, 2017, **182**, 738–744.

5   M. Oakes, R. J. Weber, B. Lai, A. Russell and E. D. Ingall, Characterization of iron speciation in urban and rural single particles using XANES spectroscopy and micro X-ray fluorescence measurements: Investigating the relationship between speciation and fractional iron solubility, *Atmos. Chem. Phys.*, 2012, **12**, 745–756.

6   M. J. Apted, G. A. Waychunas and G. E. Brown, Structure and specification of iron complexes in aqueous solutions determined by X-ray absorption spectroscopy, *Geochim. Cosmochim. Acta*, 1985, **49**, 2081–2089.

7   G. J. Herdman and G. W. Neilson, Ferrous Fe(II) hydration in a 1 molal heavy water solution of iron chloride, *J. Phys. Condenced Matter*, 1992, **4**, 649–653.

8   H. Ohtaki, T. Yamaguchi and M. Maeda, 1976, 701–708.

9   E. Miliordos and S. S. Xantheas, Ground and excited states of the [Fe(H2O)6]2+ and [Fe(H2O)6]3+ clusters: Insight into the electronic structure of the [Fe(H2O)6]2+-[Fe(H2O)6]3+ complex, *J. Chem. Theory Comput.*, 2015, **11**, 1549–1563.

10   H. Taube, Rates and mechanisms of substitution in inorganic complexes in solution, *Chem. Rev.*, 1952, **50**, 69–126.

11   B. H. Irving and R. J. P. Williams, Stability of Transition - Metal Complexes, , DOI:10.1039/JR9530003192.

12   T. Remsungnen and B. M. Rode, QM/MM molecular dynamics simulation of the structure of hydrated Fe(II) and Fe(III) ions, *J. Phys. Chem. A*, 2003, **107**, 2324–2328.

13   E. Kálmán, T. Radnai, G. Pálinkás, F. Hajdu and A. Vértes, Hydration of iron(II) ion in aqueous solutions, *Electrochim. Acta*, 1988, **33**, 1223–1228.

14   E. Guardia and J. A. Padro, Molecular-Dynamics Simulation of Ferrous and Ferric Ions in Water, *Chem. Phys.*, 1990, **144**, 353–362.

15   G. J. Herdman and G. W. Neilson, Ferric ion (Fe (III)) coordination in concentrated aqueous electrolyte solutions, *J. Phys. Condenced Matter*, 1992, **4**, 627–638.

16   S. Amira, D. Spångberg, M. Probst and K. Hermansson, Molecular Dynamics Simulation of Fe $^{2+}$ (aq) and Fe $^{3+}$ (aq), *J. Phys. Chem. B*, 2004, **108**, 496–502.

17   R. Seidel, K. Kraffert, A. Kabelitz, M. N. Pohl, R. Kraehnert, F. Emmerling and B. Winter, Detection of the electronic structure of iron-(<scp>iii)</scp> -oxo oligomers forming in aqueous solutions, *Phys. Chem. Chem. Phys.*, , DOI:10.1039/C7CP06945F.

18   N. Ottosson, M. Faubel, S. E. Bradforth, P. Jungwirth and B. Winter, Photoelectron spectroscopy of liquid water and aqueous solution: Electron effective attenuation lengths and emission-angle anisotropy, *J. Electron Spectros. Relat. Phenomena*, 2010, **177**, 60–70.

19   P. Jungwirth and D. J. Tobias, Ions at the air/water interface, *J. Phys. Chem. B*, 2002, **106**, 6361–6373.

20   S. Gopalakrishnan, P. Jungwirth, D. J. Tobias and H. C. Allen, Air-liquid interfaces of

aqueous solutions containing ammonium and sulfate: Spectroscopic and molecular

dynamics studies, *J. Phys. Chem. B*, 2005, **109**, 8861–8872.

21   M. A. Brown, R. D'Auria, I. F. W. Kuo, M. J. Krisch, D. E. Starr, H. Bluhm, D. J. Tobias

and J. C. Hemminger, Ion Spacial Distributions at the Liquid - Vapor Interface of

Aqueous Potassium Fluoride Solutions, *Phys. Chem. Chem. Phys.*, 2008, **10**, 4676–4677.

22   D. J. Tobias and J. C. Hemminger, Chemistry - Getting specific about specific ion effects,

Science (80-.)., 2008, **319**, 1197–1198.

23   S. Enami, Y. Sakamoto and A. J. Colussi, Fenton chemistry at aqueous interfaces, *Proc.

Natl. Acad. Sci.*, 2014, **111**, 623–628.

24   K. A. Perrine, K. M. Parry, A. C. Stern, M. H. C. Van Spyk, M. J. Makowski, J. A.

Freites, B. Winter, D. J. Tobias and J. C. Hemminger, Specific cation effects at aqueous

solution−vapor interfaces: Surfactant-like behavior of Li + revealed by experiments and

simulations, *Proc. Natl. Acad. Sci.*, 2017, 201707540.

25   A. M. Margarella, K. A. Perrine, T. Lewis, M. Faubel, B. Winter and J. C. Hemminger,

Dissociation of sulfuric acid in aqueous solution: Determination of the photoelectron

spectral fingerprints of H2SO4, HSO 4-, and SO42- in water, *J. Phys. Chem. C*, 2013,

117, 8131–8137.

26   M. A. Brown, B. Winter, M. Faubel and J. C. Hemminger, Spatial Distribution of Nitrate

and Nitrite Anions at the Liquid/Vapor Interface of Aqueous Solutions, *J. Am. Chem.

Soc.*, 2009, **131**, 8354–+.

27   A. P. Grosvenor, B. A. Kobe, M. C. Biesinger and N. S. McIntyre, Investigation of

multiplet splitting of Fe 2p XPS spectra and bonding in iron compounds, *Surf. Interface*

Anal., 2004, **36**, 1564–1574.

28   B. Winter and M. Faubel, Photoemission from Liquid Aqueous Solutions, *Chem. Rev.*, 2006, **106**, 1176–1211.

29   R. Seidel, S. Thürmer and B. Winter, Photoelectron spectroscopy meets aqueous solution: Studies from a vacuum liquid microjet, *J. Phys. Chem. Lett.*, 2011, **2**, 633–641.

30   M. A. Brown, R. D'Auria, I. F. W. Kuo, M. J. Krisch, D. E. Starr, H. Bluhm, D. J. Tobias and J. C. Hemminger, Ion spatial distributions at the liquid-vapor interface of aqueous potassium fluoride solutions, *Phys. Chem. Chem. Phys.*, 2008, **10**, 4778–4784.

31   W. Hua, D. Verreault and H. C. Allen, Relative Order of Sulfuric Acid, Bisulfate, Hydronium, and Cations at the Air-Water Interface, *J. Am. Chem. Soc.*, 2015, **137**, 13920–13926.

32   A. M. Jubb and H. C. Allen, Bisulfate dehydration at air/solution interfaces probed by vibrational sum frequency generation spectroscopy, *J. Phys. Chem. C*, 2012, **116**, 13161–13168.

33   B. J. Finlayson-Pitts, Reactions at surfaces in the atmosphere: integration of experiments and theory as necessary (but not necessarily sufficient) for predicting the physical chemistry of aerosols, *Phys. Chem. Chem. Phys.*, 2009, **188**, 7760–7779.

34   A. L. Sumner, E. J. Menke, Y. Dubowski, J. T. Newberg, R. M. Penner, J. C. Hemminger, L. M. Wingen and B. J. Finlayson-pitts, implications for heterogeneous chemistry in the troposphere.

35   C. W. Spicer, R. A. Plastridge, K. L. Foster, B. J. Finlayson-Pitts, J. W. Bottenheim, A. M. Grannas and P. B. Shepson, Molecular halogens before and during ozone depletion events in the Arctic at polar sunrise: Concentrations and sources, *Atmos. Environ.*, 2002,

36, 2721–2731.

36   B. J. Finlayson-Pitts and J. C. Hemminger, Physical Chemistry of Airborne Sea Salt

Particles and Their Components, *J. Phys. Chem. A*, 2000, **104**, 11463–11477.

Chapter 5: Exploring the Electronic Structure of Acetic Acid and its Solvation Using Liquid Jet X – ray Photoelectron Spectroscopy

Introduction

Acetic acid is a very important molecule in industrial and biological processes, and atmospheric reactions.[1–3] It is one of the simplest carboxylic acids having several points for interaction with a solvent through hydrogen bonding. In the gas phase, the accepted structure is a cyclic dimer shown by molecular dynamics (MD) simulations and diffraction experiments.[4] Acetic acid in the liquid phase presents a different challenge regarding the solvation and hydrogen bonding network associated with the molecule in solution from both an experimental and theoretical point of view.

Characterization of any small organic molecules in solution often relies on vibrational spectroscopy to extract information associated with any change in solvation.[5,6] MD simulations can offer some insight but require high quality structural information from diffraction studies, in addition to the vibrational work, that are difficult to obtain in solution. A different point of view to assist the MD simulations would be to focus on the intramolecular changes to the electronic structure of the molecule and follow the changes in solvation based on perturbations to the molecular electronic structure. UV – vis spectroscopy is one technique that could be used in to achieve this goal; however, this relies on low lying virtual orbitals present in double bonds that may not always be present in a given system. The data often suffers from low resolution of peaks which makes interpretation difficult and reliant on other techniques mentioned previously.[7]

Of the few techniques that can be used to investigate the electronic structure of a molecule, X – ray photoelectron spectroscopy (XPS) is the most valuable. Recent advances in instrumentation, including electron transfer lenses and differential pumping, have enabled characterization of liquid

interfaces using liquid jet ambient pressure XPS (LJ-XPS).[8–10] XPS is sensitive to changes in the local chemical environment of aqueous solutions, such as changes in pH,[11,12] and could be used to understand the solvation of a molecule such as acetic acid by investigating the changes in the relative chemical environments between the carbonyl and methyl carbons in the molecule. In aqueous solution, this would provide additional understanding of the solvation of acetic acid to the present literature and can also be used to investigate changes in solvation when different solvents are used. Methanol is a common solvent used in the work here to analyze the role solvent plays on the solvation of acetic acid.

In conjunction with the LJ – XPS measurements, molecular dynamics (MD) and core orbital simulations were used to further interpret the changes of the intramolecular electronic structure based on changes in solvation. These simulations are critical to understanding how the hydrogen bonding network of methanol interacts with the acetic acid in comparison to water in aqueous solutions.

Experimental

Solutions were prepared at a 5M bulk concentration using either water or methanol. A small amount of NaCl (0.02M) was added to the solutions to prevent charging of the liquid jet. Acetic acid, sodium acetate, trifluoroacetic acid and d^4 – acetic acid (Sigma Aldrich, ACS Reagent) were all used as received without any purification. The solutions were then characterized immediately after mixing with no modifications in pH. Gas phase spectra are obtained with the liquid jet positioned away from the entrance to the electron analyzer, ensuring no liquid phase peaks appear. Liquid phase spectra are collected with the liquid jet near the analyzer cone and contain both gas and liquid phase spectra. The liquid jet is operated at a flow rate of 0.4 mL/min.

All liquid jet XPS spectra were collected at 50 eV pass energy and were calibrated to the O 1s gas phase of water at 535.5 eV. All spectra are reported as a difference in binding energy between the carbonyl and methyl carbon (ΔBE) to account for any small charging effects that may shift the peaks and modify the absolute binding energy. The energy resolution of the analyzer at this pass energy is 1.0 eV. High resolution spectra of the different core orbitals of acetic acid were collected as follows:

Table 5.1: Core – Orbital collection parameters of the acetic acid liquid jet spectra

Core Orbital	Step Size (eV)	Number of Passes
C 1s	0.2	10
O 1s	0.2	3

Results

Gas Phase of Acetic Acid Derivatives in Aqueous Solutions

The electronic structure of acetic acid and its derivatives were investigated in aqueous and alcohol solutions. Our experimental observations of the perturbation in the electronic structure can provide insight into the solvation of acetic acid in these different solvents. In order to accomplish this, an understanding of the electronic structure in vacuum is essential. Figure 5.1 shows the C 1s gas phase spectra of the different acetic acid derivatives in aqueous solution.

The binding energy of the carbonyl C 1s for hydrogen and deuterium terminated moieties are 291.00 and 290.92 eV respectively. In contrast, the C 1s binding energy of the fluorinated molecule
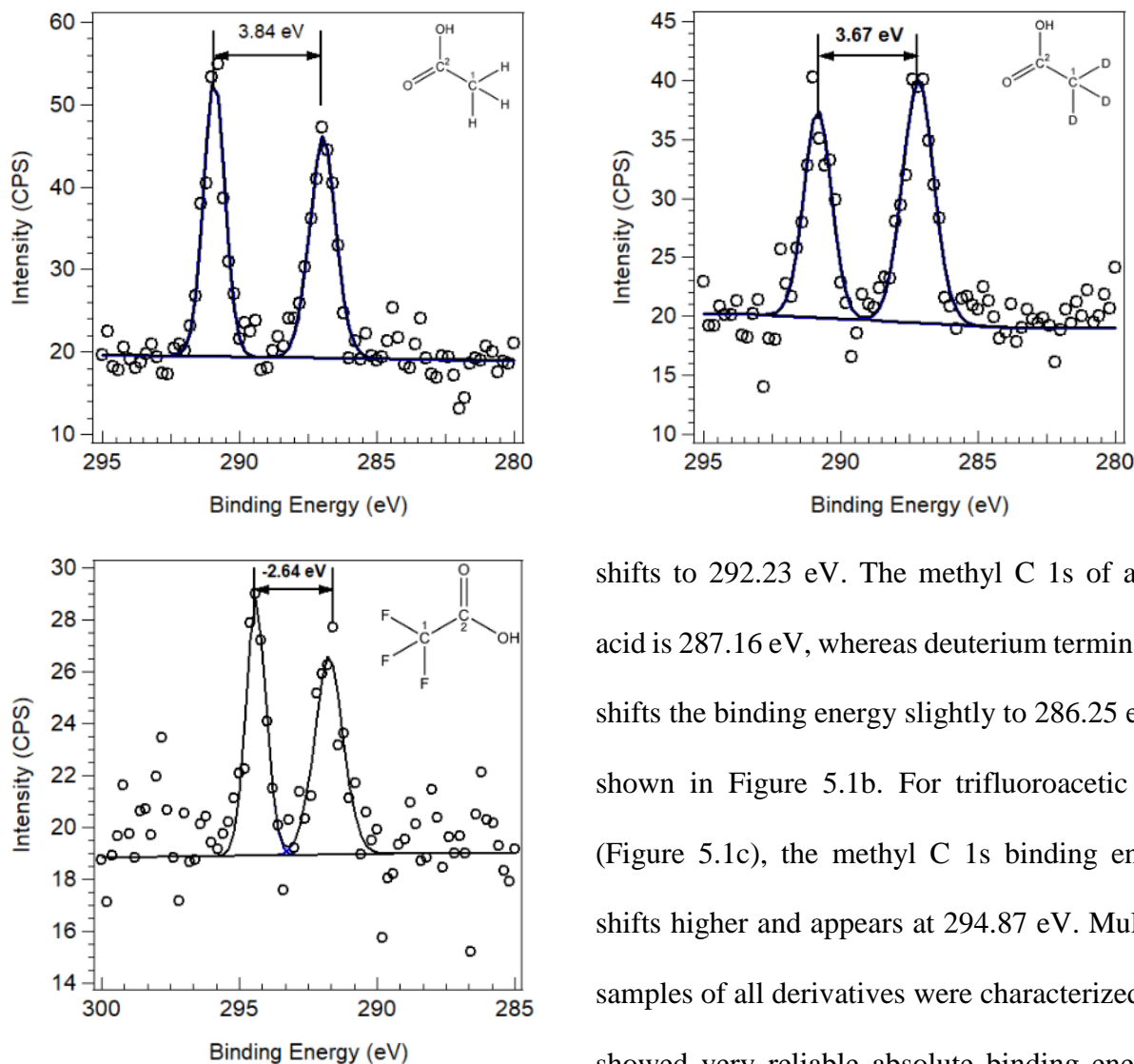
Figure 5.1: *C 1s spectra of gas phase (a) acetic acid (b) d⁴ acetic acid and (c) trifluoroacetic acid in aqueous solution at 5M concentration*

shifts to 292.23 eV. The methyl C 1s of acetic acid is 287.16 eV, whereas deuterium termination shifts the binding energy slightly to 286.25 eV as shown in Figure 5.1b. For trifluoroacetic acid (Figure 5.1c), the methyl C 1s binding energy shifts higher and appears at 294.87 eV. Multiple samples of all derivatives were characterized and showed very reliable absolute binding energies within 0.05 eV. The difference between the two peaks in the C 1s spectrum (ΔBE) can be used to show any change based on the solvation of the molecule in solution. ΔBE circumvents the reliance on absolute binding energy, which can be affected by small solution changes such as minor charging of the liquid jet surface. The termination of deuterium to the methyl carbon of acetic acid shows a decrease of 0.17 eV in ΔBE. Although this is lower than the step size of the experiment, this shift is still considered significant based on multiple experimental runs giving the same result. In addition, a Monte Carlo simulation of the peak model was used to estimate the errors in the peak

position and full width half max (FWHM).[13] These values are given in Table 5.2. A ΔBE of -2.64 eV is shown for trifluoroacetic acid in Figure 5.1c. The negative value is attributed to the strong electron withdrawing fluorine atoms attached to the methyl carbon, causing a large shift to higher binding energy. The O 1s peak was also collected for these experiments. However, the large signal from the water in the gas phase and the broadness of the desired signal prevented any information being gathered from this O 1s spectra. The relative ratios of the carbonyl and methyl for both the deuterated acetic acid and acetic acid are 1.13 and 1.28 in the gas phase. In trifluoroacetic acid, the ratio decreases to 0.88. These are all very close to the 1:1 value expected for the acetic acid moiety. A summary of all the relevant gas phase peaks is shown below in Table 5.2.

Table 5.2: *Summary of C 1s gas phase peaks of aqueous acetic acid derivatives. ΔE is the difference in binding energy between the methyl and carbonyl carbons in electron volts. Errors were calculated from a Monte Carlo simulation of the peak fit against the raw data.*

	Carbonyl Carbon		Methyl Carbon		ΔBE (eV)	Area Ratio (methyl:carbonyl)
	E_b (eV)	FWHM (eV)	E_b (eV)	FWHM (eV)		
Acetic Acid	291.00 $\pm$ 0.03	0.85 $\pm$ 0.10	287.16 $\pm$ 0.05	1.22 $\pm$ 0.15	3.84 $\pm$ 0.06	1.13
d^4 – Acetic acid	290.92 $\pm$ 0.06	1.07 $\pm$ 0.22	287.25 $\pm$ 0.05	1.17 $\pm$ 0.19	3.67 $\pm$ 0.08	1.28
Trifluoroacetic acid	292.23 $\pm$ 0.08	1.21 $\pm$ 0.30	294.87 $\pm$ 0.06	0.84 $\pm$ 0.20	-2.64 $\pm$ 0.10	0.88

Liquid Phase of Acetic Acid Derivatives in Aqueous Solutions
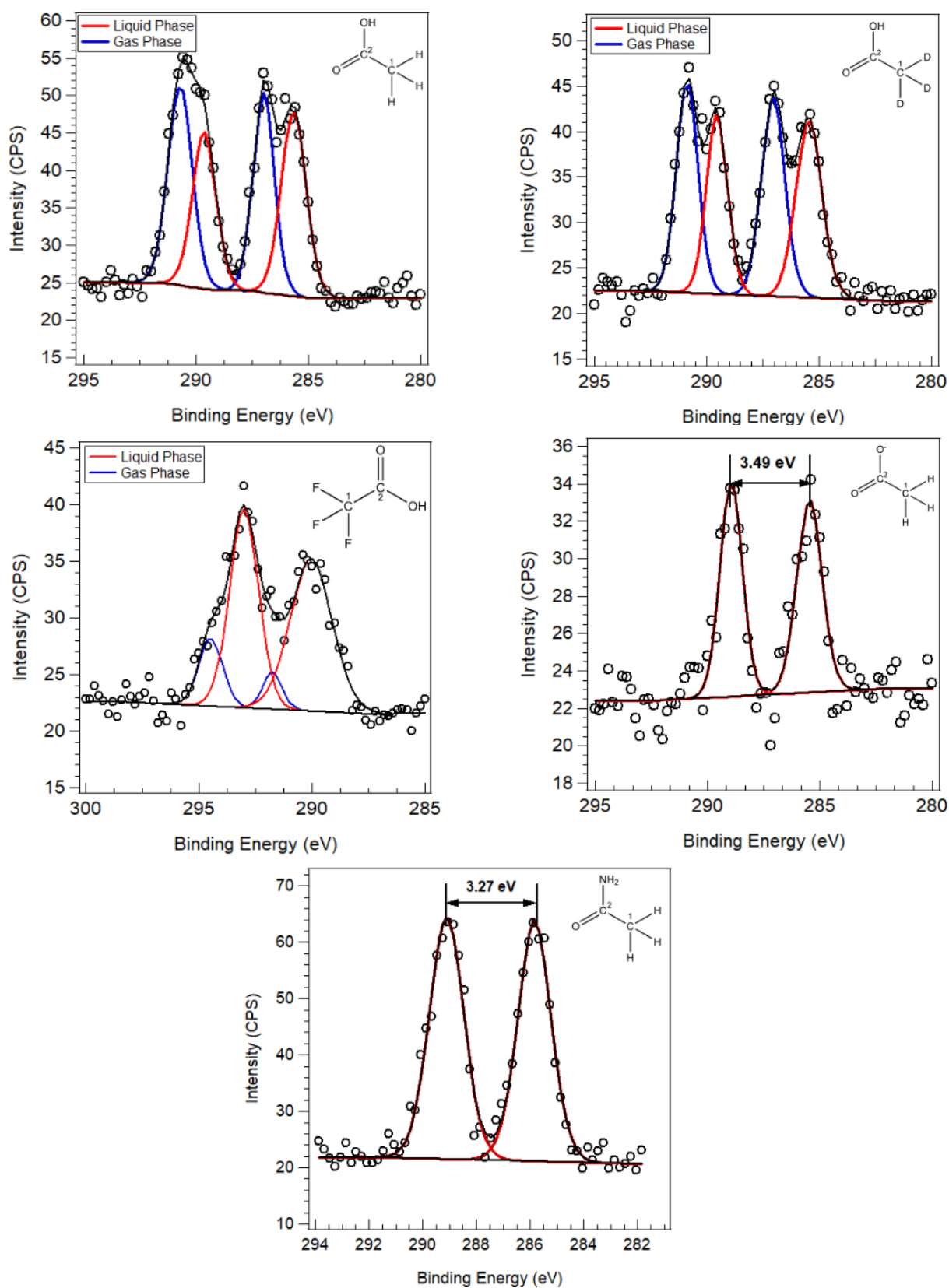
Figure 5.2: *C 1s spectra of liquid and gas phase (a) acetic acid (b) d⁴ – acetic acid (c) trifluoroacetic acid (d) sodium acetate and (e) acetamide in aqueous solutions. All concentrations are at 5M.*

Liquid phase peaks of the different acetic acid aqueous solutions were also characterized. The C 1s spectra for each of those aqueous solutions are shown in Figure 5.2. It should be noted that in the liquid jet characterization both the liquid and gas phase of the substituted acetic acid moieties are observed in the spectra. For the various acetic acid derivatives, the liquid phase peak is shifted to a lower binding energy with respect to the gas phase peaks, consistent with previous liquid jet work.[14–16] In Figure 5.2a, the aqueous phase carbonyl carbon is shifted to 289.66 eV, whereas the methyl carbon is at 285.64 eV. For deuterated acetic acid in Figure 5.2b, the liquid phase carbonyl carbon is at 289.71 eV and the methyl carbon is at 285.60 eV. Finally, for trifluoroacetic acid in Figure 5.2c the liquid phase carbonyl carbon is at 290.71 eV, while the methyl carbon is at 293.68 eV. The carbonyl C 1s peak of sodium acetate appears at 288.95 eV, whereas the methyl peak appears at 285.46 eV. Acetamide has its carbonyl peak at 289.11 eV, while its methyl peak appears at 285.84 eV. The gas phase peaks in each of the spectra in Figure 5.2 shift a small amount compared to the gas phase only peaks in Figure 5.1. This could be due to charging at the jet surface, or due to the fitting and highlights the use of ΔBE to compare the different moieties across different conditions. ΔBE of the liquid phase peaks of acetic acid and deuterated acetic acid were found to be 4.02 and 4.11 eV respectively whereas the difference for the trifluoroacetic acid were found to be -2.97 eV. ΔBE for the acetate ion was found to be 3.49 eV and acetamide was 3.27 eV. All ΔBE's are summarized in Table 5.3 for each of the acetic acid derivatives.

In Figure 5.2b, the ratio between methyl and carbonyl areas is consistent across all species as 1:1. Small deviations from this ratio are observed, however they are consistent with the gas phase only spectra. A difference in the gas to liquid phase ratio of the trifluoroacetic acid C 1s areas is observed. The lower vapor pressure of the trifluoroacetic acid may prevent the molecule from

75

evaporating into the gas phase above the jet. There is also a discernable increase in the FWHM of the carbonyl peak of the liquid phase trifluoroacetic acid compared to the gas phase.

Acetamide and acetate show no gas phase contributions and remain in solution. This is consistent with the two existing in solid form prior to mixing into aqueous solutions.

Table 5.3: Summary of C 1s liquid phase data of different acetic acid derivatives. ΔE values are the difference between the methyl and carbonyl binding energies in electron volts.

	Carbonyl Carbon		Methyl Carbon		ΔE_{gas} (eV)	ΔE_{liq} (eV)
	E_b (eV)	FWHM (eV)	E_b (eV)	FWHM (eV)		
Acetic Acid	289.66 ± 0.09	1.10 ± 0.15	285.64 ± 0.07	1.07 ± 0.16	3.90 ± 0.11	4.02 ± 0.11
d^4 – Acetic acid	289.71 ± 0.06	1.10 ± 0.11	285.60 ± 0.05	1.35 ± 0.14	3.84 ± 0.06	4.11 ± 0.08
Trifluoro acetic acid	290.71 ± 0.08	2.20 ± 0.16	293.68 ± 0.08	1.50 ± 0.34	-2.73 ± 0.24	-2.97 ± 0.11
Sodium Acetate	288.95 ± 0.04	1.16 ± 0.10	285.46 ± 0.05	1.31 ± 0.12	-	3.49 ± 0.06
Acetamide	289.11 ± 0.02	1.49 ± 0.08	285.84 ± 0.03	1.45 ± 0.08	-	3.27 ± 0.04

Acetic Acid in Methanol

In the previous section, the spectra of aqueous solutions of acetic acid, d^4 – acetic acid, trifluoroacetic acid, sodium acetate and acetamide were presented. Below, data for the corresponding methanol solutions is presented. By studying the changes in ΔBE between aqueous and methanol solutions we will learn how the solvation will impact the electronic structure of the solutes. The solvent itself needs to be investigated prior to any solute addition. Figure 5.3 below shows the C 1s spectra of methanol in the gas phase and liquid phase.
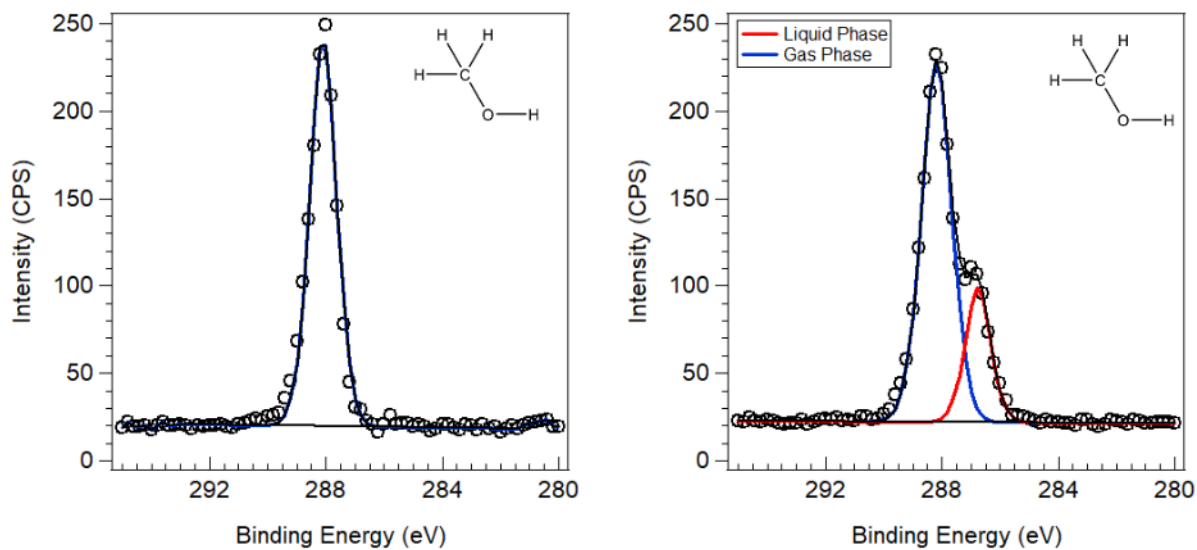
Figure 5.3: *C 1s spectra of gas phase (left) and liquid phase (right) methanol*

The strong peak due to the methanol gas phase shows a binding energy of 288.10 eV. When probing the methanol liquid jet, the gas phase peak occurs at 288.18 eV and the liquid phase peak is at a binding energy of 286.76 eV. The difference between the liquid and gas phase peaks is 1.42 eV. Acetic acid and acetamide were then dissolved in methanol at 5M concentration. Figure 5.4 below shows the resulting C 1s spectra of the gas phase and liquid phase of the solutions.
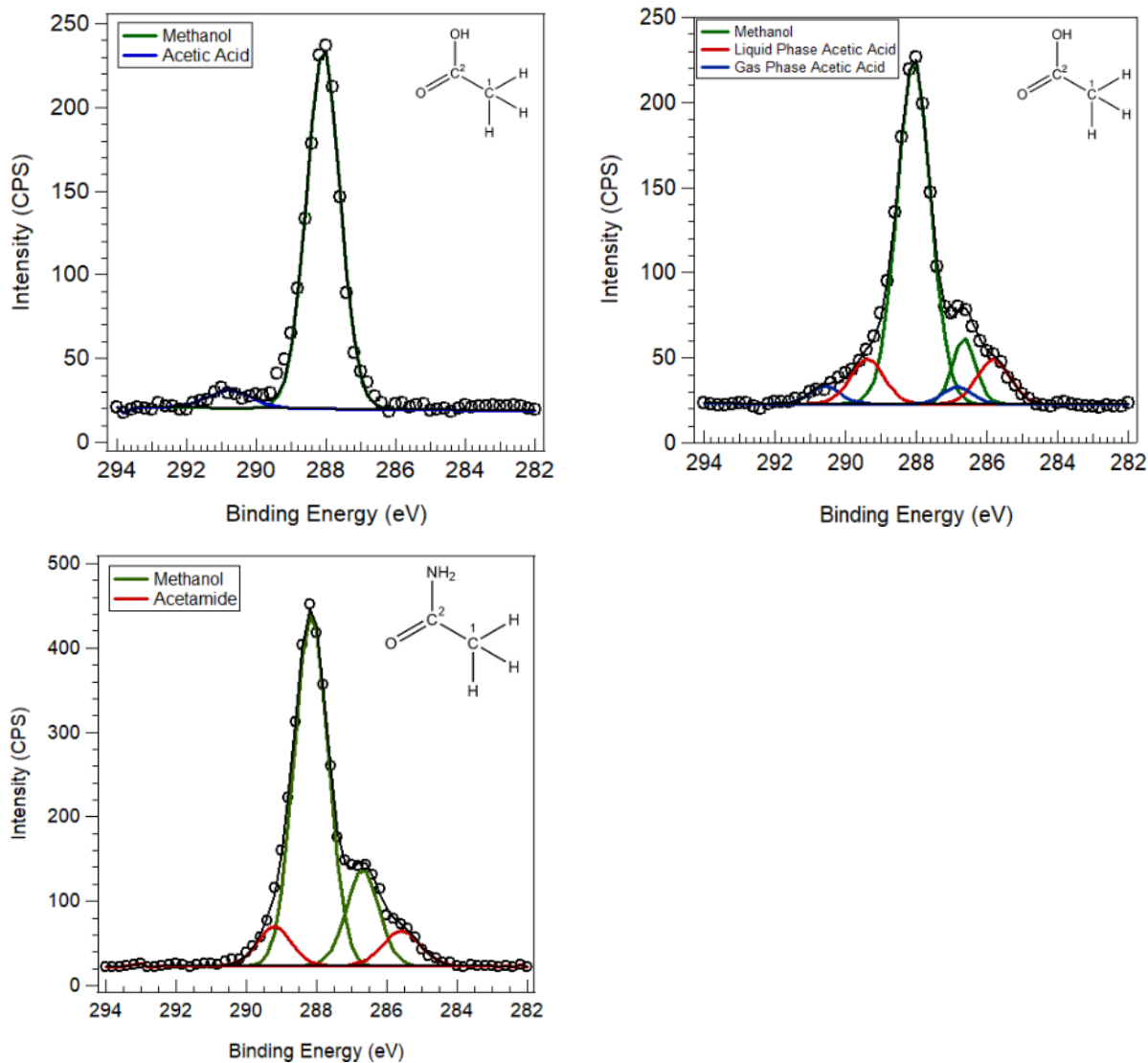
Figure 5.4: *C 1s spectra of gas phase and liquid phase of 5M acetic acid and acetamide dissolved in methanol.*

The different information gathered from the liquid phase C 1s spectrum of the acetic acid in methanol solution is summarized below.

Table 5.4: C 1s spectrum summary of acetic acid in methanol solution. All errors are calculated using a Monte Carlo simulation of the peak model with respect to the raw data. Errors for the ΔE are propagated from the peak error.

	C 1s gas phase		C 1s liquid phase		C 1s liquid phase acetamide	
	carbonyl peak	methyl peak	carbonyl peak	methyl peak	carbonyl peak	methyl peak
Binding Energy (eV)	290.58 ± 0.05	286.83 ± 0.08	289.38 ± 0.05	285.82 ± 0.04	289.20 ± 0.07	285.59 ± 0.08
FWHM (eV)	1.00 ± 0.12	1.00 ± 0.11	1.09 ± 0.09	1.10 ± 0.09	1.12 ± 0.11	1.26 ± 0.07
ΔE (eV)	3.75 ± 0.09		3.56 ± 0.06		3.61 ± 0.11	

The ΔBE of acetic acid is 3.75 eV in the gas phase and 3.56 eV in the solution phase, which is lower than the splitting for acetic acid dissolved in water. Acetamide showed a ΔBE of 3.61 eV which is larger than what is observed in aqueous solutions. The FWHM of all the peaks are smaller in comparison to the FWHM that are observed in aqueous solutions.

Discussion

Effect of Acetic Acid Electronic Structure on Aqueous Solvation

The substitution of different groups to the methyl carbon of the acetic acid moiety modifies the electronic structure and a shift is observed in ΔBE. ΔBE of the acetic acid is 3.84 eV, while the deuterated acetic acid is 3.67 eV, which is a decrease of 0.17 eV. This change is due to a differences in the vibrational coupling between the solvent and the acetic acid in solution. The FWHM value of the deuterated methyl C 1s is less than the hydrogen terminated species. This is also indicative of a change in vibrational broadening associated with the termination of deuterium rather than hydrogen. The carbonyl carbons have very similar FWHM and would not be subject to the same effect because of the fast exchange with the protons in the water. The ΔBE of trifluoroacetic acid is -2.64 eV, which comes from the large binding energy shift of the methyl

carbon terminated with fluorine groups. The carbonyl carbon binding energy is also shifted to higher binding energy by the fluorine atoms on the methyl carbon. In contrast to the acetic acid carbonyl binding energy at 291.00 eV, the trifluoroacetic acid carbonyl binding energy is 292.23 eV. The FWHM of the methyl carbon of the trifluoroacetic acid is 0.84 eV, likely due to the lack of interaction with the solvent at that end of the molecule that decreases the width of the peak. The width of the carbonyl peak of the trifluoroacetic acid (1.2 eV) is wider than the other species (~1 eV) and could be due to increased interaction with the solvent in response to the fluorine groups on the methyl carbon pulling electron density from the carbonyl carbon.

The ΔBE values of the liquid phase experiment are also calculated and tabulated from Figure 5.2 in Table 5.3. The acetic acid and deuterated acetic acid of the gas phase above the liquid jet show consistent ΔBE trends with the gas phase only spectra. The acetic acid ΔBE is 3.90 eV and the deuterated acetic acid is 3.84 eV, but are within error of one another with a difference of 0.06 eV. There may be some interaction of the liquid with the gas phase near the jet that does not generate a significant shift outside the error of measurement. Another possibility is that the vibrational coupling is only observable in the gas phase and the interactions with the solvent override the observable vibrational coupling. ΔBE for the trifluoroacetic acid in the gas phase (-2.73 eV) above the liquid jet is within error of the gas phase only spectrum. The error associated with that value is high compared to any of the other values. This is due to the low vapor pressure of trifluoroacetic acid generating a low intensity of photoelectrons from the gas phase.

The ΔBE of the acetic acid derivatives in the liquid phase increases compared to the gas phase due to the increased interactions with the solvent. ΔBE of acetic acid and deuterated acetic acid are the same within the estimated error with values of 4.02 eV and 4.11 eV respectively. The difference between the gas phase only ΔBE and liquid phase is an increase of 0.18 eV for acetic

acid and 0.44 eV for deuterated acetic acid. The interaction of the solvent with the deuterated species could give rise to the large increase in ΔBE for the liquid phase. ΔBE of the trifluoroacetic acid was -2.97 eV and shows a similar trend to the other liquid phase peaks with larger ΔBE associated with the liquid phase compared to the gas phase. The increase between the liquid phase ΔBE and gas phase is 0.33 eV, likely due to the increased solvent interaction with the molecule.

ΔBE of acetate is 3.49 eV as shown in Table 5.3. The low ΔBE for the acetate comes from the deprotonated hydroxyl oxygen on the carbonyl and increased interaction with the solvent. The binding energy of the acetate carbonyl carbon (288.95 eV) is lower than the carbonyl carbon of the acetic acid (289.64 eV). This shows that the acetic acid is protonated in both the gas phase and the liquid phase and that there is no contribution from the acetate in the aqueous spectrum. The methyl group also shows a small shift of 0.18 eV to lower binding energy which is a consequence of the deprotonation on the carbonyl group.

Acetamide, which has an amide group in place of the hydroxyl on the carbonyl carbon, shows a ΔBE of 3.27 eV in aqueous solution. The smallest ΔBE of all the derivatives stems from a different interaction of the solvent with the amide group in comparison to the carbonyl group. The hydroxyl on the carbonyl group is more acidic in comparison to the amide, while the nitrogen atom is a more competent hydrogen bond acceptor implying fundamentally different interactions with the solvent. The ΔBE may also indicate a more intimate solvation environment with the amide case as much of the electron density could be retained within the acetamide molecule.

The FWHM values of the liquid values for the methyl carbon of the deuterated acetic acid is higher than the acetic acid value, which is opposite to what is observed in the gas phase. It is not clear why the deuterium is higher in FWHM when dissolved in water. If the acetate is considered, the FWHM is very similar to the deuterium and could indicate a similar interaction with the

solvent. Trifluoroacetic acid was surprising with a carbonyl C 1s FWHM of 2.2 eV. This increase in FWHM could be due to the strong electron withdrawing fluorine groups on the methyl carbon that pull electron density out of the carbonyl group. With the decrease of electron density in the carbonyl group there will be a larger interaction with the solvent thereby increasing the FWHM at that carbon.

All relative integrated ratios between the methyl carbon and carbonyl carbon are 1:1 for all species in the liquid phase peaks in Figure 5.2. The relative ratio of the trifluoroacetic acid in the liquid phase is much higher than in the gas phase and can be explained by the low vapor pressure of that species. The peaks in the deuterated acetic acid are more resolved than in the acetic acid peaks, specifically in the carbonyl region. The reduced vibrational coupling associated with the deuterium – solvent interaction generates a lower FWHM on the peaks and leads to a better resolution, especially in the liquid phase.

Effect of Changing the Solvation Environment on the Electronic Structure of Acetic Acid

Dissolving acetic acid in an alcohol such as methanol has the potential to change the solvation environment significantly. Additionally, the concept of pH in non – aqueous solutions becomes convoluted as the interaction with the solvent and the reaction kinetics for proton donating/accepting interactions are intrinsically different from aqueous solutions. The photoelectron spectra of neat methanol solutions are shown in Figure 5.3. The liquid phase peak is clearly visible at 286.76 eV with a very narrow peak (1.03 eV) compared to the gas phase at 288.18 eV (1.21eV). This set of peaks were used to fit the C 1s of the acetic acid when it was dissolved in the methanol. All aspects of the methanol were constrained, and the remainder of the peak fit could vary in Figure 5.4b.

In Figure 5.4b, the C 1s is shown for acetic acid dissolved in methanol. The gas phase shows a very small carbonyl group at 291.05 eV. This peak is relatively similar, in terms of binding energy and overall area, to the others shown in Figure 5.2. The summary of the peak fit in Table 5.4 indicates the ΔBE between the carbonyl and methyl peak in the C 1s is significantly smaller than what is observed in the aqueous solutions. In the gas phase, the splitting is 3.75 eV and the liquid phase shows a splitting of 3.56 eV. The corresponding ΔBE in aqueous solution from Table 5.3 is 3.90 eV in the gas phase and 4.02 eV in the liquid phase. A comparison of the acetic acid in aqueous solution and in methanol solution is shown below in Table 5.5.

Table 5.5: *Comparison table of the C 1s photoelectron binding energies of acetic acid in both aqueous and methanol solutions*

	C 1s Gas Phase (eV)			C 1s Liquid Phase (eV)		
	Carbonyl	Methyl	ΔBE	Carbonyl	Methyl	ΔBE
Acetic Acid in Water	290.86 ± 0.09	286.96 ± 0.09	3.90 ± 0.11	289.66 ± 0.09	285.64 ± 0.07	4.02 ± 0.11
Acetic Acid in Methanol	290.58 ± 0.05	286.83 ± 0.08	3.75 ± 0.09	289.38 ± 0.05	285.82 ± 0.04	3.56 ± 0.06

There is no significant difference between the carbonyl carbon and the methyl carbon in the gas phase of the acetic acid in either solvation environment. This is not the case when the liquid phase is investigated. The carbonyl peak is shifted to lower binding energy in methanol solution whereas the methyl peak appears at higher binding energy relative to the aqueous solution. This result is very interesting as it appears that both ends of the molecule are affected by the solvent when it is dissolved in solution based on the C 1s binding energies. In comparison to aqueous solution, only the carbonyl group had any effect on the shifts in binding energy observed for the acetic acid, deuterated acetic acid and sodium acetate. The methanol has some hydrogen bonding to the acetic acid, but the effect is not as strong as in aqueous solution. The proton is still localized away from

the carbonyl carbon and therefore, retains more of its electron density causing the shift to lower binding energy. The lower binding energy from the methyl carbon indicates a loss of electron density in methanol compared to the aqueous solution. This is counterintuitive as the shift would be expected to be to a lower binding energy given that the carbonyl carbon is shifted to lower binding energy and the hydrogen bonding is still intact. However, if the solvation with methanol causes a deficiency of charge in the carbonyl group, this would cause a withdrawing of electron density out of the methyl group and a subsequent increase in the binding energy. This may also be the cause of the lower ΔBE observed in the methanol liquid phase rather than an increase, similar to what is observed with the aqueous solution. The methanol may also have some van der Waals interaction between the methyl carbon on the acetic acid and the -CH_3 end of the methanol.

Acetamide represents a different solvation interaction with the solvent compared to acetic acid. The acetamide ΔBE goes from 3.27 ± 0.04 eV to 3.61 ± 0.11 in methanol. This represents a significant change in the ΔBE, and solvation environment compared to acetic acid. The acetic acid ΔBE decreases in value when solvated in methanol, whereas for acetamide the opposite is observed. This may be due to fact that the acetamide has a hydrogen acceptor moiety in the amide group that can be more stabilized in an aqueous environment that has greater hydrogen bonding ability relative to methanol based on its equilibrium constant. This would then cause the amide group to become electropositive, drawing electron density away from the carbon atoms.

The opposite ΔBE shift to the acetamide compared to the acetic acid could also be a function of the acid/base identity of the molecule. It also follows from the previous discussion that the dominant equilibrium is proton donating from the acid and proton accepting for the base. The electronic structure of the molecule is sensitive to changes in pH of the surrounding enviroment, but the ΔBE measurement may give some insight into the acidity/basicity of a molecule if a trend

can be established. More work will need to be done with different solvent systems to understand the changes in ΔBE and its use in determination of acid/base molecules.

Electronic Structure Calculations, Molecular Dynamics (MD) Simulations and Acetic Acid Solvation

Molecular dynamics simulations were performed on the acetic acid solvated by both water and methanol, as well as acetate solvated by water. Electronic structure calculations were used in each configuration of the MD simulation to generate a difference in the binding energy between the carbonyl and methyl carbon (ΔBE). A summary of the ΔBE found using the electronic structure/MD simulations is shown below in Table 5.6.

Table 5.6: Summary of electronic structure calculation of ΔBE for acetic acid in water and methanol. Acetate is only solvated in water due to the low solubility in methanol restricting the experimental characterization

Number of Solvent Molecules	Acetic acid ΔBE in Water	Acetate ΔBE in Water	Acetic acid ΔBE in Methanol
Single Molecule	3.58	-	3.58
1	3.76 ± 0.17	-	3.72 ± 0.09
2	3.82 ± 0.16	2.95 ± 0.16	3.85 ± 0.16
3	3.77 ± 0.16	2.97 ± 0.17	3.61 ± 0.19
4	3.82 ± 0.18	3.01 ± 0.16	3.80 ± 0.16
Experiment Liquid	*4.02 ± 0.11*	*3.49 ± 0.06*	*3.56 ± 0.06*
Experiment Gas	*3.90 ± 0.11*	*-*	*3.75 ± 0.09*

ΔBE of acetic acid in the gas phase was calculated to be 3.58 eV. This is lower than the experimental value of 3.84 eV but may be corrected by taking vibrational effects into account, as it is much closer to the d^4 – acetic acid gas phase value of 3.67 eV. Addition of water molecules to the first solvation shell and calculating the ΔBE is what is shown in Table 5.6. The first column of Table 5.6 shows small deviations in the value of ΔBE; however, the change is all within error of the previous number of waters molecules used to solvate the molecule in solution. These values do not reproduce the gas phase ΔBE and will be used to determine the effect of solvation on the

acetic acid in aqueous solutions. The acetic acid will have 3 places to hydrogen bond to the solvent molecule directly; acceptors at the carbonyl oxygen and hydroxyl oxygen and a donator at the hydroxyl hydrogen. This would, as an initial starting point, indicate that a minimum of 3 water molecules could be needed to form the first solvation shell around the acetic acid. Comparison of the simulations to the experimental data indicate that the number of solvent molecules required to reproduce the experimental value within error is only 1 water molecule. The snapshots of the water interaction with the acetic acid are shown below in Figure 5.5.

1 water molecule   **2 water molecules**

3 water molecules   **4 water molecules**
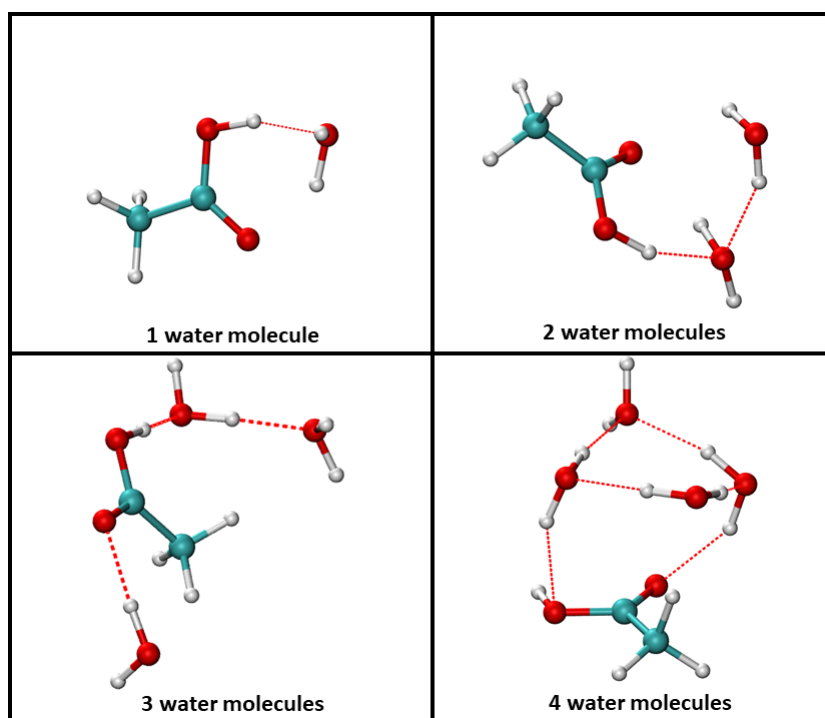
Figure 5.5: Snapshots of acetic acid with different numbers of water molecules from the MD simulations. These are representative of the results of the electronic structure calculations associated with ΔBE

The snapshots show the interaction with the acetic acid begins with the hydroxyl hydrogen and the water. When a second water molecule is added, there is no additional, direct interaction with the acetic acid, but rather the solvent molecule. This illustrates why the ΔBE does not shift significantly when adding a second water molecule. A third water molecule interacts with the

carbonyl oxygen of the acetic acid, causing a decrease in the ΔBE. It appears that any interaction with the carbonyl causes a decrease in the ΔBE of the acetic acid. When a fourth water molecule is added, there is no change in the direct interaction with the acetic acid, but the interaction between solvent molecules is modified and the ΔBE increases again. There is no interaction with the methyl group of acetic acid with the solvent molecules. Experimentally, the ΔBE increases from the gas phase to the liquid phase. The calculations capture this qualitative observation with a single water molecule being added to the simulation. Some reports in the literature indicate the first solvation shell of an acetic acid molecule in water is 4 – 5 water molecules under dilute conditions.[17] At the time of this writing, only 4 molecules were used in the simulation and we are currently investigating up to a 6-water system to test whether or not findings in the literature can be corroborated and lead to a defined solvation shell. The snapshots show that the interaction with the hydroxyl hydrogen with a single water molecule does encompass the effects observed experimentally, but a more complete picture may emerge when a full solvent shell is calculated. The water – water interaction does shift the ΔBE slightly in the calculations and could have a significant effect when more waters are added to the simulation.

Acetate was also simulated in water and its results are tabulated in the third column of Table 5.6. The ΔBE values for each number of water molecules underestimates the experimental value. Acetate is believed to contain upwards of 6 water molecules in its first solvation shell, and this may be the origin of the deviation.[16] This system is additional motivation for simulations with 6 water molecules, rather than relying on lower numbers of solvent molecules. Another probable cause for the low ΔBE values could be inherent to the DFT calculations that are used in the MD simulations. DFT often underestimates these values in highly charged systems, which the acetate

ion would be in this context. The addition of more water molecules to the simulation will help resolve the origin of the underestimated ΔBE of acetate in water.

Acetic Acid in methanol is the fourth column of Table 5.6. Experimentally, the ΔBE of the acetic acid in methanol is reproduced by the gas phase calculation. This is not true of the experimental gas phase ΔBE when acetic acid is dissolved in methanol. The ΔBE for the experimental results is 3.75 eV, while the gas phase calculation is 3.58 eV. There is a significant amount of methanol in the gas phase based on its large area C 1s contribution. There may be some interaction between the methanol in the gas phase and acetic acid. When methanol molecules are added to the simulation, the model does not reproduce the experimental liquid ΔBE value until 3 methanol molecules are added. It does, however, reproduce the gas phase ΔBE of the acetic acid in methanol, which could indicate interaction between acetic acid and methanol in the gas phase. Hydrogen bonding around the carboxylic acid will need to be achieved by a single solvent molecule for each possible site. The addition of a fourth methanol to the simulation does not reproduce the experimental value and is outside the error of both measurements. The 4 - methanol value is similar to the results when 1 or 2 methanol molecules are present. This could indicate that 3 methanol molecules form the ideal hydrogen bonding network around the acetic acid and adding a fourth may disrupt that first solvation shell resulting in an increase in ΔBE. The snapshots of the MD simulation are shown below in Figure 5.6.
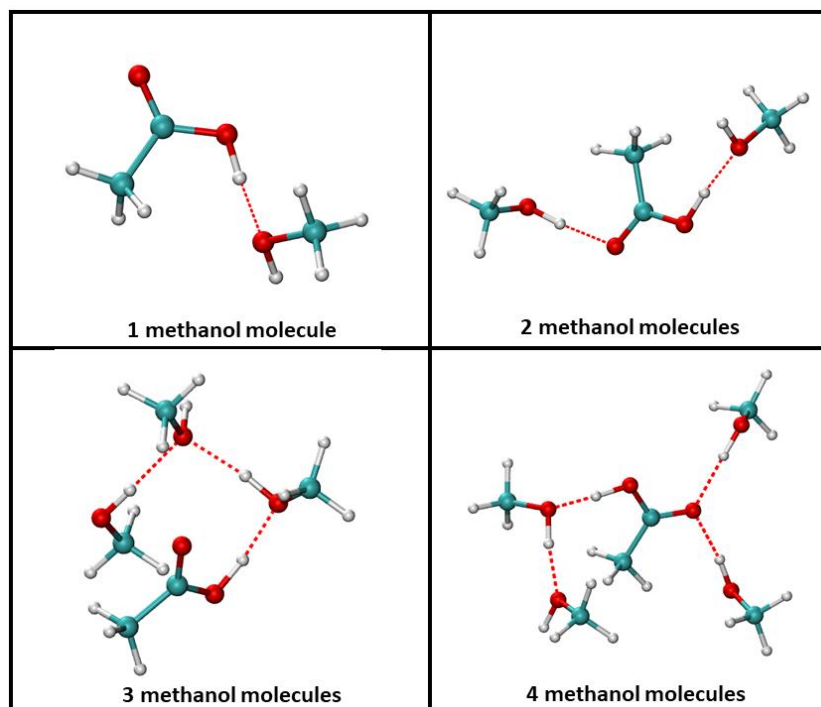
Figure 5.6: Snapshots of acetic acid with different numbers of methanol molecules from the MD simulations. These are representative of the results of the electronic structure calculations associated with ΔBE

Analogous to the interaction with water, the first methanol solvent molecule interacts with the hydroxyl hydrogen on the acetic acid. This causes an increase in the ΔBE from the single acetic acid molecule, which does not reproduce the observed qualitative experimental effect. The experiment shows the decrease of the ΔBE when acetic acid is in water. When a second methanol is added to the simulation, a second, direct interaction with the acetic acid is observed causing an increase in the ΔBE, consistent with the results for the water interaction with acetic acid. A third methanol shows greater solvent – solvent interaction and less direct interaction with the acetic acid. This configuration is one that reproduces the experimental ΔBE, as highlighted previously, and shows less direct interaction between the carbonyl oxygen of the acetic acid and more solvent – solvent interaction. When a fourth methanol is added, the interaction with the carbonyl oxygen appears again with less solvent – solvent interaction between the methanol molecules. The

corresponding ΔBE increases and no longer describes the experimental observation. There does not appear to be any interaction between the methanol solvent molecules and the methyl group of the acetic acid. The carboxyl group is where the solvent interaction is occurring, regardless of the identity of the solvent.

The qualitative ΔBE shift between the methanol and the water solvents is reproduced only in the water situation. Water causes an increase in ΔBE between the gas phase and the liquid phase acetic acid. Methanol shows a decrease in ΔBE experimentally, but an increase computationally. This may be another reason to increase the total number of solvent molecules. The solvent interaction does have a small effect on the ΔBE in the electronic structure calculation and the interaction of more solvent molecules may generate the desired qualitative effect observed experimentally.

Conclusion

Acetic acid was found to have different interactions in aqueous solution depending on the terminating groups on the methyl carbon. Hydrogenated, deuterated and fluorinated acetic acid were all investigated in aqueous solution. Deuterated acetic acid decreased the dipolar interactions with the solvent, causing a decrease in the carbonyl – methyl splitting. Acetic acid was also dissolved in methanol and showed lower splitting between the carbonyl and methyl carbon in solution compared to aqueous solution. This is due to a different solvation interaction between the acetic acid and the methanol at both the carbonyl and the methyl carbon ends of the molecule. MD simulations coupled with electronic structure calculations were also used to provide a molecular picture into the hydrogen bonding and solvation of the acetic acid in the different solvents. Water systems required only a single water molecule to describe the ΔBE observed experimentally.

Methanol solutions required 3 molecules of methanol to reproduce the experimental ΔBE and acetate was not reproduced at all in these calculations. Snapshots of the solvent interaction show the solvent molecules interacting with the carboxyl group only and no interaction with the methyl end of the acetic acid. Qualitative shifts in ΔBE are correctly predicted in water but are not in methanol. This shows that liquid jet XPS can be used to provide critical insight into the solvation environment of small molecules in different solutions and coupled with electronic structure calculations, can generate a detailed molecular understanding of the hydrogen bonding within solution.

References

1   M. Zhang, L. Chen, H. Yang and J. Ma, Theoretical Study of Acetic Acid Association Based on Hydrogen Bonding Mechanism, *J. Phys. Chem. A*, 2017, **121**, 4560–4568.

2   T. Takamuku, T. Yamaguchi, M. Asato, M. Matsumoto and N. Nishi, Structure of clusters in methanol-water binary solutions studied by mass spectrometry and X-ray diffraction, *Zeitschrift fur Naturforsch. - Sect. A J. Phys. Sci.*, 2000, **55**, 513–525.

3   A. Chebbi and P. Carlier, Carboxylic acids in the troposphere, occurrence, sources, and sinks: A review, *Atmos. Environ.*, 1996, **30**, 4233–4249.

4   P. I. Nagy, D. A. Smith, G. Alagona and C. Ghio, Ab initio studies of free and monohydrated carboxylic acids in the gas phase, *J. Phys. Chem.*, 1994, **98**, 486–493.

5   N. Fuson and M. Josien, Structure of the Associated OH Valence Vibration Band in Light and Heavy Acetic, Trichloroacetic, and Trifluoroacetic Acids*, *J. Opt. Soc. Am.*, 2008, **43**, 1102.

6   M. Śmiechowski, E. Gojło and J. Stangret, Hydration of simple carboxylic acids from infrared spectra of HDO and theoretical calculations, *J. Phys. Chem. B*, 2011, **115**, 4834–4842.

7   G. Ruderman, E. R. Caffarena, I. G. Mogilner and E. J. Tolosa, Hydrogen bonding of carboxylic acids in aqueous solutions - UV spectroscopy, viscosity, and molecular simulation of acetic acid, *J. Solution Chem.*, 1998, **27**, 935–948.

8   B. Winter and M. Faubel, Photoemission from Liquid Aqueous Solutions, *Chem. Rev.*, 2006, **106**, 1176–1211.

9   A. M. Margarella, K. A. Perrine, T. Lewis, M. Faubel, B. Winter and J. C. Hemminger, Dissociation of sulfuric acid in aqueous solution: Determination of the photoelectron

spectral fingerprints of H2SO4, HSO 4-, and SO42- in water, *J. Phys. Chem. C*, 2013, **117**, 8131–8137.

10   B. Winter, R. Weber, W. Widdra, M. Dittmar, M. Faubel and I. V. Hertel, Full Valence Band Photoemission from Liquid Water Using EUV Synchrotron Radiation, *J. Phys. Chem. A*, 2004, **108**, 2625–2632.

11   T. Lewis, B. Winter, A. C. Stern, M. D. Baer, C. J. Mundy, D. J. Tobias and J. C. Hemminger, Dissociation of Strong Acid Revisited: X-ray Photoelectron Spectroscopy and Molecular Dynamics Simulations of HNO3 in Water, *J. Phys. Chem. B*, 2011, **115**, 9445–9451.

12   T. Lewis, M. Faubel, B. Winter and J. C. Hemminger, CO2 Capture in Amine-Based Aqueous Solution: Role of the Gas-Solution Interface, *Angew. Chemie Int. Ed.*, 2011, **50**, 10178–10181.

13   N. Fairley and A. Carrick, *The Casa Cookbook*, 2005.

14   M. A. Brown, B. Winter, M. Faubel and J. C. Hemminger, Spatial Distribution of Nitrate and Nitrite Anions at the Liquid/Vapor Interface of Aqueous Solutions, *J. Am. Chem. Soc.*, 2009, **131**, 8354-+.

15   B. Winter, Liquid microjet for photoelectron spectroscopy, *Nucl. Instruments Methods Phys. Res. Sect. A Accel. Spectrometers, Detect. Assoc. Equip.*, 2009, **601**, 139–150.

16   M. A. Brown, R. D'Auria, I. F. W. Kuo, M. J. Krisch, D. E. Starr, H. Bluhm, D. J. Tobias and J. C. Hemminger, Ion spatial distributions at the liquid-vapor interface of aqueous potassium fluoride solutions, *Phys. Chem. Chem. Phys.*, 2008, **10**, 4778–4784.

17   M. V. Fedotova and S. E. Kruchinin, Hydration of acetic acid and acetate ion in water studied by 1D-RISM theory, *J. Mol. Liq.*, 2011, **164**, 201–206.

Chapter 6: Characterization of a Microfluidic Mixing Jet using X – ray Photoelectron Spectroscopy

Introduction

Chemical reactions can occur at different time scales. Techniques that can characterize the active chemical species in the reaction at these different times are critical to understanding the reaction mechanism. There are many different reactions that are dependent on the chemical environment of the reactants and may change as the reaction proceeds to completion. Microfluidic chambers are a way in which a chemical reaction can be controlled and measured at different time points while maintaining a small volume to prevent waste of large amounts of reactants.[1,2] Microfluidics have been used at free electron lasers and synchrotrons to investigate different chemical reactions using x – ray scattering techniques.[1–4]

The use of X – ray photoelectron spectroscopy (XPS) on solutions has opened up new opportunities to characterize the solutes in the bulk and surface regions of the liquid.[5–8] Furthermore, the sensitivity of XPS to the chemical environment and oxidation state of the solutes can provide a clear understanding of the transition of a reactant through a reaction scheme unlike any other technique. The coupling of a microfluidic mixing chamber that generates a liquid jet with the chemical sensitivity of XPS can provide new understanding of reactions that involve heterogeneous transformations at early time points. This information is crucial to a deeper understanding of reactions involving nanoparticle formation and will give new insights into nucleation theory of transition metals or other systems with changes in oxidation state.[9–12]

Before any characterization of complex solutions can take place, simple systems should be understood. The surface sensitivity of XPS creates a unique challenge when it comes to mixing of two or more streams in the microfluidic chamber. When a two-channel setup is used, there will be

a movement of solutes from the inner channel radially outward to the surface of the liquid jet. Additionally, solute in the outer channel will also move radially inward towards the center of the jet. Both processes, based on the speed and type of flow present in the jet, are expected to operate under a diffusion limited regime and careful characterization of the mixing jet under these conditions will be needed. The work described herein is a fundamental investigation of the surface of the mixing jet and will be used to further characterize more complex solutions in the future.

Experimental

The microfluidic mixing chamber schematics can be found in Appendix II. All solutions were made in aqueous solution with HPLC Grade water. NaI (99.99% trace metal basis, Sigma Aldrich) was dissolved in water at a concentration of 2M bulk concentration. A small amount of NaCl (0.02M) was added to prevent charging of the mixing jet. Initial experiments were conducted with NaI in one of the two channels while the other was filled with water. Two HPLC pumps were connected to the microfluidic inputs and were held at a constant total flow rate of 0.4 mL/min consistent with single jet measurements in the past unless otherwise stated.[13–15] The liquid jet temperature was not controlled, however the temperature of the jet is estimated to be ~6°C based on evaporative cooling. The background pressure of the chamber was held at 4 mbar during the experiment.

The core orbital of I 3d was taken with 0.2 eV step size, over 10 sweeps. O 1s was taken with 0.1 eV step size over 3 sweeps. All spectra were charge corrected to the O 1s water gas phase peak at 535.5 eV. Ratios of I3d/O1s were calculated using the procedure outlined in Chapter 2 and a standard calibration curve related to the concentration of NaI in water was created using a single channel jet. The effective concentration from the mixing jet was calculated from the standard curve and the I 3d/O 1s ratio.
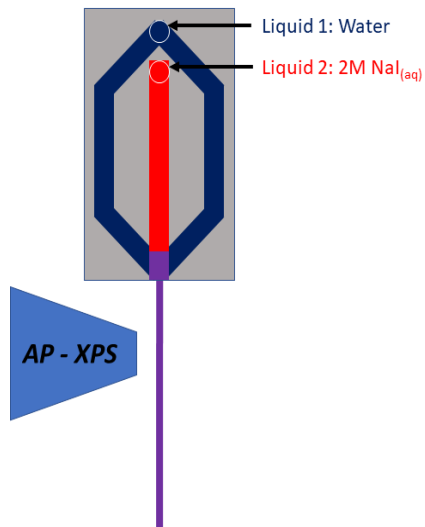
Results

Calibration Curve for NaI

A calibration curve of the NaI response of the I 3d peak vs. the concentration is shown below in Figure 6.1.
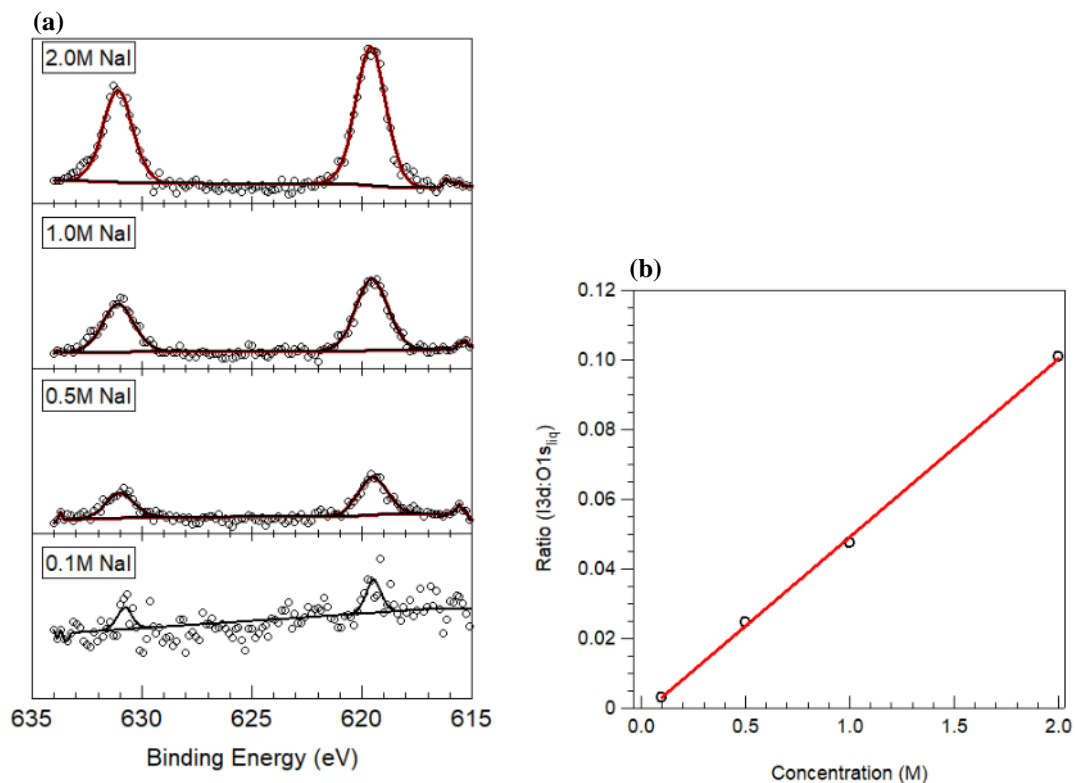
Figure 6.1: *(a) I 3d photoelectron spectra of different concentrations. (b) Calibration curve of I3d: O1s$_{liq}$ peaks as a function of the concentration.*
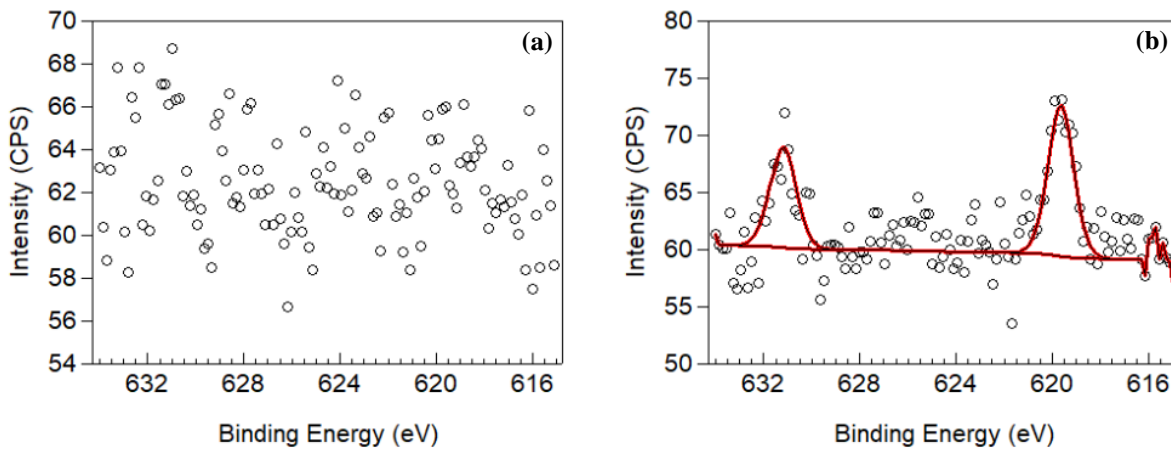
The change in concentration shows a linear response of the XPS I3d: O1s$_{liq}$ ratio. The linear fit of the data is shown in Figure 6.1a. This fit is then used as the basis to calculate an effective concentration of the mixing jet response in the photoelectron peaks. The flow rate of the single jet was 0.4 mL/min.

Figure 6.2: *Schematic of the Mixing Jet. The two channels are separate until they are brought together to form the mixed jet. A similar figure is found in Appendix II.*

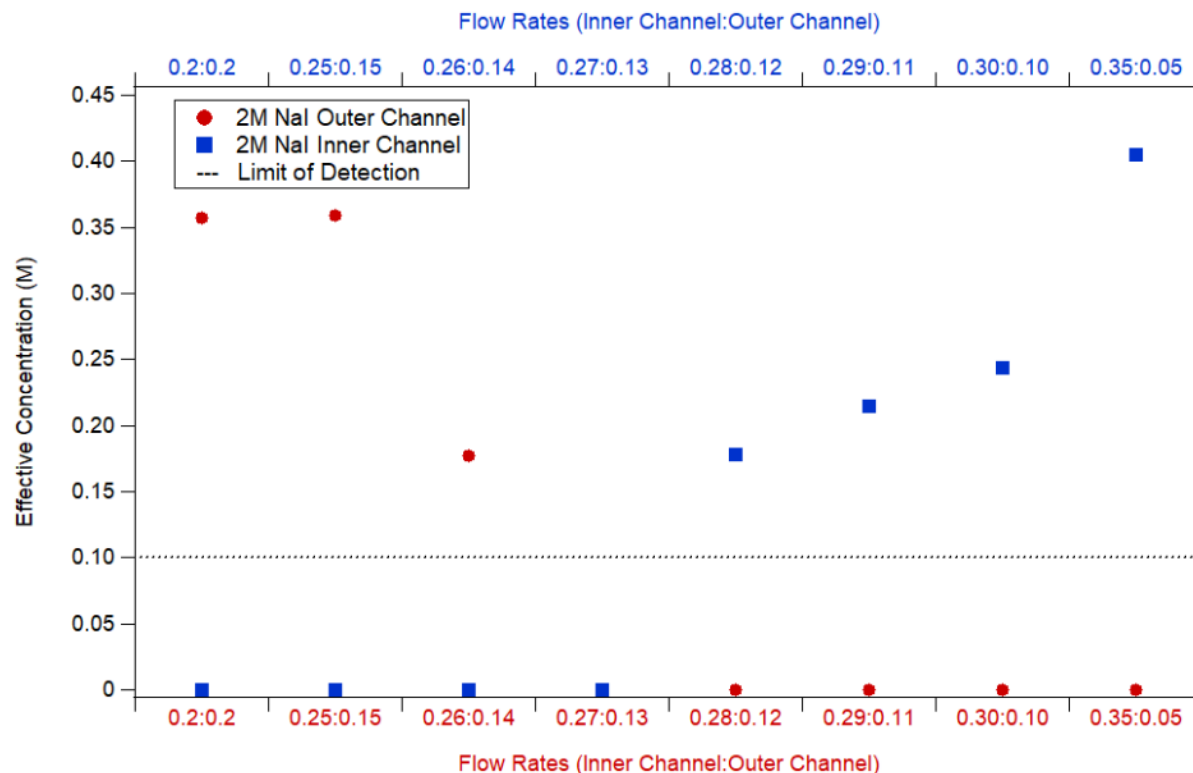**Calibration of the Mixing Jet**

In Figure 6.2, the schematic of the mixing chamber is shown to illustrate the two channels and how they will be mixed to create the mixing jet. Either channel can have a distinct liquid contained within it prior to mixing. In this case we chose to use NaI because of the high X- ray cross section and surface propensity of the I⁻ ion.[13,16–20] A 2M concentration was also chosen to fit within the calibration curve and would be responsive to any dilution changes induced by the mixing. The first test was to look for that response. Figure 6.3 shows the initial change in concentration when the flow rates were changed between the inner channel (2M $NaI_{(aq)}$) and the outer channel (water).

Figure 6.3: *I 3d spectra for the mixing jet when (a) Flow rates between the inner channel and outer channel are 0.2 mL/min respectively. (b) Flow rates for the inner channel and the outer channel are 0.3 mL/min and 0.1 mL/min respectively.*

There is a distinct change in the response to I⁻ concentration as a function of relative flow rate. This can be used to modify the mixing ratio and ensure the solution is fully mixed prior to any characterization of the liquid jet by photoelectron spectroscopy. In Figure 6.4, the mixing was characterized by changing the relative flow rates and whether the NaI was in the inner channel or the outer channel at a constant overall flow rate of 0.4 mL/min.

Figure 6.4: *Concentration response of the mixing jet as a function of the relative flow rates in each of the channels. The effective concentration is calculated using the calibration curve in Figure 6.1b.*

The effective concentration in Figure 6.4 was found by using the I3d: $O1s_{liq}$ ratio in the calibration curve and calculating a concentration from the slope of the line. Figure 6.4 also shows the difference in whether the NaI was in the outer channel or the inner channel at different flow rates. At 0.2 mL/min for both inner and outer channels and if the NaI was in the outer channel, the effective concentration decreased approximately 3x. When NaI was in the inner channel, the ratio was below the limit of detection and no signal was detected. The opposite is true when the inner

channel had 0.35 mL/min and the outer channel was run at 0.05 mL/min. At different relative flow rates between the inner and outer channel, the concentration can be varied and controlled. Another parameter that may be used is the total flow rate of the jet. A slower flow rate allows for a longer mixing time prior to exiting the channel. A relative flow rate of 0.28 mL/min in the inner channel and 0.12 mL/min in the outer channel was chosen for the 0.4mL/min as it was near the limit of detection. In Figure 6.5, the total flow rate of the jet was changed while the relative flow rates remained constant throughout the experiment.
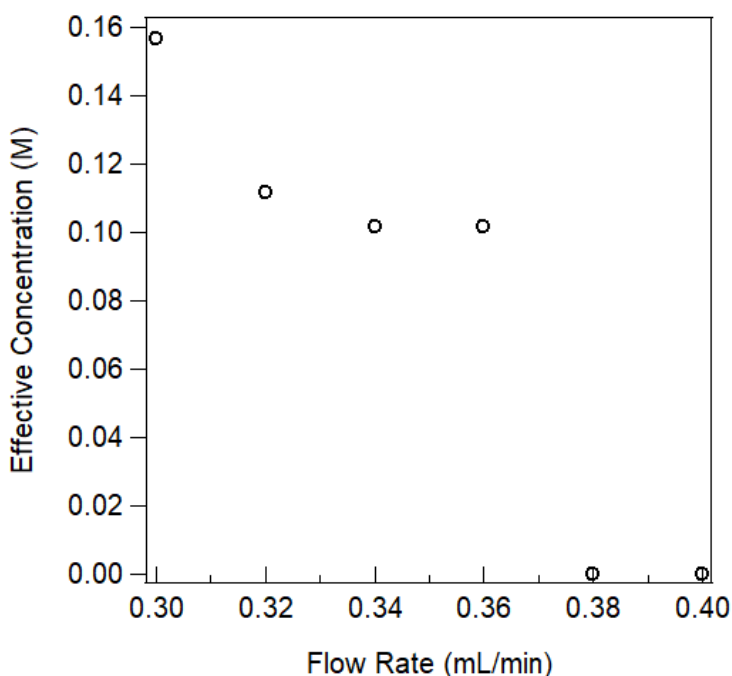
Figure 6.5: *Total flow rate change of the mixing jet to observe any changes in the effective concentration. This mixing chamber was a different microfluidic chip than the previous plot in Figure 6.4.*

This shows that the total flow rate can be decreased, and lower effective concentrations can be observed. The I 3d signal is not observed at the initial flow rate of 0.40 mL/min, but was clearly observed beginning at 0.36 mL/min. There is a slight increase in the signal at 0.32 mL/min and a significant increase to the previous ratio in Figure 6.4 at 0.30 mL/min. The experiment may be optimal at a flow rate of 0.30 mL/min rather than the 0.40 mL/min run previously. At the higher

flow rates, a longer mixing channel will need to be used. In this experiment, a mixing channel of 95 µm was used.

Discussion

**Mixing and a Model for Quantifying Dilution Factors**

What is clear from the data gathered to this point is that the different mixing ratios can be controlled by changing the relative flow rates between the two channels. Quantification of the dilution factors based on the observed ratios is the next step in fully characterizing the mixing jet. The two channels meet and mix as they travel down the 95 µm channel (in the chips that were used herein) until they finally exit the end of the chip. A cross sectional schematic illustrating the jet as the inner flow rate is changed is shown below in Figure 6.6.
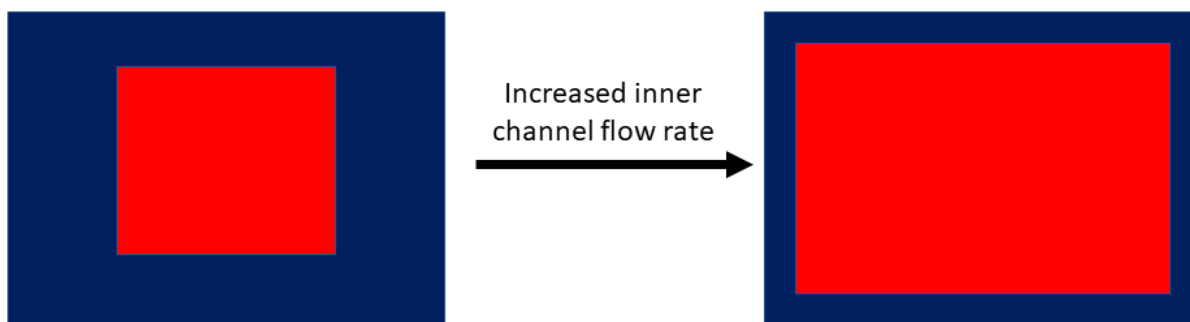
Figure 6.6: *Cross – sectional schematic of the mixing jet. The red represents the central channel whereas the blue represents the outer channel. Increasing the inner channel flow rate increases the overall contribution of the red to the total jet area.*

Both the inner and outer channels are in a laminar flow regime and not in a turbulent flow based on the flow rates used during the experiment. As the inner flow rate is increased, there is a subsequent increase in the size of the area of the red that represents the inner channel. A fully mixed jet would be achieved when the above condition is met in Figure 6.6 and the remaining change in concentration is solely due to diffusion. A diffusion limited condition can only be

manipulated by changing the relative flow rates and by modifying the amount of mixing time prior to analysis. Different lengths of mixing channels are available. For consistency, we limited our experiments to the 95 µm mixing channel. Since the measurements are surface sensitive, the analysis depth only reaches to a maximum of ~ 10 nm from the jet surface.[7] This puts another limitation on the experiment that even though a large majority of the jet may be mixed, the surface of the jet may not be. If the cross – sectional area of the inner channel is not large enough the experiment is limited by diffusion and no analyte is detected. An illustration of this consideration is shown in Figure 6.7 below.
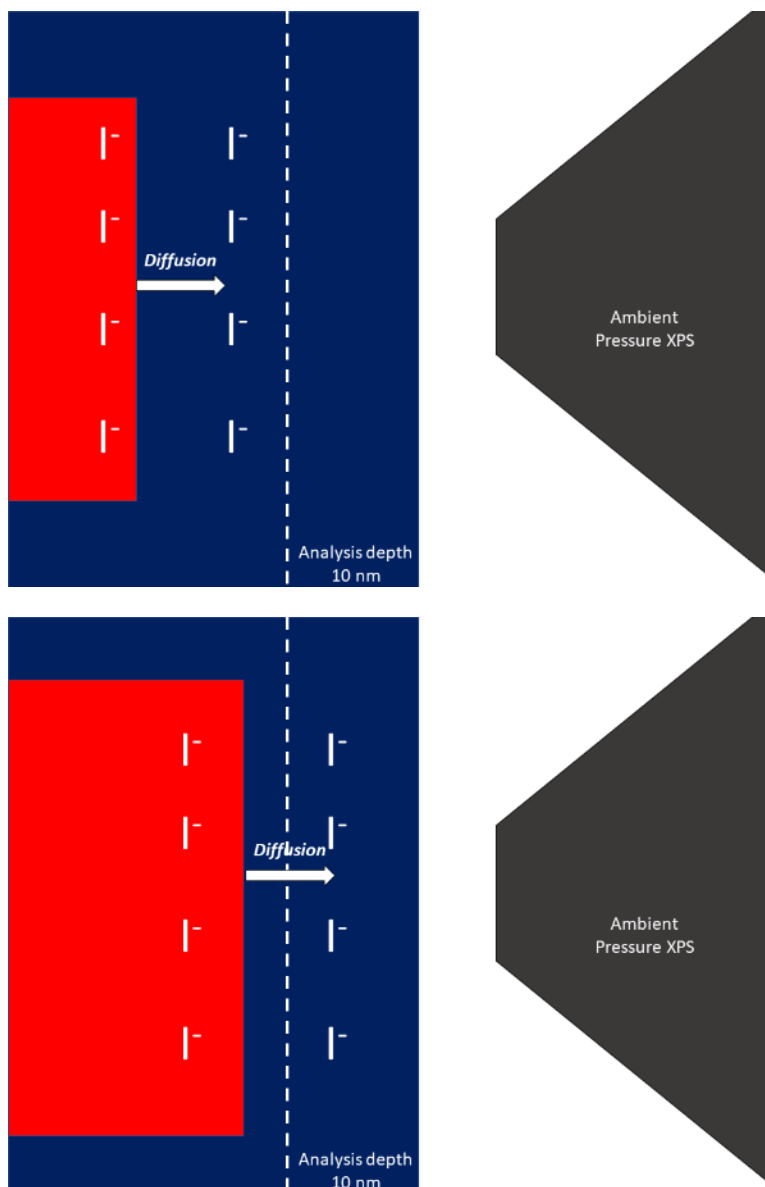
Figure 6.7: Two diffusion limited conditions for detecting the I 3d signal in the XPS over the same mixing time period. In the upper figure, the area defined by the inner flow rate is not high enough for diffusion to carry I^- into the analysis depth. In the lower figure, the inner flow rate is high enough to remove the diffusion limited condition and I^- is detected.

At high enough inner channel flow rates, the I 3d signal will be detected as the I^- is no longer under a diffusion limited condition. This can be observed in Figure 6.4 with the NaI in the inner channel represented by the blue squares. There is a flow rate dependence on the signal observed and once the area of the inner channel is high enough, the distance between the concentrated inner channel

area and the analysis area is short enough that a signal is observed. If, as in Figure 6.4, the NaI is in the outer channel this creates a dilution condition where the inner channel then causes a dilution of the analyte in the outer channel. This occurs at a low relative flow rate increase of the inner channel (0.26 mL/min). The immediate dilution of the outer channel indicates a fully mixed jet due to the response of the signal to the flow rate. If there were no mixing at the outer edges, the concentration would not change.

The total flow rate dependence is notable. Given the length of the mixing channel is 95 µm and the cross section of the channel is 10 µm x 25 µm, we can calculate a resonance time for the solution within the channel. No signal is observed for the 0.40 and 0.38 mL/min flow rates and the first observation of the signal is at 0.36 mL/min. The total volume of the channel given the above dimensions is 2.375×10^{-8} mL and has a resonance time of 3.958 µsec. The diffusion constant of I⁻ is 2.045×10^{-9} m^2/sec. Therefore, the distance travelled by an I⁻ is 89.97 nm during the mixing in the channel. I 3d occurs at a binding energy of 620 eV and with the Al kα excitation source this gives a kinetic energy of the electron of ~860 eV which translates to approximately 5 nm of analysis depth.[21] A summary table of the calculated resonance time and the distance travelled is shown in Table 6.1 below. The 6 different flow rates give a distance travelled by the I⁻ in solution. Based on the analysis depth of the I 3d (5 nm), a total flow rate change of 0.04 mL/min would constitute a full probe depth based on a 95 µm mixing channel.

Table 6.1: *Summary of Flow Rate Data. Resonance time is based on 95 μm mixing channel. Distance travelled is based on the diffusion constant of I⁻. Italicized numbers gave above background signal for I 3d XPS.*

Flow Rate (mL/min)	Linear Velocity (m/sec)	Resonance Time (sec x 10⁻⁶)	Distance Travelled (nm)
0.40	26.67	3.56	85.35
0.38	25.33	3.75	87.57
0.36	*24.00*	*3.96*	*89.97*
0.34	*22.67*	*4.19*	*92.58*
0.32	*21.33*	*4.45*	*95.43*
0.30	*20.00*	*4.75*	*98.56*

* Based on an I⁻ diffusion constant of 2.045×10^{-9} m²s⁻¹

Based on the variability in the geometry of the mixing chips used, the correct dilution factor has yet to be accounted for. Our initial strategy was to use the cross-sectional area as a metric for calculating the dilution factor; however, the values calculated based on this are not consistent with the experimental results. There may be other aspects of the diffusion that have yet to be considered when calculating the mixing concentration.

Conclusion

A microfluidic mixing jet with NaI was used for the first time in an X – ray photoelectron experiment. Two channels are brought together with different analytes and are considered fully mixed as operate only under diffusion limited conditions in the axial dimension. Different flow rates between the two channels were used to control the concentration observed in the photoelectron spectrum of iodine. The total flow rate was used to show the mixing was under diffusion limited conditions and that slower total flow rates may be needed based on the dimensions of the microfluidic chamber. These experiments will provide the foundation for which mixing experiments and pH jumps can be investigated using liquid jet photoelectron spectroscopy.

References

1   B. Marmiroli, G. Grenci, F. Cacho-Nerin, B. Sartori, E. Ferrari, P. Laggner, L. Businaro and H. Amenitsch, Free jet micromixer to study fast chemical reactions by small angle X-ray scattering, *Lab Chip*, 2009, **9**, 2063–2069.

2   J. A. Faust and G. M. Nathanson, Microjets and coated wheels: versatile tools for exploring collisions and reactions at gas–liquid interfaces, *Chem. Soc. Rev.*, 2016, **45**, 3609–3620.

3   B. Marmiroli, G. Grenci, F. Cacho-Nerin, B. Sartori, P. Laggner, L. Businaro and H. Amenitsch, Experimental set-up for time resolved small angle X-ray scattering studies of nanoparticles formation using a free-jet micromixer, *Nucl. Instruments Methods Phys. Res. Sect. B Beam Interact. with Mater. Atoms*, 2010, **268**, 329–333.

4   D. P. DePonte, U. Weierstall, K. Schmidt, J. Warner, D. Starodub, J. C. H. Spence and R. B. Doak, Gas dynamic virtual nozzle for generation of microscopic droplet streams, *J. Phys. D. Appl. Phys.*, 2008, **41**, 195505.

5   B. Winter and M. Faubel, Photoemission from Liquid Aqueous Solutions, *Chem. Rev.*, 2006, **106**, 1176–1211.

6   A. M. Margarella, K. A. Perrine, T. Lewis, M. Faubel, B. Winter and J. C. Hemminger, Dissociation of sulfuric acid in aqueous solution: Determination of the photoelectron spectral fingerprints of H2SO4, HSO 4-, and SO42- in water, *J. Phys. Chem. C*, 2013, **117**, 8131–8137.

7   S. Thurmer, R. Seidel, M. Faubel, W. Eberhardt, J. C. Hemminger, S. E. Bradforth and B. Winter, Photoelectron Angular Distributions from Liquid Water: Effects of Electron Scattering, *Phys. Rev. Lett.*, , DOI:10.1103/PhysRevLett.111.173005.

8   M. A. Brown, B. Winter, M. Faubel and J. C. Hemminger, Spatial Distribution of Nitrate
        and Nitrite Anions at the Liquid/Vapor Interface of Aqueous Solutions, *J. Am. Chem.
        Soc.*, 2009, **131**, 8354–+.

9   N. T. K. Thanh, N. Maclean and S. Mahiddine, Mechanisms of Nucleation and Growth of
        Nanoparticles in Solution, *Chem. Rev.*, 2014, **114**, 7610–7630.

10   J. A. Widegren, J. D. Aiken, S. Özkar and R. G. Finke, Additional Investigations of a New
        Kinetic Method To Follow Transition-Metal Nanocluster Formation, Including the
        Discovery of Heterolytic Hydrogen Activation in Nanocluster Nucleation Reactions,
        Chem. Mater., 2001, **13**, 312–324.

11   L. D. Marks and L. Peng, Nanoparticle shape, thermodynamics and kinetics, *J. Phys.
        Condens. Matter*, 2016, **28**, 53001.

12   M. A. Watzky and R. G. Finke, Transition Metal Nanocluster Formation Kinetic and
        Mechanistic Studies. A New Mechanism When Hydrogen Is the Reductant: Slow,
        Continuous Nucleation and Fast Autocatalytic Surface Growth, *J. Am. Chem. Soc.*, 1997,
        119, 10382–10400.

13   M. A. Brown, R. D'Auria, I. F. W. Kuo, M. J. Krisch, D. E. Starr, H. Bluhm, D. J. Tobias
        and J. C. Hemminger, Ion spatial distributions at the liquid-vapor interface of aqueous
        potassium fluoride solutions, *Phys. Chem. Chem. Phys.*, 2008, **10**, 4778–4784.

14   K. A. Perrine, M. H. C. Van Spyk, A. M. Margarella, B. Winter, M. Faubel, H. Bluhm and
        J. C. Hemminger, Characterization of the acetonitrile aqueous solution/vapor interface by
        liquid-jet X-ray photoelectron spectroscopy, *J. Phys. Chem. C*, 2014, **118**, 29378–29388.

15   M. J. Makowski, R. P. Galhenage, J. Langford and J. C. Hemminger, Liquid-Jet X-ray
        Photoelectron Spectra of TiO2 Nanoparticles in an Aqueous Electrolyte Solution, *J. Phys.*

Chem. Lett., 2016, **7**, 1732–1735.

16   B. Winter and M. Faubel, Photoemission from liquid aqueous solutions, *Chem. Rev.*,
      2006, **106**, 1176–1211.

17   P. Jungwirth and D. J. Tobias, Ions at the air/water interface, *J. Phys. Chem. B*, 2002, **106**,
      6361–6373.

18   P. Jungwirth and B. Winter, Ions at Aqueous Interfaces: From Water Surface to Hydrated
      Proteins, *Annu. Rev. Phys. Chem.*, 2008, **59**, 343–366.

19   N. Ottosson, M. Faubel, S. E. Bradforth, P. Jungwirth and B. Winter, Photoelectron
      spectroscopy of liquid water and aqueous solution: Electron effective attenuation lengths
      and emission-angle anisotropy, *J. Electron Spectros. Relat. Phenomena*, 2010, **177**, 60–
      70.

20   D. J. Tobias and J. C. Hemminger, Chemistry - Getting specific about specific ion effects,
      Science (80-.)., 2008, **319**, 1197–1198.

21   J. J. Yeh and I. Lindau, Atomic subshell photoionization cross sections and asymmetry
      parameters: $1 \leq Z \leq 103$, *At. Data Nucl. Data Tables*, 1985, **32**, 1–155.

Chapter 8: Conclusions and Future Directions

The work presented throughout this thesis has shown the versatility of X – ray photoelectron spectroscopy when it comes to solid, liquid and gas samples. In Chapter 3, XPS was used to demonstrate the consequences of photodeposition/photoreduction of Pt on TiO_2 nanoparticles and was also used under near ambient conditions to understand how a well – known CO oxidation catalyst at the nanoscale differs from a bulk catalyst of the same material. In subsequent chapters, XPS was used to characterize different liquid interfaces to investigate the effect of small halides on the coordination sphere of Fe^{2+} and the solvation change of acetic acid in different solvents. It was also used to show that mixed solutions could be characterized, which opens a new direction for liquid interface processes.

One specific area of research that I think the mixing jet will contribute to will be the chemical events of early nanoparticle formation. We have proposed this from the beginning of our project and with the groundwork completed in Chapter 6, this would be a high – impact area to focus our efforts in the future. Initially, Fe oxide nanoparticles were considered as the ideal candidates to investigate with the mixing jet. Unfortunately, Fe chlorides used in most aqueous nanoparticle syntheses are quite caustic and did not form a consistent jet. They also required very acidic conditions, especially the Fe^{3+} species, to prevent premature particle formation in the loops. Instead ZnO nanoparticles were proposed as a more suitable alternative. $Zn(NO_3)_2$ aqueous solutions were characterized as created and are a more ideal candidate compared to the Fe oxides. Ni oxides could also be considered as their aqueous solutions are more suitable to create the liquid jet. A pH jump using NaOH would be used to induce nanoparticle formation of the oxides from the as prepared solution. The transition metal would be in the outer channel closest to the surface and the hydroxide would move through solution to the surface of the liquid jet, triggering oxidation and nucleation

of the metal at the interface. These events at the optimized time scale would then be investigated using XPS and provide crucial information at the early stages of nucleation and nanoparticle formation.

Early work has already been completed for the Zn system using a single liquid jet without mixing. In Figure 1 below, the Zn 2p region is shown for 3M $Zn(NO_3)_2$.
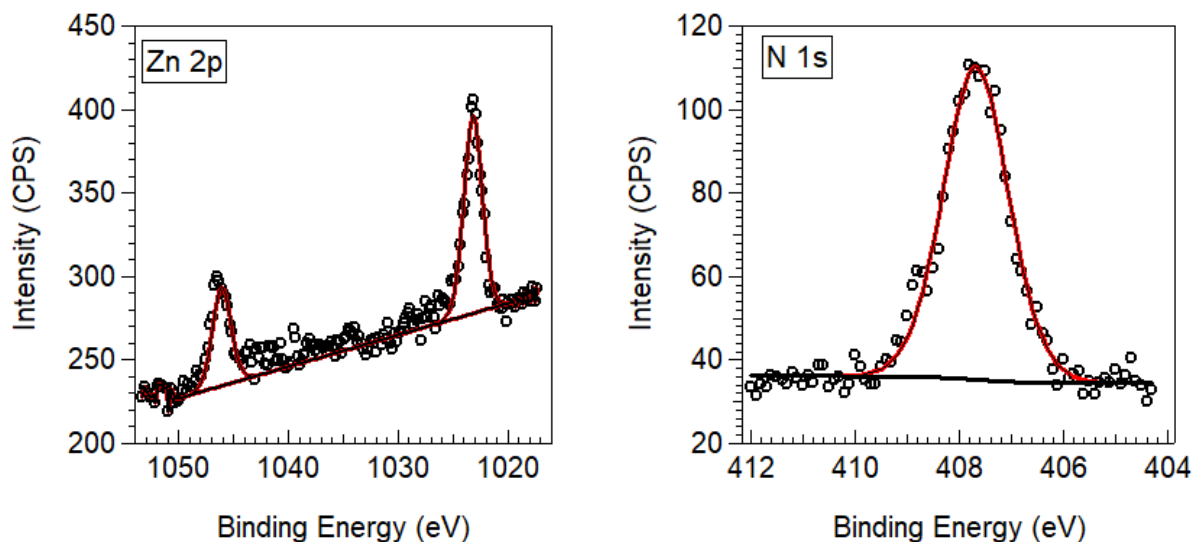
Figure 7.1: Zn 2p and N 1s spectra of Zn(NO₃)₂ in aqueous solution. The pH of the 3M Zn(NO₃)₂ solution was 4.3.

The Zn 2p binding energy of the $2p_{3/2}$ peak is 1023.18 eV which indicates a Zn^{2+} species in solution. There are no shoulders present on the peak and the pH was found to be 4.3. The species that is most likely to be present is the $[Zn(H_2O)_6]^{2+}$ and based on the equilibrium constant (1 x 10^{-9}) would not show a concentration of the $[ZnOH(H_2O)_5]^+$ high enough to be detected. In the N 1s spectra, the binding energy of the single N 1s peak is 407.38 eV which has been observed for nitrates in aqueous solutions.[1] These spectra would then be used to monitor the formation of ZnO in nanoparticle form when the solution is mixed with a high concentration of OH⁻. This mixing event is what we are calling a "pH jump" in solution and could be used in conjunction with the XPS to monitor these reactions. We have shown in Chapter 4 that Fe^{2+} shows small changes in binding energy when coordinated with electron withdrawing halides. The coordination and

eventual precipitation of $Zn(OH)_2$ should produce a binding energy shift associated with that event in the Zn 2p region. The signal – to – noise at 3M concentration appears adequate, though lower concentrations will also need to be investigated because of the mixing event and subsequent dilution of the metal in the solution.

Once the photoelectron spectra have been characterized for the mixing, X – ray absorption (XAS) studies similar to work in the literature on Fe^{3+} can be done to understand more of the solution chemistry that occurs during the nucleation process.[2] This work in conjunction with X – ray scattering work will give a full picture of what chemistry is occurring at early reaction times and how it gives rise to different nanoparticles in solution.

References

1   M. A. Brown, B. Winter, M. Faubel and J. C. Hemminger, Spatial Distribution of Nitrate

and Nitrite Anions at the Liquid/Vapor Interface of Aqueous Solutions, *J. Am. Chem.*

Soc., 2009, **131**, 8354–+.

2   H. Ali, R. Seidel, M. N. Pohl and B. Winter, Molecular species forming at the α-

Fe2O3nanoparticle-aqueous solution interface, *Chem. Sci.*, 2018, **9**, 4511–4523.

Appendix I: Lab – based Liquid Jet XPS Schematics and Standard Operating Procedures

The ambient pressure liquid jet X – ray photoelectron spectrometer is the first lab – based instrument in the world. The instrument was designed and built in collaboration with SPECS Gmbh out of Germany. SPECS has a US – based office that has been very helpful during some minor maintenance issues and should be contacted prior to any maintenance request. They have a file on this instrument (AU150380 California Irvine) that can be consulted for any prior maintenance.

This appendix will be a step – by – step guide to liquid jet experiments. Small tips and tricks will be shown throughout the guide to help with common issues that often arise in this work.

Start up

Prior to any liquid jet experiments, the HPLC pump and trap need to be primed and cooled, respectively. The cold trap uses approximately 500 mL of saturated NaCl solution to keep the background pressure low. A saturated NaCl solution is created by adding NaCl while stirring until there are small, undissolved crystals that remain. The trap is also set to -5°C rather than -10°C in previous experiments in the literature.[1–3] I have found this prevents any freezing of the jet from the trap up and keeps the background pressure low enough to be controlled by the vacuum pump on the small sample chamber.

Priming of the HPLC pump should be done prior to starting the pump. Figure 1 shows the HPLC pump from the front view.
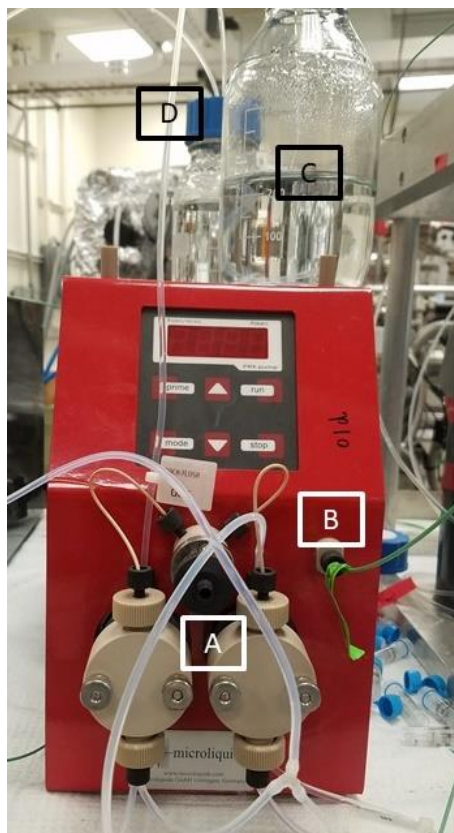
Figure AI.1: Front view of HPLC pump. (a) purge valve (b) outlet to loop (c) reservoir of water (d) back flush solution of 20% v/v methanol in water

The purge valve shown in Figure 1a should be opened and the flow rate should be set above 3 mL/min for the prime. Figure 1b should be replaced with a blank insert and will be isolated from the loops. Figure 1c should have at least 500 mL of pure HPLC grade water in the reservoir to prevent any damage. Figure 1d should be a 20% aqueous solution of methanol by volume. This back-flush solution is important for the heads of the peristaltic pump and should not have any bubbles within the lines. Both lines that go into Figure 1d should be submerged within the methanol solution. Once the purge valve is open and the flow rate is set, take a large (60 mL) empty syringe and place it on the outside of the purge valve. Run the pump and slowly pull solution through the closed system. The air bubbles that may be present in the reservoir lines and the back – flush lines should be removed from the system. A minimum volume of 30 mL should be drawn

out of the reservoir to prime the pump. I have also drawn a full syringe (60 mL) out of the reservoir

if the air bubbles are still there after the 30 mL. Once you're satisfied with the removal of the air

from the line, turn off the pump and close the purge valve. The pump can then be attached back to

the loops by replacing the blank in Figure 1b with the external line. You are now ready to start

generating a liquid jet.

Liquid Jet

Once the pump has been primed, it is ready to generate a liquid jet. The HPLC pump generates

this jet by pressure flow from the pump that is pushed through a small glass capillary. The diameter

of the capillary exit is ~ 20 µm but can vary. A good check is to generate the jet and take a light

microscope image to measure the diameter. A good jet is one that looks like Figure 2 and shows

no change in the back pressure of the HPLC pump. To find out how much pressure is being

generated with the jet press the "mode" button on the jet until the display reads "bar" as the unit.
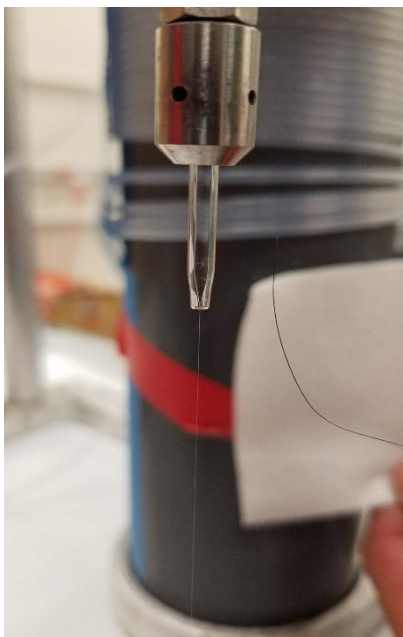
Figure AI.2: *Liquid jet generated with HPLC pump. The capillary generates a 20 µm diameter jet.*

If the pressure on the jet is greater than "0" on the "old" HPLC pump or "5" on the other HPLC pump, then there are a few parts to check prior to beginning. The first is the inline filter prior to the vacuum flange, this will often get clogged with particulate matter and needs to be changed on a regular basis. New filters can be purchased from VWR under the catalog number of 53501-222 which is A-706, 2µm inline filter from IDEX Health and Science. If this does not decrease the pressure to the values above, there is likely a clog in the capillary tube. Attempting to clear the capillary can be a time intensive endeavor. Strong acids (HCl or H_2SO_4) can be used however sonicating the capillary tubes in isopropanol and slowing increasing the water concentration seems to work best. The IPA has a low surface tension and can easily go into the small opening. Once the clog has been cleared and the pressure has been stable at the values above, the liquid jet can be placed into the chamber.

Standard Operating Procedures for LJ – XPS

Figure 3 is the schematic of the valve setup for the ambient pressure XPS. All the SOPs are based off this diagram. There are different procedures based on the status of the instrument. The different statuses are: Normal and Jet, with normal indicating there is no liquid jet in the sample chamber whereas the Jet will be when there is a jet in the sample chamber.
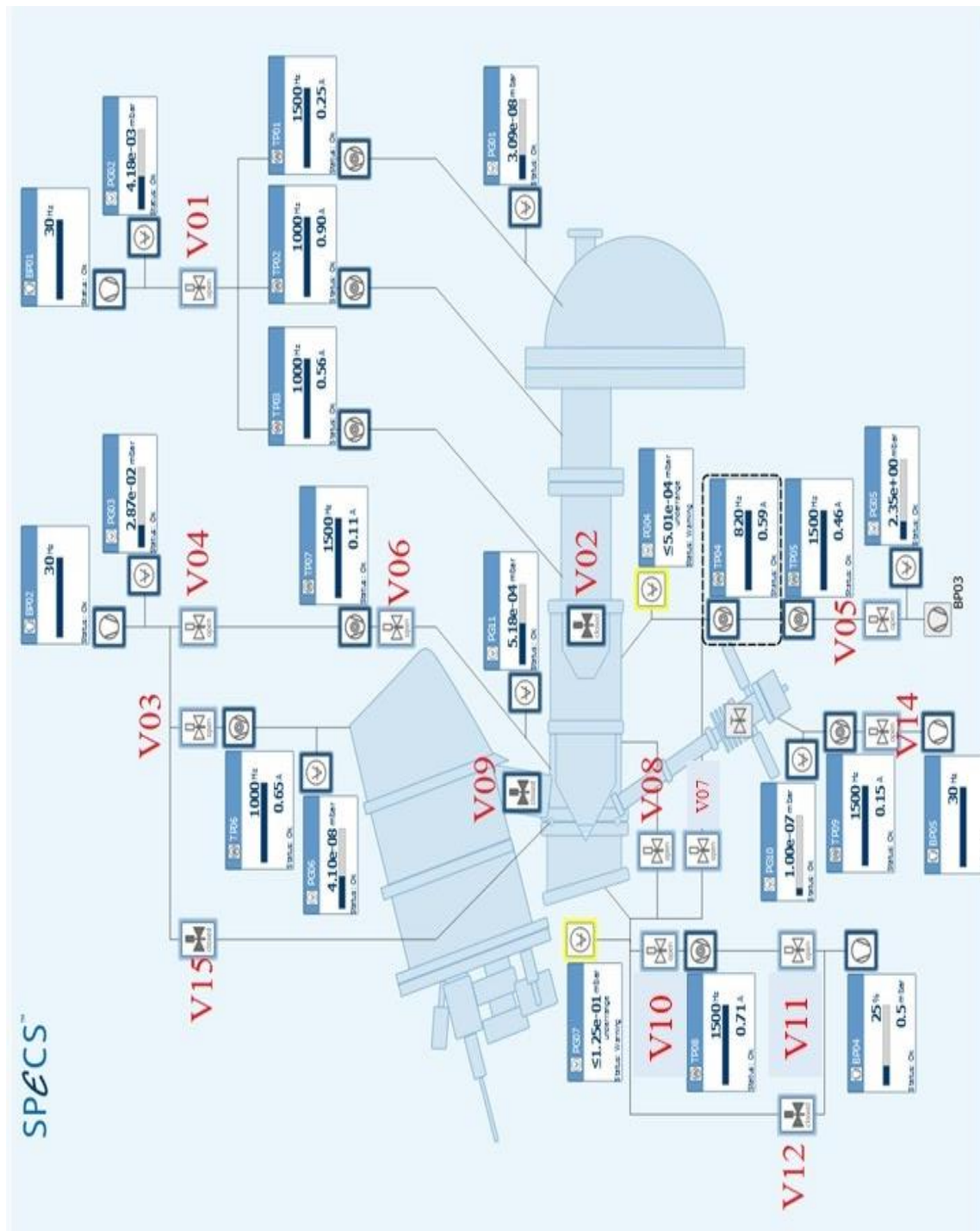
Figure AI.3: *Valve diagram of ambient pressure X – ray photoelectron spectrometer.*

Status: Normal → Bring to Atmosphere

1. Check V09 and V02 are closed (monochromator and analyzer)

2. Check that V08 and V07 are open

    a. These need to be open to ensure the silicon nitride window does not break

3. Check that green vent line is in TP07

4. Turn on purge nitrogen at back of room

5. Isolate all backing pumps from turbos

    a. Close V04, V05 and V11

6. Turn off turbo pumps TP04, TP05, TP07 and TP08 and allow to spin down

7. Select TP07 and vent through this pump.

8. To check for appropriate venting, unplug green vent line from TP07. If not properly vented, the opening will "suck". If there is an increased pressure from over – venting, the opening will "blow" nitrogen.

9. Turn on camera computer and start the camera

At this point, the liquid jet can be put into the chamber. First the trap should be installed with the ball valve at the bottom closed. The jet can then be installed on the top of the sample chamber. This process should be done slowly to ensure the jet does not run into the cone of the entrance to the analyzer. Use three bolts provided to secure the jet. At this point, you should open the ball valve and turn on the liquid jet. The jet stream should be straight and the pressure on the HPLC pump should be normal. If either of those parameters are not met, stop the liquid jet and take it out of the chamber to clean the capillary.

Status: Jet → Pumpdown

1. Close V10, V03 and double check V02/V09 are closed

2. Stop venting through TP07

3. Open V12 and allow pump to pump out entire chamber until approximately 100 mBar

4. Open V05 and allow pump to pump out chamber until approximately 25 mBar

5. Open V04 and allow pump to pump out chamber until approximately ~5 mBar

6. Close V08 and V09

7. Set BP04 to control vacuum at 4 mBar

8. Start TP07 and TP05

9. After 45 seconds start TP04

10. When backing pressure (PG03) reaches <1 x 10^{-1} mBar open V03 to monochromator

11. PG11 and PG04 should be yellow and below 5.01 x 10^{-4} mBar for *at least* 1 hour prior to opening the gate valves to the monochromator and the analyzer.

12. After 1 hour, check the increase in pressure of the monochromator by opening V09. The pressure should be less than 5 x 10^{-7} mBar to do the experiment. Ideally it would be closer to 1 x 10^{-7} mBar prior to the start of the experiment. If the pressure is not low enough, close V09 and continue to pump on that chamber until the pressure is adequate.

13. If the pressure in Step 12 is low enough, turn on the analyzer, lens and x – ray source at the rack. There will be a green button on the rack that is flashing. This is the interlock and needs to be pushed before any control can be activated. Open V02 to the analyzer. You are now ready to begin the experiment.

Setting up and Running an Experiment

1. Connect the monochromator and analyzer in the SPECS program

2. Adjust the liquid jet close to the cone using the camera

3. Start an O1s scan (530 – 540 eV) and observe the peak shape. If the peak shape gives only a gas phase water peak (535.5 eV) the jet or the x – rays need to be adjusted. If the liquid peak is present (533.5 eV) then proceed to Step 5

4. Adjust the jet perpendicular to the cone by eye. This can be tricky to line up the jet and the cone in your line of sight. A small flashlight shone into the sample chamber at an angle helps to illuminate the jet and the cone entrance.

5. Set the analyzer to constant energy mode and sit at the apex of the liquid peak (533.5 eV). Right click and override to a continuous loop. Adjust the liquid jet to maximize the signal of that peak.

6. If the instrument has not been used in some time, the vibrational pads have lost some air, the cone/x-ray window has been changed or a bakeout has occurred the x – ray spot may not be in the correct place. This needs to be manually adjusted on the X – ray monochromator.

7. Once the x – rays are optimized, the lenses need to be optimized. This can be found under the analyzer window in the "additional voltages" tab. PreX, PreY, L1 and L2 can all be adjusted by small increments to maximize the signal of the liquid peak.

8. If either the x – ray source or the lenses have been modified, the jet should then be moved to maximize the signal of the liquid peak. An optimized signal has a gas phase peak >1000 CPS and a liquid peak >500 CPS. The instrument is now tuned and ready for the experiment.

9. The sample should be injected into one of the two sample loops. Different samples can go into different loops. Each loop represents a single experiment. One loop can hold 32 mL while the other holds 29 mL. Your scan time should be adjusted accordingly based on the flow rate of the HPLC pump and the associated loop.

10. Move the jet away from the cone and inject your sample by turning the 2 – way valve. The jet will often stop and bubble until the pressure has equalized and the jet has been restored. Keep a close watch on the bubble to make sure it does not come in contact with the cone.

11. Once the jet has been re-established, start a fixed energy scan on the liquid phase peak and move the jet toward the cone to maximize the signal.

12. You should have set up your experimental parameters for each orbital of interest. At this point, you should run the desired experiments.

13. Every new sample loop that is done should start with Step 10 and continue until the experiment is complete

Completing the Experiment

Once your experiment is complete the liquid jet can continue running while the instrument is brought to atmosphere. The jet should be moved away from the cone to ensure that if anything occurs there will be no concern of the jet hitting the cone.

Status: Jet → Bringing to Atmosphere

1. Close V02 and V09. Disconnect monochromator and analyzer from program. Shut off analyzer and lens power at the rack. *Do not* shut off x – ray source yet

2. Close V04

3. Stop TP07, TP04 and TP05 and allow them to spin down to approximately 30% their max spin speed.

    a. This may take up to an hour to spin down. Shut down X – ray power source

4. Plug green nitrogen venting line into TP07. Turn on nitrogen

5. Once the turbo pumps have spun down low enough, close V05

6. Open V08 and V07

7. Close V12

8. Turn off BP04 and set the pump to "pumpdown" mode. Restart pump.

9. Vent through TP07. Check the venting line after a few minutes for proper venting

10. Shut off liquid jet and take out of sample chamber

11. Close the ball valve on the trap and remove trap

At this point the sample chamber can be cleaned with water and any maintenance can be done at this point. If cleaning, finish with IPA to help pumpdown.

Status: Normal → Pumpdown

1. Open V10 and ensure V08/V07 are open

2. Close V03

3. Stop venting through TP07

4. Open V11 and pump the chamber below 100 mBar

5. Open V05 and pump the chamber below 20 mBar

6. Open V04 and pump the chamber to below 1 mBar

    a. Note: If you have cleaned the sample chamber pumping it down below 1mBar will take a significant amount of time.

7. Start TP05, TP07 and TP08

8. After 1 minute, start TP04

9. Once the backing pressure (PG03) reaches <1 x 10^{-1} mBar open V03

10. Push green light on rack to acknowledge the interlock

Sample Calculation of the Liquid Jet Ratios

In Chapter 2, the calculation for the area intensity of different photoelectron peaks was shown in its full and simplified version. The simplified version is shown here:

$$\frac{I_a}{I_b} = \frac{n_a(z)\sigma_a(hv)L_a(\gamma)\lambda_a}{n_b(z)\sigma_b(hv)L_b(\gamma)\lambda_b}$$

A sample calculation using this equation is shown below. The data is taken directly from Chapter 4 on the ratio of NaBr to the liquid water peak.

Example: 2M NaBr in water

O1s water → Binding Energy: 533.5 eV; Area: 423.15 CPS

Br 3d → Binding Energy: 68.9 eV; Area: 23.53 CPS

Br 3d

KE = 1486.6 eV – 68.9 eV = 1417.7 eV

Atomic Parameters (Asymmetry and Cross Section): 0.042666

IMFP = 1417.7 – 1417.7*exp(1417.7/1486.6) = 920.8981401

Corrected Area = Area/(Atomic Parameters*IMFP) = 23.53/(0.042666*920.8981410) =

0.594283072

O 1s

KE = 1486.6 – 533.5 = 953.11

Atomic Parameters: 0.082

IMFP = 953.11 – 953.11*exp(953.11/1486.6) = 752.774332

Corrected Area = 423.15/(0.082*752.774332) = 6.85512993

Total Ratio:

Br 3d/O 1s = 0.59428/6.85512 = 0.08669173

Actual Ratio:

2M/55M water = 0.036 which is a bit smaller than the ratio above however bromide is known to surface segregate and would account for the higher overall ratio calculated using this method.

Appendix II: Microfluidic Mixing Chamber

The microfluidic mixing chamber used in chapter 7 was designed and fabricated by Dan Deponte at SLAC National Accelerator Laboratory at Stanford University. All parts and accessories were provided by Dan. The main providers of the chips were Micronit Microfluidics and the holder was fabricated by Neptune Fluid Flow Systems.

There were two designs that had been considered for feeding the sample lines through the vacuum flange and into the microfluidic holder. The designs are shown below in Figure 1.
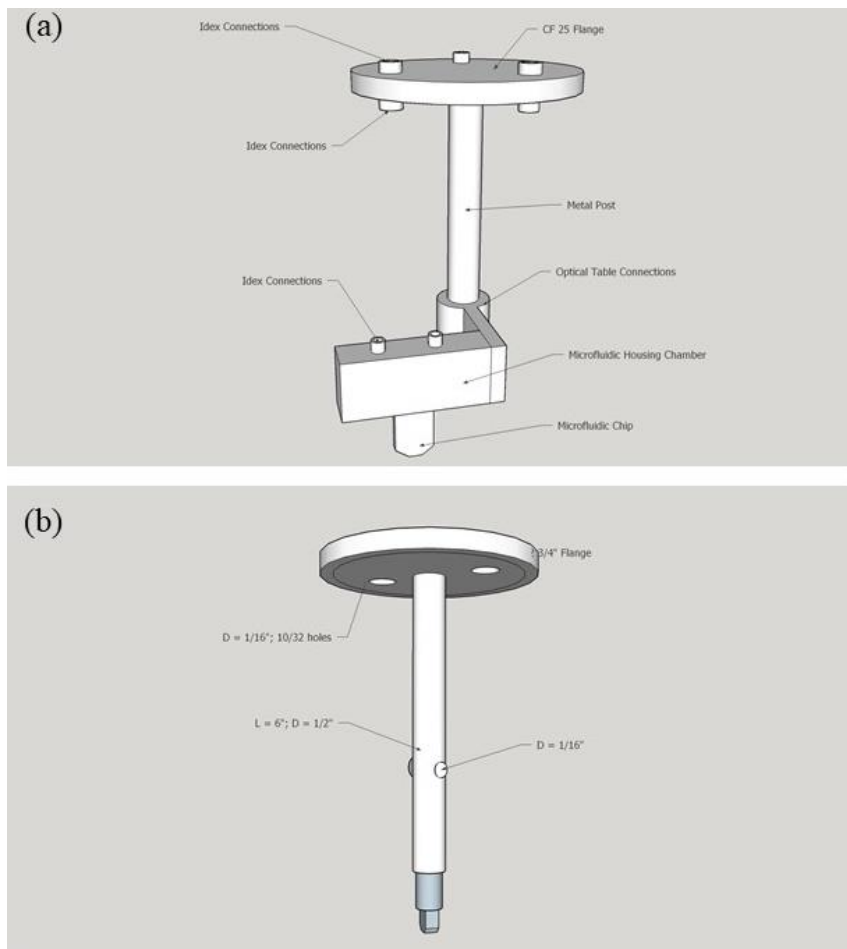

Figure AII.1: Mixing Jet schematics for mounting the jet on the flange (a) used a single post with optical table mounts (b) single post with NPT threads on the bottom that fastened the housing to the post

Figure 1b was the final version that is being used today. The post is cut into two pieces that are fastened together by an NPT threading. The bottom section is hollow and allows for the two lines to be connected to the holder and then fed out of the 1/16" holes before coming to the flange. At the flange the holes were drilled through the flange and the threading was tapped through the holes. An adapter of 10/32 Male x 10/32 Female PEEK from IDEX Health and Science (P-636) was used to create a seal that allowed the liquid jet to be run at 4 mBar under vacuum. This part needed to be drilled out due to the fact we wanted to have the 3/16" OD green tubing to go through the fitting rather than use the existing part. An image of the mixing jet setup is shown below in Figure 2.
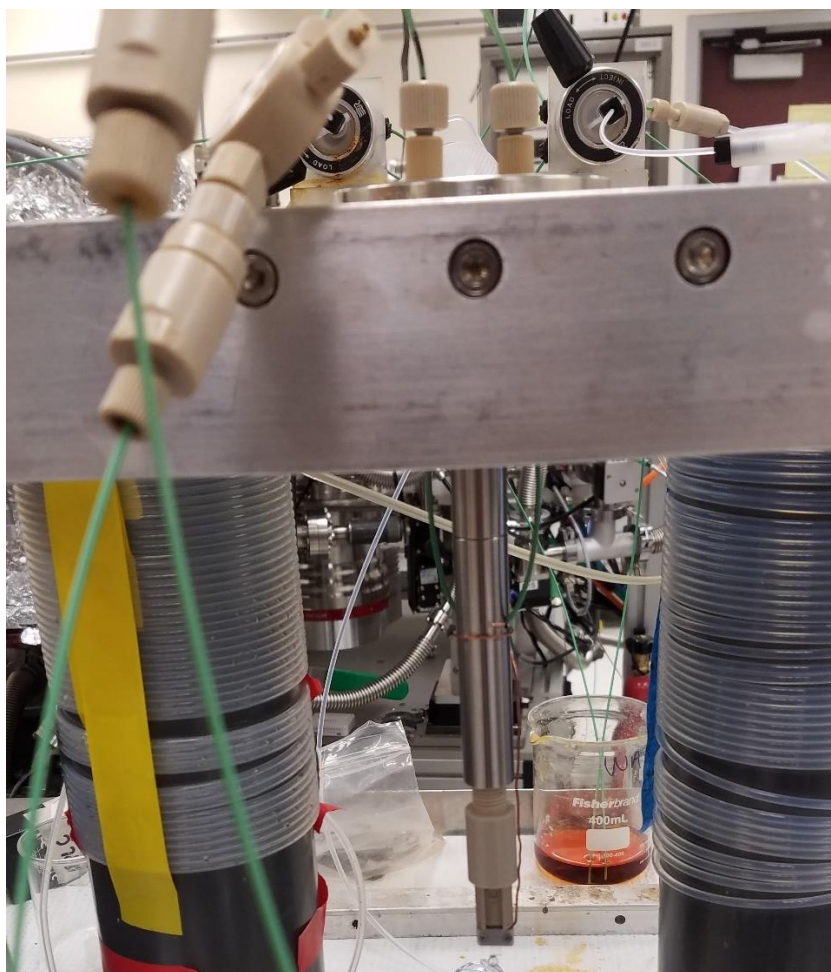
Figure AII.2: Mixing Jet fastened on the post. Two lines with their own HPLC pump are shown. The lines are sealed to a level that allows control of the pressure in the liquid jet chamber and there is no detectable atmospheric oxygen contamination.

The metal plate and screws on the holder need to be non – magnetic. In the first few experiments the O 1s of the water gas phase was very broad and the peak intensity was very low. This was due to the magnetic screws that were on the holder. These were replaced and a standard O 1s spectrum was collected. Figure 3 shows a closer view of the holder and mixing jet chip used in the mixing experiments.
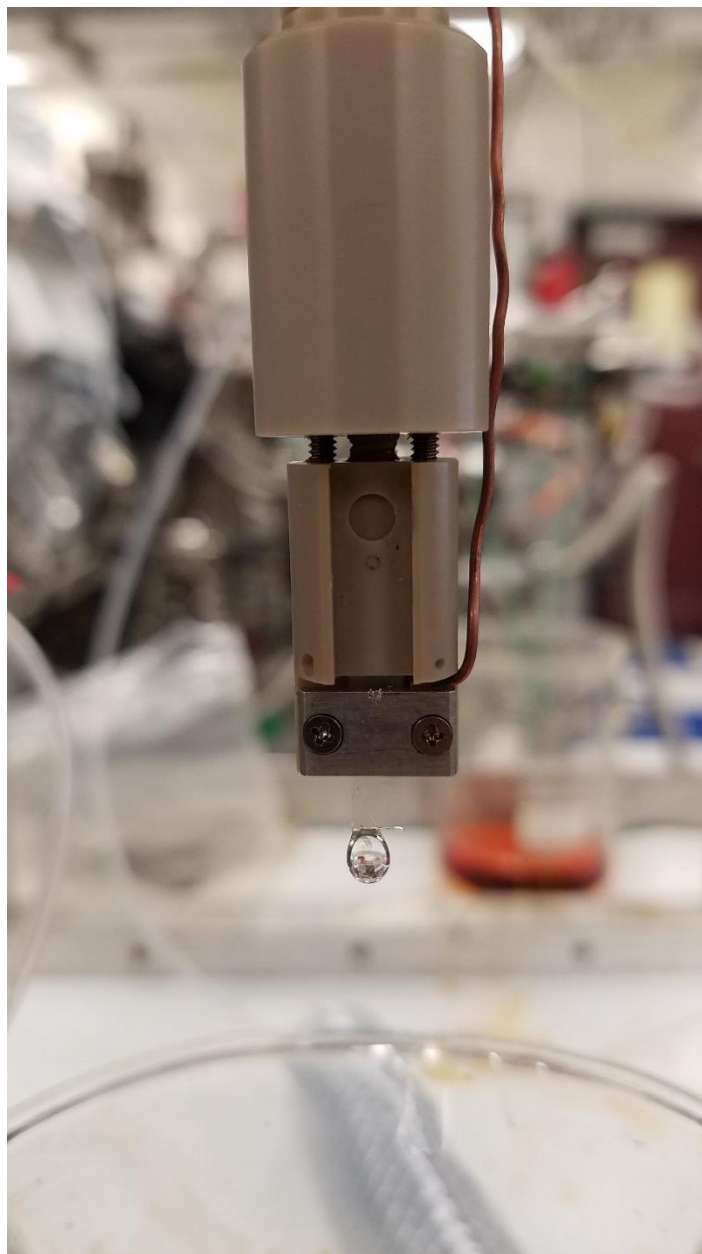
Figure AII.3: *Close up of mixing jet chip and holder. The copper wire was added as a grounding wire to the front plate.*

The holder was mounted to the post with an NPT fitting. The microfluidic chip can be very breakable and should be tightened gently so as not to break the chip. There are two small o – rings that create the seal between the holder and the chip. The copper wire was added as a grounding wire for the front plate and is grounded to the post inside the liquid jet chamber. All experiments

follow the experimental procedures outlined in Chapter 2 for the liquid jet and Chapter 6 for specific mixing jet experiments.

Finally, the schematics of the chip are proprietary information owned by the Micronit company. Contact Dan, myself or Micronit if more chips are needed to be made.